The Study and Characterisation of Plasma Microfluidic Devices

Ph.D Thesis

Olumuyiwa Tobi OLABANJI

April 2012

Thesis submitted in accordance with the requirements of the
University of Liverpool for the degree of Doctor in Philosophy

"In the middle of difficulty lies opportunity." **Albert Einstein**

"A wise man will make more opportunities than he finds." **Sir. Francis Bacon**

"We know what we are, but know not what we may be." **William Shakespeare**

"The ultimate power to possess is that of forgiveness." **O. T. Olabanji**

"The PIN code for success is ***b****elieve,* ***h****ard work,* ***p****lay and* ***d****iscipline."* **O. T. Olabanji**

DEDICATION

I lovingly dedicate this thesis to my wonderful son, Olukayode Victor Nathanael Olusegun OLABANJI and to my late Aunty, Mrs. Abiola Oyeyipo.

STATEMENT OF AUTHENTICITY

I hereby certify that the work presented in this thesis is, to the best of my knowledge and belief, original except as acknowledged in the thesis. I hereby declare that I have not submitted this material, either in whole or in part, for a degree in this or any other institution. I can confirm that all sources on which is based have been acknowledged in the references.

ABSTRACT

Controlling the behaviour of atmospheric pressure plasmas and their interaction with polymeric materials is of major interest for surface modification applications across multidisciplinary fields intersecting biomedical engineering, bio-nanoengineering, clinical/medical science, material science and microelectronics. The aim of the present work is to investigate the behaviour of atmospheric pressure dielectric barrier discharges in closed systems (microfluidic devices) and open systems (glass capillary devices) and their polymer-surface interactions. Atmospheric pressure microplasma jets operating in helium gas have been used to modify locally the surface energy of polystyrene (PS) and to interact directly with the surface of analytes using a novel plasma assisted desorption ionisation (PADI) method causing desorption and ionization to occur. Although atmospheric pressure micro-jets are now widely studied for the treatment of materials there is still a lack of understanding of the fundamental plasma-surface processes. A number of recent studies using plasma micro-jets for the surface modification of polymerics have used systems in which the emerging plume impinges directly the substrate head-on. Here, by placing the micro-jet side-on to the substrate we can observe how different flow regions of the jet affect the sample, allowing individual effects to be seen. In addition, this configuration may prove an efficient way of treating samples with reduced or no surface damage. These conclusions are considered to be an important contribution to the study of complex mechanisms underpinning the behaviour of radicals and reactive species in surface modification processes of polymeric materials.

The study of the behavioural mechanism involved in the plasma was done using various diagnostic techniques such as electrical measurements, optical emission spectroscopy (OES), Time-averaged and time-resolved ICCD Optical Imaging and Schlieren Photography. The filamentary discharge mode was observed in bonded microchannels using metallic and liquid-patterned electrodes. The treated surfaces were characterised using various techniques such as X-ray photoelectron spectroscopy (XPS), Atomic Force Microscopy (AFM), Optical profiling measurements and Water Contact Angle (WCA) measurements. Schlieren photography has been used to indentify regions of laminar (pre-onset of visual instability) and turbulent flows (post-onset of visual instability) in the exiting gas stream and the nature of their interaction with the substrate surface. The length of both regions varies depending on operating parameters such as frequency, applied voltage and flow rate. WCA results from treated polystyrene (PS) samples exposed directly facing the microjet reveals a change from hydrophobic (high contact angle) to a hydrophilic (low contact angle) surface with substantial reductions in WCA (~ 50 to 60 °) occurring in downstream regions where the turbulent gas mixed with air impinges the substrate surface. In contrast, only small changes in WCA (~ 10 to 20 °) occur in regions where the gas flow is laminar. AFM imaging of treated PS samples reveal holes and ripple like effect with a much larger area than that of the capillary seen on treated samples positioned "head-on" and directly facing the sample but this was not seen using the side-on configuration. The results indicate that excited air species (either mixed or entrained in the He gas flow) which exist only in regions of turbulence are the main agents causing surface covalent bond breaking leading to surface modification. This thesis reports on atmospheric pressure microdischarges and their applications, a brief summary of work done so far including major results, using new and existing technologies including those under development in terms of design, properties and working conditions.

ACKNOWLEDGEMENTS

This thesis would not have been possible without the guidance and the help of several individuals who in one way or another contributed and extended their valuable assistance in the preparation and completion of this study.

I would like to first and foremost thank God Almighty who has made it possible to achieve the completion of this work.

Secondly, I would like to thank my Principal Supervisor, Prof. James William Bradley for his continued guidance, support and encouragement.

Special thanks go to Dr. John Marsland, Dr. Paul Unsworth, Dr. Paul Bryant, Dr. James Walsh and Dr. Robb Dodd for their professional advice.

Special thanks to, my Dad, Prof. Simon Olukayode Olabanji, my Mum, Mrs. Victoria Moromoke Olabanji, my sisters, Titilope (Sistai), Oluwaseun (Sisken), Olufunwo (Sisfun) & Opeyemi (Opuslala), my darling wife, Mrs. Oyinlade Kofoworola Olabanji, my big uncle, Elder Emmanuel Oladipo, my big aunty, Mrs. Ruth Oladipo, Mr. Oyeyipo and my brothers-in-law, Bro. Femi, Bro. Phillip, Dr. Riwo and Dr. Julius for their sincere support, advice and encouragement.

Special thanks go to our collaborators at Ian Wark and Mawson Research Institutes, University of South Australia for supporting this work.

Funding for this project by the University of Liverpool Doctoral Training Award (DTA) is also gratefully acknowledged.

Lastly, I wish to thank Mr. Alan Roby, Mr Alan Edwards, Mr. Alan. Noble, Ms. Gill Anson, the technicians of the electronic workshop, colleagues and friends for providing assistance when required.

AUTHOR'S CONTRIBUTION FROM THIS THESIS

Journal Publications

1) **Olumuyiwa. T. Olabanji**, Craig Priest, Endre J. Szili , John Ralston, Robert D. Short and James W. Bradley; Time-resolved Imaging and electrical characterization of a microdischarge inside a microfluidic chip, *Lab on a Chip*. 2012.(Submitted Paper)

2) **O. T. Olabanji** and J.W. Bradley; Side-on surface modification of polystyrene with an atmospheric pressure microplasma jet, *Plasma Process. Polym*. 2012.

3) **O. T. Olabanji** and J.W. Bradley; The development and analysis of plasma microfluidic devices, *Surface and coatings technology*, 2011, 205, S516

4) Jun-Seok Oh, **Olumuyiwa T. Olabanji**, Craig Hale, Raffaello Mariani, Konstantinos Kontis and James W Bradley (2011); Imaging gas and plasma interactions in the surface-chemical modification of polymers using micro-plasma jets, *Journal of Phys. D: Appl. Phys.* 2011, 15, 155206

5) James W. Bradley, Jun-Seok Oh, **Olumuyiwa T. Olabanji**, Craig Hale, Raffaello Mariani, and Konstantinos Kontis; Schlieren Photography of the Outflow from a Plasma Jet, *IEEE Trans. Plasma Sci*, 2011, 39, 2312

Book Chapter

6) J W Bradley, J-S Oh, B Abdullah, S A Voronin and **O T Olabanji**, K G Doherty, C M Sheridan and R L Williams, M Zelzer, D Scurr, A J Urquhart and M R Alexander, N Gadegaard (2011), Plasma chemical modification of 2 and 3-D structures in cell-surface interaction studies in the volume entitled: Biomaterials and Plasma Processing, Editors: Nicoleta Dumitrascu, Ionut Topala ISBN: 978-973-703-543-1

TABLE OF CONTENTS

LIST OF FIGURES

LIST OF TABLES

CHAPTER ONE

1.0 Introduction

Abstract

In this chapter, the author attempts to review some concepts relevant to the research project by surveying works from numerous research books, papers, and journals, published in the past few decades. Additional information has been drawn from private communications with lecturers and supervisors, and also conferences and seminars attended. It is the author's intention to help our understanding of the fundamental principles of plasma dynamics at macro scales, and most importantly the scaling down of these processes at micro and nano scales.

1.1 Scientific Background

The word plasma is derived from the Greek word meaning to mould, from which also words like plaster and plastic take origin. In 1929, Irving Langmuir suggested that the word plasma will be used to designate that portion of an arc type discharge in which the densities of ions and electrons are high but substantially equal. This discharge acts like a form of substructure carrying so many diverse particles, like high-velocity electrons, molecules ions, excited atoms, molecules, similar to the way blood plasma carries red and white blood cells, and nutrients around the body. Langmuir realized this similarity of discharge structures and was looking for a name to describe this new state of matter. These subsequently seemed to have created some

confusion in the medical communities until the word plasma became widely used for any kind of ionised gas. The most popular definition is the one given by Chen's (1984), which defines a plasma as a quasineutral gas of charged and neutral particles that exhibit a collective behaviour, resulting from the fact that charged particles generate local concentrations of positive and negative charge, which give rise to local electric fields that generate currents, and also magnetic fields that in turn affect the motion of other charged particles far away.

Plasmas are chemically active material that can operate at low or very high "temperatures", and are referred to respectively as cold or thermal plasmas, depending on the mode of activation as well as the working power. Thermal plasmas, popularly known as arc plasmas have been extensively industrialised by the aeronautic sector whereas cold plasma technologies have been developed in the microelectronics sector. The wide range of temperature enables various applications for plasma technologies such as surface coatings, waste destruction, and chemical synthesis and gas treatments.

Plasma is a distinct state of matter unlike solids, liquids or gases that can be defined as partially ionized gas in which a certain proportion of electrons are free rather than being bound to an atom. Plasmas are able to respond to electromagnetic fields as they are electrically conductive, owing to the independent movement of the positive and negative charges contained within it. Plasmas are generally referred to as the fourth state of matter and by far the most common, both by mass and volume. Plasmas constitute more than 99% of the universe and take the form of neutral gas-like cloud [1]. Plasmas can be created by applying appropriate energy to a gas in order to reorganise the electronic structure of the species, and also to produce excited species and ions. The energy applied that can be thermal, or carried by either electric current of electromagnetic radiations. Plasma properties in terms of electron density N_e and

temperature T_e can change depending on the type and amount of energy transferred to it [2]. The essential mechanisms in the plasma are excitation and relaxation, ionization and recombination.

1.2 Microplasmas

Microplasmas have attracted more and more attention due to their unique characteristics, such as weakly-ionized, boundary dominated phenomena and high ion density. Some have been developed in environmental, UV radiation source and plasma-reactors fields [3, 4]. A variety of electrode configurations in the microplasma devices have been studied and these include spirals or slits in the cathode, dielectric and anode [4]. For example, Eden et al developed microplasma devices fabricated in Silicon in 1997, and also extended the array dimension to 500 μm x 500 μm [3, 6], with luminance capable of reaching 2000 cd m^{-2} operating with N_e or 50% X_e gas mixtures at total pressure 800 Torr [3]. In 2006, Park and Eden also developed microplasma devices with aluminium electrodes encapsulated with alumina, with luminance reaching 500cd m^{-2} at a pressure of 500 Torr of N_e gas [7]. More recently, Eden et al developed addressable microcavity plasma devices fabricated in silicon [8] by plastic-based replica moulding [9].

Microplasmas operated either at atmospheric or reduced pressure exist in various configurations. Among these are, direct current (dc) discharge glow discharges used as molecular emission detectors as demonstrated in [10 -13], electrolyte-as-cathode glow discharges (ELCAD) [14 -18], liquid-sampling atmospheric pressure glow discharges e.g. [19 –

22], miniature inductively coupled plasmas [23 -25], capacitively coupled radio-frequency discharges [26 -31], microwave induced plasmas using microstrip technology [32 -34], dielectric barrier discharges [37- 41] , microstructure electrode discharges (MSD) e.g.[35, 36] and other variations [42]. An overview and general description is presented by numerous studies [43 -46] and literature reviews

1.3 Dielectric Barrier Discharge (DBD)

This is usually formed between two parallel electrodes with a separation in the order of 0.1 to 10mm, where one or both electrodes are covered with a dielectric barrier due to dielectric charging issues associated with direct current (dc) operation. They are normally operated with square wave currents, sinusoidal wave currents or pulses waveforms with frequencies ranging from a few Hz to MHz, but often in the KHz range [47]. The amount of displacement current that can flow through the dielectric is determined by the dielectric constant and thickness.

DBDs are strongly non-equilibrium plasmas and are often operated at atmospheric pressure. They have unique properties and characteristics which form the basis for many applications such as ozone generation, plasma display panels, surface engineering processes, gas treatment and excimer lamps [48 – 56]. Examples of the DBD characteristics are described in [37 – 40], and demonstrated with low electric power (< 1W), low gas temperature (~ 600K) plasma sources, and excellent dissociation capability for molecular species. These characteristics have been explored at reduced pressures (10-100mbar) in plasma modulation diode laser atomic absorption spectrometry of excited states of chlorine and fluorine, with typically helium or argon as the plasma gases. Figure 1.1 below shows an operation in a capillary surrounded by two ring electrodes, where the dielectric barrier discharge is at the end of the capillary, and

where gas flow extends the plasma out of the capillary [57, 58] . These sources are typically dielectric barrier discharges operating in non-thermal equilibrium with energy coupled through the dielectric material of the capillary wall from external ring electrodes. The plasma and neutral gas species are effectively "cold" providing the opportunity to develop these sources for applications in health and live science and in applications with thermally sensitive surfaces. This method has been applied for the detection of chemical warfare analytes, for the detection of gas phase compounds [59], drugs and explosives, medical applications [62, 63] and for process control, food and safety [60, 61] .

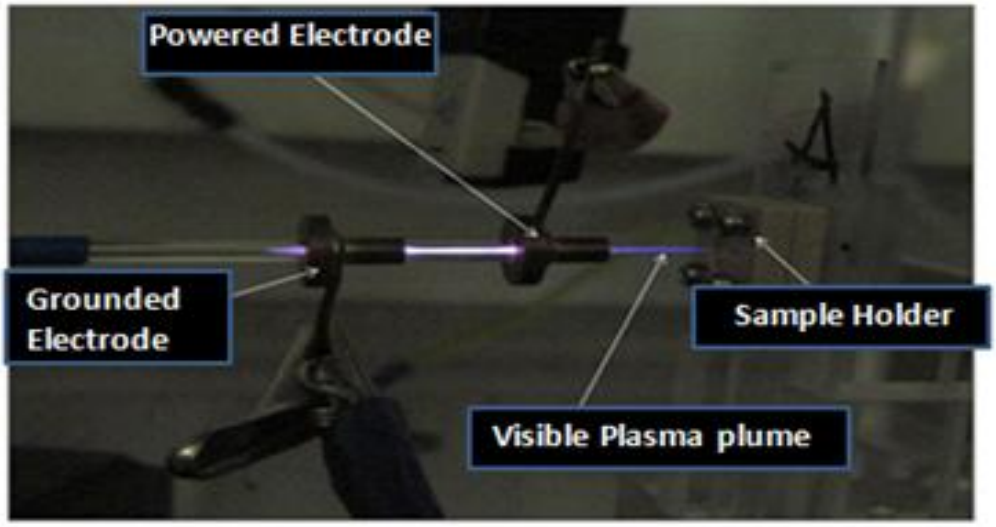

Figure 1.1. Experimental arrangement and plasma source

The kind of discharge gas determines the stability of the glow discharge. For example, helium gives rise to a stable homogeneous glow discharge, whereas nitrogen, oxygen and argon easily cause the transition into a filamentary discharge. However, by changing the electrode configuration, it is still possible to let them operate in a homogeneous glow discharge regime according to Kanazawa et al. (1988) and Okazaki et al, (1993).

Applications include the development of an atmospheric pressure micro-discharge in a hollow-cathode with diameter of about 100 - 200 μm, in a work reported by others [64]. A small atmospheric pressure discharge was operated in open-air with an electrolyte solution as the cathode, to be used for analysis of water and waste water solutions. The use of an atmospheric pressure helium DC discharge on a microchip, as an optical emission detector for gas chromatography with dimensions ranging from 1- 2mm length, width and depth of a few hundred microns, leading to a plasma chamber of 50 – 80nl volume was also reported [65 - 66].

1.4 Atmospheric plasma sources

The atmospheric plasma sources can be broadly classified according to their excitation modes into the following;

1. AC/DC (alternating/direct current) and low frequency discharges
2. The plasmas which are ignited by radio frequency waves
3. Microwave discharges

The following diagram (figure 1.2) shows an example of the variation range for F_{pe} (frequency of the electrons in the plasma) and F_{pi} (ions frequency) in cold plasmas (e.g. glow discharges). The excitation frequency is important because it influences the behavior of the electrons and the ions. Figure 1.3 shows different ranges of plasmas with corresponding electron temperatures and densities.

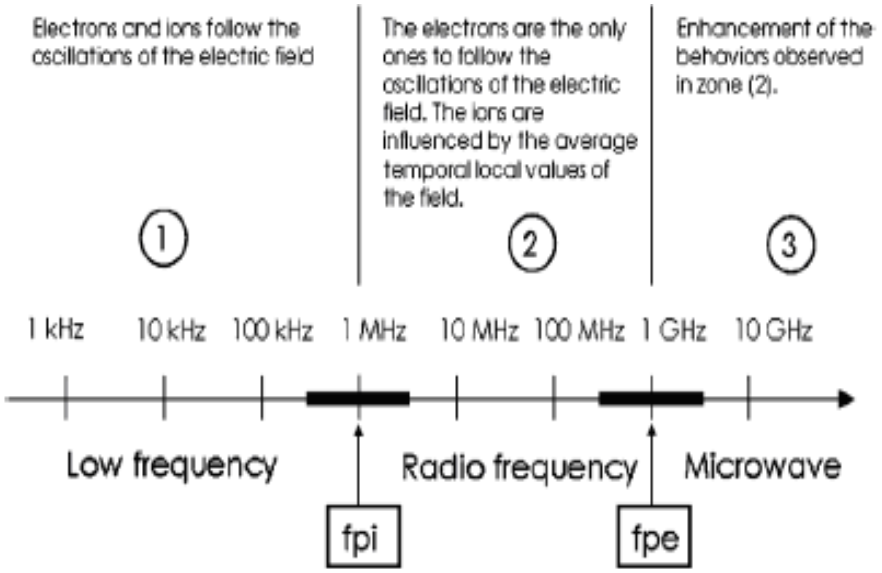

Figure 1.2. Electron and ion frequencies in cold plasma [1]

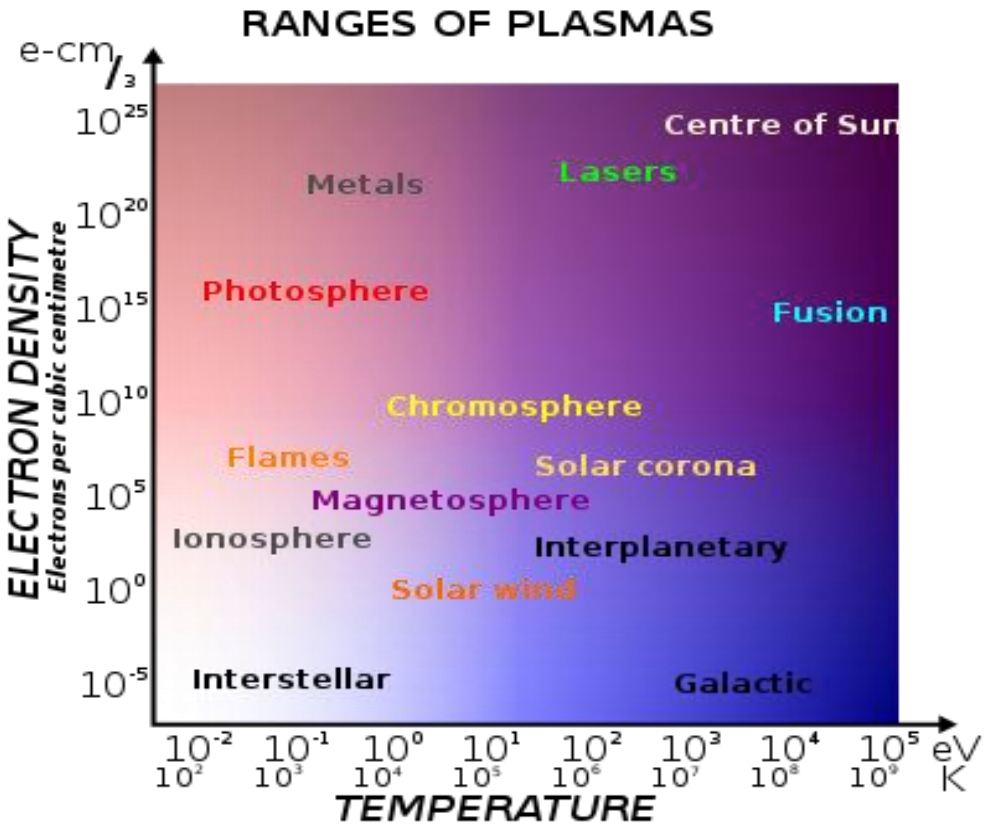

Figure 1.3. Different ranges of plasma with corresponding electron density and temperature

1.4.1 AC/DC (alternating/direct current) and low frequency discharges

These can either work with a continuous or pulsed mode depending on their design. A pulsed working mode enables the injection of large energy amounts in the discharge while the system warming up is limited. On the other hand, a pulsed power supply is technically more complex than a DC source, hence compromising the reproducibility of the process [1].

When a sufficiently high potential difference is applied between two electrodes placed in a gas, the latter will break down into positive ions and electrons, giving rise to a gas discharge, the electrons are accelerated by the electric field in front of the cathode and collide with the gas atoms. The most important collisions are the inelastic collisions, leading to excitation and ionisation. The excitation collisions, followed by de-excitations with the emission of radiation, are responsible for the characteristic name of the "glow" discharge. The ionisation collisions create new electrons and ions. The ions are accelerated by the electric field toward the cathode, where they release new electrons by ion induced secondary electron emission, as explained above. The electrons give rise to new ionisation collisions, creating new ions and electrons.

1.4.2 RF discharges

The RF sources can work with a high or low power supply depending on their structure. The structure influences the properties of the plasma and also determines its potential applications. The impedance matching can be either inductive (high powered discharges) or capactive.

1.4.2.1 Inductively coupled RF discharges

The inductive discharges have been known for a long while. An example is the RF torch [1] in which the plasma is initiated and maintained by an RF fed helical coil. The current that flows in the RF coil induces a timevarying magnetic field nearby the plasma zone. The resulting electric ring field (from Faraday law) accelerates the electrons and thus sustains the discharge. The frequency of the generated plasma is higher than 1 MHz and the frequency level implies that electrons follow the electric field oscillations and that neither ions nor electrons can reach the torch wall. This lack of contact between the plasma and the wall reduces the pollution of plasma and torch walls which enables to work with different gases: inert, reductive, oxidant, nitriding gas [67].The inductive torches work in a wide power range, typically 20 kW– 1000 kW, with a gas flow rate of 10 –200 slm.

1.4.2.2 Capacitively coupled RF discharges

The term "capacitively coupled" refers to the way the electric energy is coupled into the discharge, i.e. by means of two electrodes and their sheaths forming a kind of capacitor. At the typical RF frequencies, the electrons and ions have a totally different behaviour, which can be explained by their different masses. Because of their small inertia, the light electrons can follow the instantaneous electric fields produced by the applied RF voltage. The frequencies generally used for these alternating voltages are typically in the radiofrequency (RF) range (1 MHz -100 MHz; with a most common value of 13.56 MHz or multiples of it), but when the electron density varies from 10^{16} to 10^{19} m^{-3}, the plasma frequency ranges from 9×10^{8} to 3×10^{10} Hz, which is much higher than the typical RF-frequency of 13.56 MHz.

1.4.3 Microwave induced discharges

The discharge ignition is key to microwave sources.Self-ignition of the discharge ensures flexible operating conditions and enables the industrialization of the process. The energy, transmitted to the gas electrons, has to be high enough to initiate the plasma [1]. For microwave induced plasmas, microwaves are guided along the system and transmit energy to the plasma gas electrons. Elastic collisions between electrons and heavy particles results in a rebound of the collided electrons whereas the heavy particles remain static. After several elastic collisions (which follow probabilistic laws), the electrons get enough energy to produce inelastic exciting or even ionizing collisions. The gas is partially ionized and becomes plasma which supports microwave propagation [68].

Plasmas or partially ionized gases are complex systems containing a range of reactive species including radicals, metastables, ions, electrons, and photons. Although they can be generated in many ways, they are most commonly created in the laboratory using radio frequency (rf), microwave, or direct current (dc) applied electrical power. The highly reactive nature of the plasmas makes possible a number of reactions at the gas phase as well as the gas-surface interface. The gas-phase plasma species reaction with the interface (e.g. the reactor walls or the substrates) can be classified into three categories namely:

1. Etching or removal of material
2. Deposition which refers to the formation of a different chemical material on the substrate
3. Surface modification, which refers to the implantation of chemical functional groups in the outermost layer.

The complexity of plasma chemistry is amplified by the number of system variables used for process optimization, including equipment variables (reactor size and configuration, materials for construction, method and amount of power applied); gas variables (pressure, flow and gas ratios); and substrate variables such as temperature, material and the location of the reactor. Often, small changes can result in large changes in the overall process chemistry, and it is therefore important to understand the challenges of balancing the sensitivity of these different parameters. It is therefore necessary to design microfluidic diagnostic devices that are straight forward, reliable as well as have the following characteristics [69]:

1. Allow for identification and quantification of all plasma species
2. Can be performed in a non-intrusive manner
3. Can provide data on the gas phase, surface and gas-surface interface
4. Characterize the internal and external energies of plasma species

1.5 Dusty plasmas

This is a property of many gas discharges such as the presence of little dust, particles or clusters, in the plasma, but does not actually indicate a type of discharge. Dust particles do not only change the chemistry, but also the electric field. These dust particles are normally considered to be contaminants, which reduce the performance of the plasma processes and the quality of the final result. Indeed, with the decreasing feature sizes on integrated circuits, the tolerance for dust particles becomes smaller, and very small dust particles with a diameter of only a few tenths of a μm, can destroy the microfluidic device.

The presence of dust particles is useful in plasma processing applications for driving impurities in plasmas under the action of strong electromagnetic fields. Often, the properties of dusty plasmas will be determined by how and where the particles move in the plasma and this is controlled by the various forces acting on the particles.

Some applications, such as the production of photoluminescent and electroluminescent materials, sub micron catalysts, fullerenes, nanotubes and other clusters have been developed with the use of dusty plasmas [70].

1.6 Plasma Characterization Techniques

Plasma diagnostics for both industrial processes and fundamental studies have been the subject of numerous review articles and books, although very little is known about plasma processing mechanisms due to the incompleteness of the picture presented by studies attempting to address plasma or gas-surface interface chemistry as well as studies focusing on correlating surface properties with plasma parameters. Consequently, recent studies suggest a combination of techniques, affording broader descriptions of plasma processes with primary focus on in situ optical gas-phase diagnostics. Although a detailed description of the techniques can be found elsewhere [69], such techniques include:

1. Optical Emission Spectroscopy (OES)
2. Optical Absorption Spectroscopy (OAS)
3. Laser Induce Fluorescence (LIF)
4. Imaging of Radicals Interacting with Surfaces (IRIS)
5. Cavity Ringdown Absorption Spectroscopy (CRDS)
6. Fourier Transform Infrared Spectroscopy (FTIR)

7. Langmuir probe technique

8. Mass Spectrometry

1.6.1 Optical Emission Spectroscopy (OES): This technique is used for analyzing light emitted from a given medium in the absence of external excitation by means of collection, and detection of light. Gas phase-species in plasma are promoted to excited electron states by colliding with energetic electrons followed by relaxation accompanied by emission of a photon. Emitted radiation is spectrally dispersed and detected in OES and this technique can be employed both qualitatively and quantitatively for the identification of plasma species and the detection of absolute or relative species densities [69].

1.6.2 Optical Absorption Spectroscopy (OAS): This technique is used for measuring light absorbed at a particular wavelength and also for probing highly excited-state species as they are long lived, but do not decay via emission of a visible photon. OAS is comparable to OES in terms of equipment simplicity as it basically consists of a light source (e.g. tungsten or gas-discharge lamp), which is directed into a sample chamber and then analyzed by a detector placed opposite to the sample [69].

1.6.3 Laser-Induced Fluorescence (LIF): This technique probes ground-state species with sensitivities of the order of 10^8 cm^{-3}. The basic setup comprises a tunable laser and a detector for collecting fluorescence, situated orthogonal to the beam source. LIF occurs due to the interaction of Laser light of the correct wavelength with molecules contained within the

sample volume, causing resonant absorption. LIF experiments are capable of providing relative and absolute number densities, gas temperature T_g, surface reactivities, data on kinetics and electric fields in plasmas [69].

1.6.4 Imaging of Radicals Interacting with Surfaces (IRIS): This technique combines molecular beams with spatially resolved LIF and is used for resolving radical-surface interactions during plasma processing. IRIS can be used to determine velocities by means of exploring the time resolution of the CCD, and also for the study of plasma ions via mass spectrometry [69].

1.6.5 Cavity Ringdown Absorption Spectroscopy (CRDS): This technique measures the temporary decay in the light intensity leaving the laser output coupler, using laser pulses to determine the absorption of a sample placed directly in the laser's optical cavity. The ringdown is time required for the output signal to decay to a fraction 1/e of its initial value and this is often used to correct for mirror reflectivities and cavity dimensions at nonresonant wavelengths [69].

1.6.6 Fourier Transform Infrared Spectroscopy (FTIR): This technique focuses on both the gas phase and processed surfaces and finds applications across a range of chemistries. Information on plasma generated species can be obtained via this method by monitoring plasma effluent in the exhaust region [69].

1.6.7 Langmuir Probes: This technique is most widely used for measuring the plasma current potential (I-V) relationship with similar functions to electrodes in electrochemical cells. Resulting data which includes electron temperature (T_e), electron density (N_e) and plasma potential (V_p) can be obtained using probes in potential sweep mode configuration [69].

1.6.8 Mass Spectrometry: This technique provides information about the identity and concentration of plasma species using a mass spectrometer which consists of an ion source, an analyzer, and a detector. Some advantages of using this technique for plasma diagnostics include fast analysis, good sensitivity, compactness and robustness [69].

1.7 The concept of Lab-on-a-chip

The concept of micro-total analysis system (μTAS) or "lab-on-a-chip" devices has gained a remarkable amount of popularity in various science and engineering fields over the past decade [71 -74]. Most of these interests arise from the possibility of incorporating sample-processing steps such as sample pretreatment, dilution, calibration, separation and detection onto a small dimensioned "chip" of the order of a few tens of microns up to a few centimeters [75- 81]. Critical to the successful implementation of μTAS technologies are the availability of a simplistic device prototyping and preparation methods, the physical and chemical characterization of the substrate material, and the development of integrated "on-chip" analyte detection methods [82, 83].

Many of the promising aspects of μTAS arise due to scaling laws, specifically the large increase in surface area to volume ratio as well as enhanced portability associated with reduction in dimensions, which makes possible faster processing and an increased efficiency at the micro scale versus the macro scale. e.g., of smaller required volumes, lower reagent consumption, and the ability to place many microfluidic architectures in a relatively small area, thus allowing multiple studies to be performed in parallel [72, 73, 82]. Majority of these devices have been applied to bioanalysis, i.e., cell and protein-based assays for high-throughput drug delivery, purification, separation and analysis, as tremendous amounts of time, reagents and samples can be saved.

The development of suitable detection methods for micro analytical devices presents a significant challenge to the extremely small sample volumes involved and the desire to minimize the amount of instrumentation used in order to maintain portability. Glow discharge optical emission spectroscopy (GD-OES) has recently been demonstrated to be an effective method for integrating with miniaturized GC systems [71, 72] and benefits not only from low detection limits but also allows atomic and molecular determination to aid analysis. The distinct advantage of the miniaturized emission detector, apart from its low consuming power is that it can operate at atmospheric pressure as a result of the scaling laws that apply to glow discharge [71, 73, 74]

1.7.1 Lab-on-a-chip /Microfluidic devices

Microfluidic technology has progressed remarkably over the last 15 years from a technology being exploited by small groups of researchers to commercially available products being

exploited to solve complex biological problems. Despite significant advances in microfluidic design and fabrication, there remains a strong drive to improve microfluidic utility and functionality. However, most microfluidic chips exhibit homogeneous microchannel surface chemistry, which imposes limitations in a range of applications. Microfluidic chips are usually made by etching a microchannel in one half of the chip and then sealing the channel by bonding it to a flat base, either thermally or by gas plasma surface activation. The open half of the microchannel can be patterned prior to bonding using techniques such as photolithography, inkjet printing and gas plasma based methods. However, the post-bonding of modified surfaces poses two major problems: (1) it may result in a weak bond between the two halves of the chip; or (2) the bonding process itself may further modifiy the surface chemistry of the microchannels. The understanding of the microplasma behaviour within the microchannels is key to its design and development. One solution is the surface modification of the microchannels after pre-bonding.

Microfluidics has brought many advantages for analytical chemistry applications by the miniaturization of analytical devices. Silicon was the first material used as it is well known in the semiconductor industry and because its properties and processing are well established. Another often used material in microanalysis systems is glass due to its broad study in analytical chemistry and because of its chemical and thermal stability. Although glass has other favorable properties, its microprocessing is somewhat challenging, therefore making its use somewhat impractical. Polymers tend to be more attractive due to their low cost and easy processability [84 - 85], although the drawback is typically their poor thermal and chemical stability. The use of polymeric materials has led to the development of a broad range of techniques, which provide high throughput and high-resolution patterning. PDMS was used

here as the preferred dielectric option because it is inert, non-toxic, non-flammable and optically clear, based on the dielectric barrier discharge (DBD) mode of activation.

1.8 Theory of volt-ampere characteristics

Recently, the generation of small size plasmas in the range of μm to mm has received considerable attention due to their unique feature and actual size in various applications, including UV light sources, plasma display panels, gas analysis, surface treatment and gas analysis. Microcavity plasma devices are not restricted to dc operation and have been successfully operated using pulsed excitation as well as ac and rf excitation. An illustration of a typical volt-ampere characteristic of a plasma discharge is shown in the figure 1.4 below. It shows different V-I regimes. Region AB is the region in which electrons and ions are created by background radiation; the current is very low in this regime because background radiation cannot produce significant densities of charged species.

The region BC is the saturation current regime. Here the current does not respond to an increase of voltage. In region CD the applied voltage becomes high enough, thus producing an appreciable current up to point D. The discharge current collapses when the ion source is removed, a term called non self-sustaining regime. Going from D to E, a small increment in voltage will produce and exponential increase in current due to the state of the discharge. The electrons are accelerated and ionise another atom before reaching the anode.

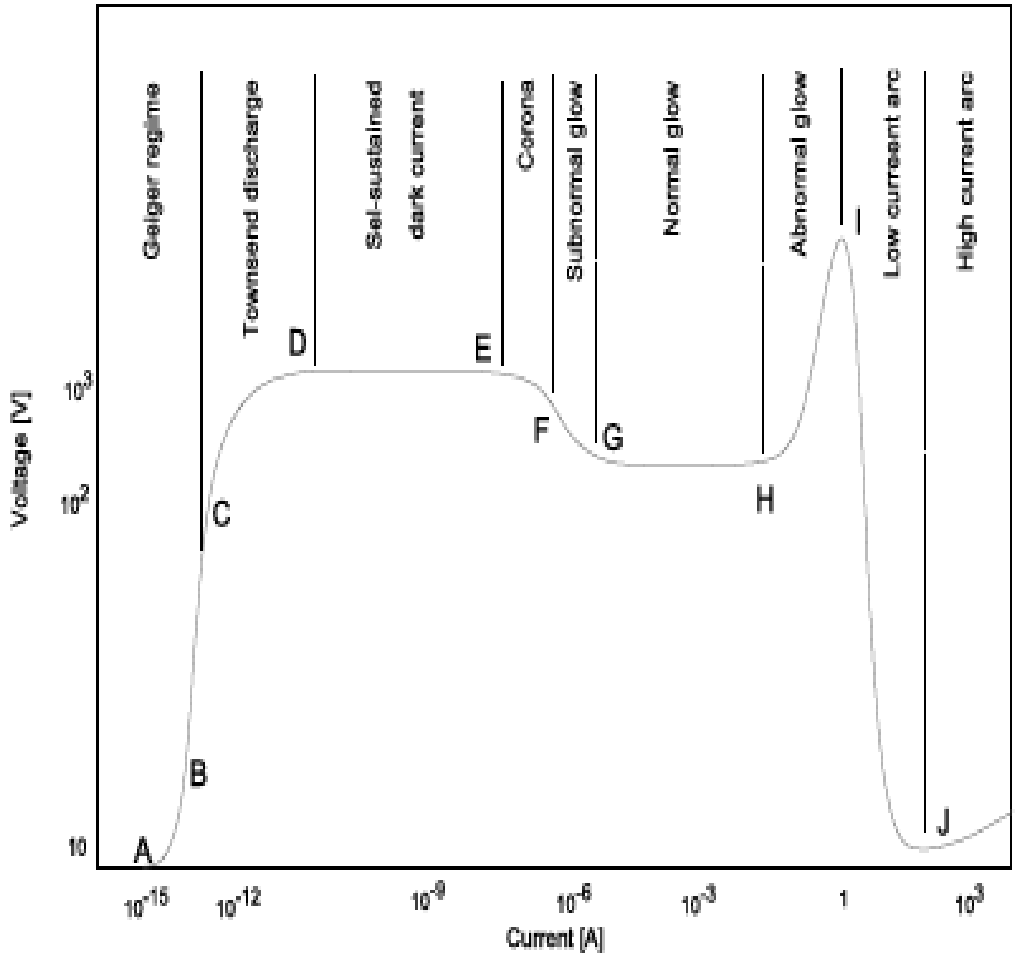

Figure 1.4. Types of discharges (Volt-ampere characteristic)

The gas subsequently breaks down when the voltage across the gap is greater than the ionisation potential of the gas. Region AD is called the Geiger regime.

Point F is later on reached, called the corona regime, and this happens when a further increase in current occurs. The discharge enters the region called the subnormal glow regime (point G), due to a further increase in discharge current, and this later ends up in a plateau that gives

origin to a normal glow discharge (point H). Here, almost all the low pressure plasma applications take place. As the voltage keeps increasing, the discharge enters the abnormal glow regime (point I) in which the current does not increase as fast as in the normal glow. After this point the voltage falls rapidly while the current increases even further, until finally, when the discharge has made the transition from a glow to an arc.

1.9 Paschen's Law

This examines the relationship between the breakdown voltage of parallel plates in a gas as a function of pressure and the gap distance. It is observed that the voltage necessary to arc the gap decreases up to a point as the pressure is reduced and then increases gradually, thus exceeding its original value. Also, it has been observed from numerous studies that decreasing the gap with normal pressure caused the same behaviour in the voltage required to cause an arc. Paschen's law is given by the expression below, where V is the breakdown voltage in Volts, p is the pressure in atmospheres and d is the gap distance in meters. a and b are constants which depend on the composition of the gap.

$$V = \frac{a(pd)}{\ln(pd) + b}. \qquad (1.1)$$

By differentiating equation 1.1 with respect to pd, and setting the derivative to zero, the minimum voltage can be calculated with the expression $pd = e^{1-b}$. It has been shown that for air at standard atmospheric pressure of 760 Torr, a = $43.6*10^6$ V/atm-m and b = 12.8. This yields and predicts the minimum arc voltage of 137 Volts for argon at a larger than 12 micrometers [86, 87].

CHAPTER TWO

2.0 Plasma confinement and discharge characteristics

Abstract

In this chapter, the author attempts to discuss some fundamental concepts on plasma confinement leading to the establishment and sustenance of stable discharges. Effort is made to outline the difficulties in the development of a model for a microplasma discharge. The major problem being the scaling of those processes happening close to the walls. Although there are very few publications on the simulation of plasma microdevices that help gain insight into how to tackle these problems, it is important to understand the theory and phenomenon of gas/microplasma behaviour in a confined environment.

2.1 High-Pressure Microdischarges

Microplasmas are also known as microcavity plasmas that have unique properties and represent systems with new and fascinating challenges for plasma science such as possible breakdown of pd scaling and the increasing dominance of boundary-dominated phenomena. The spatial confinement atmospheric-pressure, non equilibrium plasmas to dimensions of 1mm or less is a great approach to the generation and maintenance of stable glow discharges. Pulsed excitation on a submicrosecond time scale results in microplasmas with significant shifts in energy distribution functions of ions and electrons. This allows for the selective production of chemically reactive species and opens the door to a wide range of new applications in areas such as biomedicine, biology as well as gas and surface analysis.

Applications of microdischarges often require the use of two-dimensional arrays of individual microdischarges, either operated in parallel or in series, or both.

2.2 Plasma confinement

In a micro channel plasma reactor the ratio of surface area to volume is very high, so it is expected that processes at the walls come to the forefront. Therefore methods of confinement must be sought in order to reduce the possibility of interaction of plasma species with the walls. Basically, magnetic and inertial confinements are the most common methods of confining plasmas. For obvious reasons, focus is made on magnetic confinement methods. In general terms, magnetic confinement increases the number densities of direct current (DC) and radiofrequency (RF) discharges, which leads to improved ionisation yields, depending on the chemical process involved. Roth, 1995 suggests that magnetic fields parallel to the walls can reduce wall bombardment by charged particles and associated sputtering, thereby lowering the purity concentrations. In addition, magnetic fields may improve the operational stability of a microreactor. Applications where magnetic fields are applied work best when the magnetic moment is an approximate constant of motion and the condition (2.1) is met. A condition with Shohet refers to as adiabatic.

$$\frac{m\nu_{\perp}}{eBZ_0} << 1 \qquad (2.1)$$

Where $\nu_{\perp}$ denotes the transverse velocity, B the magnetic flux, m the mass of the particle, e is the elementary charge and Z_0 is the characteristic length of the magnetic field gradient. For microplasma which holds a B of around 10^{-3}.Tesla, the ratio expressed in equation 2.1 has a value of approximately 10^{-2}. Also the following two criteria must apply.

$$\omega_c \tau = \frac{eB}{m\nu_c} >> 1 \tag{2.2}$$

$$a > r_L = \frac{m\nu_\perp}{eB} \tag{2.3}$$

a denotes the plasma radius, r_L is the gyro-radius of the particle, τ is the collisional time and ν_c is the collision frequency. Condition (2.2) requires a charged particle to perform many gyrations before it collides, and condition (2.3) requires that the Larmor radius r_L of a charge species to be smaller than the plasma radius.

2.3 Electrical Breakdown

A gas is a very good insulator under normal conditions, but it undergoes a transition from an electrically insulating state to a conducting state, in which a small ionisation current can be greatly amplified when a sufficiently large potential difference is applied to it. The transition to a conducting state is termed "electrical breakdown" of the gas. A study of electrical breakdown, besides providing information concerning the fundamental atomic and molecular collision processes responsible for ionization growth, also contributes to the design of many important devices in modern electronics, for example, inductive and capacitive coupled plasma reactors, gas lasers, etc. Due to the geometrical characteristics of a microchannel plasma reactor, it is absolutely crucial to acquire a deep understanding of those ionisation processes leading to a self-sustained discharge. The fundamental collision processes which can contribute to the growth of ionization have been understood for a long time, but it is

important to elucidate which of these processes are important under any given conditions and to determine by what means they interact in order to produce a current growth. Secondary particles are ejected from metal surfaces by the potential energy associated with excited and metastable atoms. The lifetime of an excited atom is typically of the order of 10^{-8} s or less, and because of their short lifetime they will normally play a limited role in ionization phenomena. Metastable atoms, on the other hand, can only return to the ground state by collisions with another body and subsequent reversal to the ground state, and have typical lifetimes of the order of 10^{-3}s.

2.4 Microplasma Properties

Diagnostic studies of various microplasmas have been carried out using a variety of established techniques ranging from electrical characterization to various optical diagnostics methods and plasma mass spectrometry. These include time-averaged and time-resolved studies. The basic parameters that characterize microplasmas include I-V characteristics, electron density, and temperature, as well as electron energy distribution, radiative properties and gas temperature. Excitation of microplasmas in various configurations can occur by direct current (dc), pulsed dc, alternating current (dc), radiofrequency (rf), and microwave sources.

2.5 Electron Temperature & Energy Distribution

The increase in electron temperature, which is often correlated to an increase in electron density, is attributed to pulsed electron heating [63]. Measurements of the electron temperature in rare gas microplasmas have been carried out using emission spectroscopy.

The simple fact that microplasmas are efficient sources of excimer radiation points to the presence of a significant fraction of high-energy electrons (with energies exceeding the

excitation and ionization energies of the rare gas atoms, i.e. above at least 12eV in Xe and more than 21eV in Helium (He)). Thus, the electron energy distribution function contains a significant amount of very energetic beam electrons, and must be high non-Maxwellian. Earlier diagnostics studies [74] of this distribution function in low-pressure HC discharges found evidence of copious amounts of electrons with energies well above 10eV and a tail extending up to the plasma operating voltage. This observation is supported by Kurunczi et al [3, 74] of the intense Ne_2 and He_2 excimer emissions from microdischarges in pure Ne and He, which requires copious amounts of electrons with energies of at least 17eV in Ne and 21eV in He.

2.6 Plasma Chemistry

Primary ionisation - Considering a pure gas at a pressure p, under a field E, free electrons travel through a gas along the electric field with the drift velocity. The state of energy of the gas is a unique function of E/p (Brown, 1966) which is termed the reduced field. This reduced field is also given as E/n when a state law is used to relate the gas pressure to the number density. Because electron velocities spread over a wide range, a certain portion of free electrons will acquire sufficient energy to knock off more electrons out of atoms and molecules. The Townsend primary ionisation coefficient, α, is defined as the average number of ionising collisions an electron undergoes in travelling a unit distance in the direction of the field. The mean free path, defined as the distance between collisions, is inversely proportional to the gas pressure p, so the probability of ionisation per collision will be proportional to the ratio α/p. Thus α/p will be a unique function of E/p. Excitation - In travelling through the gas, electrons will also undergo excitation collisions with gas molecules. By analogy with the α

coefficient we may define an excitation coefficient α' as the average number of excitation collisions undergone by an electron in traveling a unit distance in the direction of the field.

Recombination. In a partially ionized gas there will be collisions between electrons and positive ions that may result in neutralisation to form neutral gas atoms or molecules, thus removing charged particles from the gas (Arnot, 1933). The rate of recombination will be proportional to the product of the electron and ions densities $n_e n_p$ we may define a recombination S such that $n_e n_p$ is the probability per unit volume per unit time of an electron and ion recombining.

$$\left(\frac{\partial n_e}{\partial t}\right)_{recomb} = \left(\frac{\partial n_p}{\partial t}\right)_{recomb} = -S n_e n_p \qquad (2.4)$$

Since the rate of recombination is proportional to the product of n_p and n_e, it will not be of importance at small ionisation densities (small number densities of electrons and ions). The probability of recombination will depend on the time an electron is within the interaction range of the ion, thus, S will be a decreasing function of electron energy (Kunhardt and Luessen, 1981). If, in addition, negative ions are present in a gas, recombination will also be possible between the negative and positive ions. Electrons may be lost from a region of a gas by attachment to neutral gas molecules forming negative ions. An attachment coefficient β is defined as the probability of attachment per unit distance travelled by an electron in the direction of the field, so that attachment will have the effect of reducing the number of ionizations per unit distance from α to α−β. The coefficient α−β is sometimes called the effective primary ionization coefficient α_{eff}. Attachment will be of particular importance in

electronegative gases where the potential energy of the negative ions is smaller that that of the atom or molecule in its normal state.

Detachment: This is the reverse process to attachment; in which negative ions will have a probability μ of detaching per unit time to give an electron and a neutral atom or molecule, hence the reciprocal of this probability $1/\mu$ is thus the mean lifetime of a negative ion.

Positive ion Ionisation: The early work by Townsend (1903) not only considered ionisation of gas molecules by electrons but also by positive ions produced in the body of the gas. He defined an ionization coefficient S as the average number of ionizing collisions per unit distance travelled by a positive ion in the direction of E, and (like α/p) S/p is a unique function of E/p. Here we shall consider this process because of its historical importance, but it is now accepted that in all fields normally met with in the laboratory its contribution is negligible compared with the contributions of other possible processes suggested by Morgan, (1965). Positive ion energies $\geq$ 300eV are necessary before any appreciable ionisation can be detected. So given the conditions of a microchannel plasma reactor, this process is not of any practical relevance. There are a number of additional ionisation processes to be considered when the gas is not pure or is a mixture of pure gases.

2.7 Initiation of the discharge

In order to understand the various ionisation processes that can occur at metal surfaces in a gas, it is important, to consider two plane parallel electrodes, separated by a distance d, immersed in a gas at pressure p. A uniform Electric field (E) is produced when a potential difference V is applied between the electrodes. In any gaseous discharge it is necessary to have

some active particles, normally free electrons, present in the discharge space in order to initiate the ionisation process. These particles may be produced, for example, by background ionisation of gas molecules by cosmic rays or by field, photo, or thermionic emission from the cathode surface.

The generation of secondary emission due to the incidence of positive ions on the cathode: - Electrons drifting in the field E will undergo ionizing collisions with gas molecules producing one further electron and one positive ion in such collision. These positive ions will drift back to the cathode where they may eject secondary electrons by virtue of either their kinetic or potential energies. The details of the ejection mechanisms are discussed fully in the literature and we shall simply assume that each ion incident on the cathode will have a probability γ_i of producing secondary electrons at a particular field and gas pressures. Since each ion is generated in an ionizing collision, γ_i may also be defined as the probability that a secondary electron is produced per ionising collision in the gas.

Secondary electron emission due to the incidence of photons on the cathode: - A fraction of the photons produced (by excitation collisions of the primary electrons) in any region of the gas will sooner or later arrive at the cathode surface where the photons will have a fixed probability of producing a secondary electron by the photoelectric effect. Each photon will have a certain energy $h\nu$ associated with it and may be a resonance or non-resonance photon. In the latter case it will reach the cathode after a delay time of the order of the lifetime of the excited atom ($\approx 10^{-8}$s), while a resonance photon may have a considerable delay time due to its repeated absorption and scattering. For photons of a given energy and delay time we may define a secondary emission coefficient δ as the probability of the production of a secondary

electron by this type of photon per unit distance. The coefficient δ incorporates a factor representing the fraction of the photons, emitted at a given point in space, which reach the cathode. It is normal practice in the consulted literature to represent this secondary process by a coefficient γ_{ph} (sometimes written as δ/α), which denotes the probability of production of a secondary electron per ionizing collision. If there is a number of different species of photons having different energies and delay times, then there will be a series of coefficients γ^1_{ph}, γ^2_{ph} ... with associate delay times τ^1_{ph}, τ^2_{ph}, etc.

Secondary electron emission due to the incidence of metastable and ex-cited atoms on the cathode: - Excited and metastable atoms produced in the body of the gas will diffuse at a rate determined by the neutral gas density (and the flow velocity in flowing systems), and a fraction of those produced in a given region of the discharge space will eventually reach the cathode, where they can cause a secondary electron to be emitted. Obviously, in general this process will be more probable for metastable atoms because of their greater lifetime, so that there is much less likelihood of their decaying before reaching the electrodes. As in the previous cases, we may define coefficients γ_m (for metastables) and γ_{ex} (for excited atoms) as the probability of the production of a secondary electron per ionizing collision of the primary electron. Mathematically, there is no difference between the two processes apart from the different lifetimes involved. The coefficients γ_m and γ_{ex} will be functions of the distance from the cathode due to geometric effects and to the greater probability of an atom returning to the ground state the further away from the cathode it is created. The distance dependence will be especially important when the lifetimes are of the order of the time the particles take to diffuse across the electrodes separation.

2.8 Ionization by electrons and secondary ionisation by positive ions in the gas.

Townsend (1903) obtained an expression for the current flowing in the discharge gap considering the contribution of all the processes mentioned above, so that the total current, I, flowing in the discharge space is given by

$$I = \frac{I_0 e^{\alpha d}}{1 - \gamma_T \left(e^{\alpha d} - 1\right)} \tag{2.5}$$

Equation 2.5 is known as the Townsend equation. $\gamma_T = \gamma_i + \gamma_{ph} + \gamma_m + \gamma_{ex}$ is the generalized Townsend secondary coefficient. The Townsend equation is valid for infinite plane parallel electrodes and will also be accurate provided that the cross-section of the discharge is small compared with the electrode area. Strictly speaking, even for finite electrodes, the coefficients γ_m and γ_{ex} may be functions of distance, since metastable atoms and excited atoms that are created a large distance away from the cathode will have a smaller probability of arriving there before decaying, than those produced in the neighbourhood of the cathode (Kunhardt and Luessen, 1981). Furthermore, metastable and excited atoms produced near the anode will have a high probability of diffusing to the anode and being absorbed, thus being removed from the discharge.

Breakdown criterion. The condition when the current increases without limit occur when

$$\gamma_T \left(e^{\alpha d} - 1\right) = 1 \tag{2.6}$$

This is the familiar Townsend "breakdown criterion", and the value of the applied voltage for which it is satisfied (at a fixed value of the electrode separation d) is called the "breakdown potential".

2.9 Breakdown Potential

The breakdown potential is the minimum voltage that will maintain a small current in a distance gap without any additional sources (self sustained discharge). The left hand side of Eq. (2.6) represents the average number of secondary electrons produced by an electron leaving the cathode and traveling to the anode. Thus the breakdown criterion must be interpreted physically as a replacement condition in which every electron leaving the cathode produces, on the average, one secondary electron. We note that the definition of γ_T given above is independent of the value of the current flowing in the gap, the only restriction being that the current should not be so large as to produce appreciagble space-charge distortion of the electric field [88].

References

1. C. Tendero, C. Tixier, P. Tristant, J. Desmaison, P. Leprince, Spectrochimica Acta Part B 61 (2006) 2 – 30

2. H. Conrads, M. Schmidt, Plasma generation and plasma sources, Plasma Sources Sci. Technol. 9 (2000) 441–454.

3. S.-J. Park, K.F. Chen, S.H. Sung, J. SID 13 (2005) 949.

4. K.H. Becker, K.H. Schoenbach, J.G. Eden, J. Phys. D: Appl. Phys. 39 (2006) R55.

5. J.W. Frame, D.J. Wheeler, T.A. DeTemple, Appl. Phys. Lett. 71 (1997) 1165.

6. J.G. Eden, S.-J. Park, N.P. Ostrom, J. Display Tech. 1 (2005) 112.

7. S.-J. Park, K.-S. Kim, J.G. Eden, J. Appl. Phys. 99 (2006) 026107.

8. S.-J. Park, P.A. Tchertchian, S.H. Sung, IEEE Trans. Plasma Sci. 35 (2007) 215.

9. M. Lu, S.-J. Park, B.T. Cunningham, J. Microelectromech. Syst. 16 (2007) 1397

10. J.C.T. Eijkel, H. Stoeri, A. Manz,An atmospheric pressure dc glow discharge on a microchip and 1st application as a molecular emission detector, J. Anal. At. Spectrom. 15 (2000) 297–300.

11. J.C.T. Eijkel, H. Stoeri, A. Manz, A dc microplasma on a chip employed as an optical emission detector for gas chromatography, Anal. Chem. 72 (2000) 2547–2552.

12. H.J. Kim, Y.A. Woo, J.S. Kang, S.S. Anderson, E.H. Piepmeier, Microchim. Acta. 134 (2000) 1–7.

13. F.G. Bessoth, O.P. Naji, J.C.T. Eijkel, A. Manz, Towards an on-chip gas chromatograph: the development of a gas injector and a dc plasma emission detector, J. Anal. At. Spectrom. 17 (2002) 794–799.

14. T. Cserfalvi, P. Mezei, P. Apai, Emission studies on a glow discharge in atmospheric

pressure air using water as a cathode, J. Phys. D 26 (1993) 2184–2188.

15. P. Mezei, T. Cserfalvi, M. Janossy, Pressure dependence of the atmospheric electrolyte cathode glow discharge spectrum, J. Anal. At. Spectrom. 12 (1997) 1203–1208.

16. P. Mezei, T. Cserfalvi, M. Janossy, Szöcs, H.J. Kim, Similarity laws for glow discharges with cathodes of metal and an electrolyte, J. Phys. D 31 (1998) 2818–2825.

17. T. Cserfalvi, P. Mezei, Subnanogram sensitive multimetal detector with atmospheric electrolyte cathode glow discharge, J. Anal. At. Spectrom. 18 (2003) 596–602.

18. H.J. Kim, J.H. Lee, M.Y. Kim, T. Cserfalvi, P. Mezei, Development of open-air type electrolyte-as-cathode glow discharge-atomic emission spectrometry for determination of trace metals in water, Spectrochim.Acta Part B 55 (2000) 823–831.

19. W.C. Davis, R.K. Marcus, An atmospheric pressure glow discharge optical emission source for the direct sampling of liquid media, J. Anal. At. Spectrom. 16 (2001) 931–937.

20. R.K. Marcus,W.C. Davis, An atmospheric pressure glow discharge optical emission source for the direct sampling of liquid media, Anal. Chem. 73 (2001) 2903–2910.

21. W.C. Davis, R.K. Marcus, Role of powering geometries and sheath gas composition on operation characteristics and the optical emission in the liquid sampling-atmospheric pressure glow discharge, Spectrochim. Acta Part B 57 (2002) 1473–1486.

22. M.R. Webb, F.J. Andrade, G. Gamez, R. McCrindle, G.M. Hieftje, Spectroscopic and electrical studies of a solution-cathode glow discharge, J. Anal. At. Spectrom. (2005) 1218

23. Y. Yin, J. Messier, J.A. Hopwood, Miniaturization of inductively coupled plasma sources, IEEE Trans. Plasma. Sci. 27 (1999) 1516

24. J.A. Hopwood, Microfabricated inductively coupled plasma generator, J. Microelectromech. Syst. 9 (2000) 309–313.

25. F. Iza, J. Hopwood, Influence of operating frequency and coupling coefficient on the

efficiency of microfabricated inductively coupled plasma sources, Plasma Sources Sci. Technol. 11 (2002) 229–235.

26. D. Liang, M.W. Blades, Atmospheric-pressure capacitively coupled plasma spectral lamp and source for the direct analysis of conducting solid samples, Spectrochim. Acta Part B 44 (1989) 1049–1057.

27. M.W. Blades, The response of the inductively-coupled argon plasma to solvent plasma load-spatially-resolved maps of electron-density obtained from the intensity of one argon line, Spectrochim. Acta Part B 49 (1994) 1231–1250.

28. S.D. Anghel, T. Frentiu, E.A. Cordos, A. Simon, A. Popescu, Atmospheric pressure capacitively coupled plasma source for the direct analysis of nonconductive solid samples, J. Anal. At. Spectrom. 14 (1999) 541–545.

29. S.Y. Lu, C.W. LeBlanc, M.W. Blades, Analyte ionization in the furnace atomization plasma excitation spectrometry source—spatial and temporal observations, J. Anal. At. Spectrom. 16 (2001) 256–262.

30. A. Bass, C. Chevalier, M.W. Blades, A capacitively coupled microplasma (CC mu P) formed in a channel in a quartz wafer, J. Anal. At. Spectrom. 16 (2001) 919–921.

31. H. Yoshiki, Y. Horiike, Jpn. J. Appl. Phys. 40 (2001) L360–L362.

32. A.M. Bilgic, E. Voges, U. Engel, J.A.C. Broekaert, A low-power 2.45 GHz microwave induced helium plasma source at atmospheric pressure based on microstrip technology, J. Anal. At. Spectrom. 15 (2000) 579–580.

33. A.M. Bilgic, U. Engel, E. Voges, M. Kückelheim, J.A.C. Broekaert, A new low-power microwave plasma source using microstrip technology for atomic emission spectrometry, Plasma Sources Sci. Technol. 9 (2000)1–4.

34. J. Hopwood, F. Iza, Ultrahigh frequency microplasmas from 1 pascal to 1

atmosphere, J. Anal. At. Spectrom. 19 (2004) 1145–1150.

35. J. Franzke, K. Kunze, M. Miclea, K. Niemax, Microplasmas for analytical spectrometry, J. Anal. At. Spectrom. 18 (2003) 802–807.

36. C. Penache, M. Miclea, A. Bräuning-Demian, O. Hohn, S. Schössler, T. Jahnke, K. Niemax, H. Schmidt-Böcking, Characterization of a highpressure microdischarge using diode laser atomic absorption spectroscopy, Plasma Sources Sci. Technol. 11 (2002) 476–483.

37. M. Miclea, K. Kunze, G. Musa, J. Franzke, K. Niemax, The dielectric barrier discharge — a powerful microchip plasma for diode laser spectrometry, Spectrochim. Acta Part B 56 (2001) 37–43.

38. K. Kunze, M. Miclea, G. Musa, J. Franzke, C. Vadla, K. Niemax, Diode laser-aided diagnostics of a low-pressure dielectric barrier discharge applied in element-selective detection of molecular species, Spectrochim. Acta Part B 57 (2002) 137–146.

39. M. Miclea, K. Kunze, J. Franzke, K. Niemax, Plasmas for lab-on-the-chip applications, Spectrochim. Acta Part B 57 (2002) 1585–1592.

40. K. Kunze, M. Miclea, J. Franzke, K. Niemax, The dielectric barrier discharge as a detector for gas chromatography, Spectrochim. Acta Part B 58 (2003) 1435–1443.

41. Z. Zhu, S. Zhang, J. Xue, X. Zhang, Application of atmospheric pressure dielectric barrier discharge plasma for the determination of Se, Sb and Sn with atomic absorption spectrometry, Spectrochim. Acta Part B 61 (2006) 916–921.

42. R.J. Skelton Jr., H.-C.K. Chang, P.B. Farnsworth, K.E. Markides, M.L. Lee, Radio-frequency plasma detector for sulfur selective capillary gaschromatographic analysis of fossil-fuels, Anal. Chem. 61 (1989) 2292–2298.

43. J.A.C. Broekaert, The development of microplasmas for spectrochemical analysis, Anal. BioAnal. Chem. 374 (2002) 182–187.

44. J. Franzke, K. Kunze, M. Miclea, K. Niemax, Microplasmas for analytical spectrometry, J. Anal. At. Spectrom. 18 (2003) 802–807.

45. Karanassios, Microplasmas for chemical analysis: analytical tools or research toys? Spectrochim. Acta Part B 59 (2004) 909–928.

46. J.A.C. Broekaert, V. Siemens, Some trends in the development of microplasmas for spectrochemical analysis, Anal. BioAnal. Chem. 380 (2004) 185–189.

47. J.R. Roth, Industrial plasma engineering, Principles, vol. 1, IOP Publishing, Philadelphia, 1995.

48. U. Kogelschatz, B. Eliasson, W. Egli, From ozone generators to flat television screens: history and future potential of dielectric-barrier discharges, Pure Appl. Chem. 71 (1999) 1819–1828.

49. A. Sobel, Plasma displays, IEEE Trans. Plasma. Sci. 19 (1991) 1032–1047.

50. U. Kogelschatz, B. Eliasson, M. Hirth, Ozone generation from oxygen and air — discharge physics and reaction-mechanisms, Ozone: Sci. Eng. 10 (1988) 367–377.

51. B. Eliasson, U. Kogelschatz, UVexcimer radiation from dielectric-barrier discharges, Appl. Phys., B 46 (1988) 299–303.

52. B.M. Penetrante, R.M. Brusasco, B.T. Merritt, G.E. Vogtlin, Pure Appl. Chem. 71 (1999) 1829–1835.

53. B.M. Penetrante, M.C. Hsiao, J.N. Bardsley, B.T. Merritt, G.E. Vogtlin, A. Kuthi, C.P. Burkhart, J.R. Bayless, Plasma Sources Sci. Technol. 6 (1997) 251–259.

54. G. Borcial, C.A. Anderson, N.M.D. Brown, Plasma Sources Sci. Technol.12 (2003) 335–344.

55. Z. Hubiccka, M. Cad, M. Sicha, A. Churpita, P. Pokorný, L. Soukup, L. Jastrabik, Plasma Sources Sci. Technol. 11 (2002) 195–202.

56. O. Goossens, E. Dekempeneer, D. Vangeneugden, R. Van de Leesta, Surf. Coat. Technol. 142–144 (2001) 474–481.

57. R. Guchardi, P.C. Hauser, A capacitively coupled microplasma in a fused silica capillary, J. Anal. At. Spectrom. 18 (2003) 1056–1059.

58. M. Laroussi, X. Lu, Room-temperature atmospheric pressure plasma plume for biomedical applications, Appl. Phys. Lett. 87 (2005) 113902.

59. G.A. Eiceman, Z. Karpas, Ion Mobility Spectrometry, 2nd Ed.CRC Press,London, UK, 2005.

60. W. Vautz, D. Zimmermann, M. Hartmann, J.I. Baumbach, J. Nolte, J. Jung, Ion mobility spectrometry for food quality and safety, Food Addit. Contam. 23 (11) (2006) 1064–1073.

61. W. Vautz, J.I. Baumbach, J. Jung, Beer fermentation control using ion mobility spectrometry, J. Inst. Brew. 112 (2006) 157–164.

62. M. Westhoff, P. Litterst, L. Freitag, B. Obertrifter, V. Ruzsanyi, J.I. Baumbach, Ion mobility spectrometry — a new method in the diagnostic approach to sarcoidosis?-Preliminary data, Eur. Respir. J. 28 (2006) 111S.

63. J.I. Baumbach, M. Westhoff, Ion mobility spectrometry to detect lung cancer and airway infections, Spectrosc. Eur. 18 (2006) 22–27.

64. Schoenbach K.H., El-Habachi A., Shi W., Ciocca M., High-pressure hollow cathode discharges, Plasmas Sources Sci. Technol. 6 (1997) 468-477.

65. Karanassios V., Johnson K and Smith A. T. (2007); Micromachined, planar-geometry, atmospheric-pressure, battery-operated microplasma devices (MPDs) on chips for analysis of microsamples of liquids, solids, or gases by optical-emission spectrometry, Journal of Anal. Bioanal Chem, Vol. 388, pp 1595 – 1604

66. Czerfalvi T., Mezei P., Apai P., Emission studies on a glow discharge in atmospheric pressure air using water as a cathode, J. Phys. D: Appl. Phys. 26 (1993) 2184-2188

67. P. Fauchais, A. Vardelle, Les applications innovantes des plasmas thermiques dans l'industrie, Les guides de l'innovation NOVELECT/EDF R&D. NOV001E2003, 2003, 54 pp.

68. Y. Kabouzi, M.D. Calzada, M. Moisan, K.C. Tran, C. Trassy, Radial contraction of microwave-sustained columns at atmospheric pressure, J. Appl. Phys. 91 (3) (2002) 1008 – 1019

69. Stillahn J. M., Trevino K. J. and Fisher E. R. (2008); Plasma Diagnostics for Unraveling Process Chemistry, Proceedings of the annual review analytical chemistry journal, Vol. 1, pp 261 – 291

70. Kroesen et al (1999); Dusty plasmas: fundamental aspects and industrial applications, in H. Schluter, A. Shivarova (Eds.), Advanced Technologies Based on Wave and Beam Generated Plasmas, NATO Science Series, vol. 67, pp. 175-190.

71. Eijkel J C T, Stoeri H and Manz A 1999 A molecular emission detector on a chip employing direct current microplasma *Anal. Chem.* **71** 2600–6

72. Eijkel J C T, Stoeri H and Manz A 2000 A dc microplasma on a chip employed as an optical emission detector for gas chromatography *Anal. Chem.* **72** 2547–52

73. von Engel A 1965 *Ionized Gases* (Oxford: Oxford University Press)

74. Eijkel J C T, Stoeri H and Manz A 2000 An atmospheric pressure dc glow discharge on a microchip and its application as a molecular emission detector *J. Anal. At. Spectrom.* **15** 297–300

75. Manz A, Graber N and Widmer H M 1990Miniaturized totalchemical-analysis systems—a novel concept for chemical sensing *Sensors Actuators* B **1** 244–8

76. Cserfalvi T, Mezei P and Apai P 1993 Emission studies on a glow-discharge in atmospheric-pressure air using water as a cathode *J. Phys. D: Appl. Phys.* **26** 2184–8

77. Kim H J, Lee J H, Kim M Y, Cserfalvi T and Mezei P 2000 Development of open-air type electrolyle-as-cathode glow discharge-atomic emission spectrometry for determination of trace metals in water *Spectrochim Acta* B **55** 823–31

78. Cserfalvi T and Mezei P 1996 Operating mechanism of the electrolyte cathode atmospheric glow discharge *Fresenius J. Anal. Chem.* **355** 813–9

79. Marcus R K and DavisW C 2001 An atmospheric pressure glow discharge optical emission source for the direct sampling of liquid media *Anal. Chem.* **73** 2903–10

80. DavisW C and Marcus R K 2001 An atmospheric pressure glow discharge optical emission source for the direct sampling of liquid media *J. Anal. At. Spectrom.* **16** 9317

81. StjernstromM and Roeraade J 1998 Method for fabrication of microfluidic systems in glass *J. Michromech.Microeng.* **8** 33–8

82. Pearse R W B and Gaydon A G 1950 *The Identification of Molecular Spectra* (London: Chapman and Hall)

83. Cserfalvi T and Mezei P 1994 Direct solution analysis by glow-discharge—electrolyte cathode discharge spectrometry *J. Anal. At. Spectrom.* **9** 345–9

84. H. Becker, L.E. Loccascio, Polymer microfluidic devices,Talanta 56 (2002), pp 267

85. Eijkel J.C.T., Stori H., Manz A., A dc microplasma on a chip employed as an optical emission detector for gas chromatography, Anal. Chem. 72 (2000) 2547-2552.

86. University of Rochester, Course Handout

87 Gottscho R A and Miller T A 1984 *Pure Appl. Chem.* **56** 189

88 Dendy, R.O. Plasma particle dynamics, The 40th Culham plasma physics summer school, UKAEA Fusion (2003).

CHAPTER THREE

3.0 Experimental Settings and Methods

Abstract

This chapter presents a brief discussion on the equipment settings and the main characterization techniques used to analyse the plasma as well as the modified surfaces. These equipments and techniques were used to obtain qualitative and quantitative information about the plasma discharge characteristics as well as the chemical composition, surface morphology and energy of polystyrene (PS) samples used. The results obtained are presented in the following chapters.

3.1 Power Supply

The applied voltage is generated from a power supply consisting of a signal generator, an HQ Audio Power amplifier – VPA 2350MB and a 2 kHz to 50 kHz, 10kV peak to peak (p-p) express step-up transformer. Measurement of the voltage and current outputs were provided by a 15kV p-p, 50MHz high voltage probe, a 30A TCP312 current probe used with a Tektronix TCPA 300 current probe amplifier and a DPS3034 Tektronix oscilloscope. The applied voltage V_{app} (t) was measured with the aid of a 15 kV, 50MHz High voltage probe. The discharge current was obtained by subtracting the traces of the displacement current from the total current and compared it with the measured voltage drop across a shunt resistor R = 50 Ω connected in series with an unbiased electrode and ground using a current probe.

3.2 Surface Characterisation Methods

3.2.1 Atomic Force Microscopy (AFM)

Atomic force microscopy (AFM) is an imaging technique that is useful for obtaining three-dimensional (3D) topographic information from conducting and insulating structures with lateral resolution down to 1.5 nm and vertical resolution down to 0.05 nm. Such samples include clusters of atoms and molecules as well as biological species (DNA and proteins). [1]. The first description of atomic force microscopy was published in 1986 by Binnig, [2] Quate and Gerber cited in [3]. AFM can operate in gas, ambient and fluid environments and can measure physical properties such as elasticity, adhesion, chemical functionality, friction and hardness of materials.

The AFM operates in three distinct modes, namely contact, non-contact and tapping mode .When the force microscope is operated in 'contact mode' (typically < 0.5 nm probe-surface separation), the tip and the sample remain in close contact as the scanning proceeds. [1, 4, 5]

The surface is scanned by a sharp tip, which is mounted on a soft spring, also referred to as 'cantilever'. [1] The sample is positioned on a piezoelectric tube ortripod, which controls the scanning motion. Features on the sample surface cause a deflection of the cantilever. This deflection is commonly measured by an optical beam technique in which the laser light is focused onto the end of the cantilever, and reflected onto a split photodiode. The feedback signal from the photodiode is used to control the height of the piezoelectric crystal as the sample is scanned.

The corresponding height adjustment signal is directly related to the topography of the surface. Interaction between the sample surface and the AFM tip is determined by the interaction between the molecules or atoms on the surface of the sample and the tip. The relevant forces in force microscopy (e.g. electrostatic forces, dipolar actions, van der Waals forces, H-bonding) have been summarized e.g. by Schönherr.[6]. The "non contact" mode (typically 0.1 – 10 nm probe-surface separation) is a mode where the cantilever is oscillated above the surface of the sample at a distance such that it is no longer in the repulsive regime but in the attractive regime of the inter-molecular force curve. The third mode of AFM operation is the tapping mode which typically has a probe-surface separation of 0.5 - 2 nm Unlike the operation of contact mode, where the tip is in constant contact with the surface, in tapping mode the tip only makes intermittent contact with the surface once in every vibration period. [1, 4, 5].

The AFM images presented in this thesis were done in tapping mode due to generation of image artefacts and the disruption of the surfaces in contact mode. This is because the plasma films on the modified polystyrene surfaces (PS) were seen to be rather soft. Since the tip only intermittently 'taps 'the surface, the tip-sample interactions (especially shear forces) are greatly reduced, which ensures minimal disturbance of the adsorbed molecules [7]. This technique has been used to image molecular packing and aggregation of proteins on surfaces such as silicon, [8] methylated silicon, [9] self-assembled monolayers, [10] spin-cast polymer films, [11] and on mica [12].

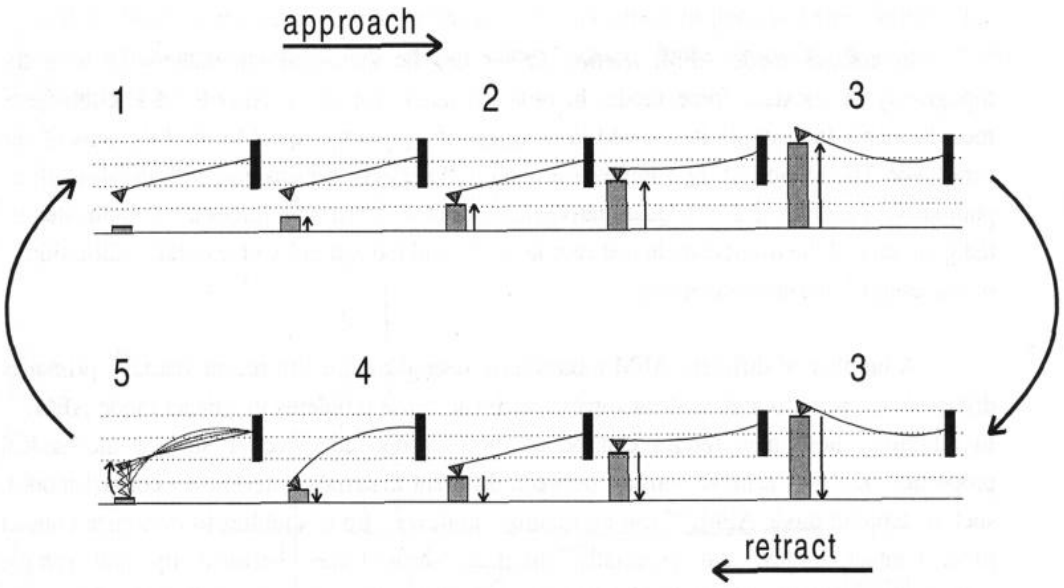

Figure 3.1 Schematic diagram of a force spectroscopy experiment. Adapted from Schönherr [6].

From figure 3.1, starting at position 1, the sample moves up but it is out of contact with the tip. In position 2, the cantilever spring constant is overcome by the gradient of the force, causing the tip to jump into contact. In position 3, the sample continues to move up, and causes the cantilever to deflect. The tip sticks to the surface during retraction if the attractive forces are greater than the repulsive forces. Finally in position 5, the tip snaps off when the force gradient overcomes the spring constant.

3.2.1.1 Atomic Force Microscopy (AFM) Measurement

Scanning probe microscopy was used to investigate the surface morphology of treated PS samples. This was carried out using a CP-II atomic force microscope (Veeco Instruments, USA). Tapping mode with phase imaging was used as opposed to contact mode, so as to avoid the possibility of surface damage to the samples. The probes were uncoated Si_3N_4 with a force constant of 40 N/m and a resonance frequency of 320 kHz (Windsor Scientific, UK). A

large (120 x 120 um) area scanner was used to accommodate various scan dimensions and the scans comprised of 256 x 256 points. The resulting scans were analyzed using WSxM SPM analysis software (Nanotec Electronica, Spain).

3.2.2 X-ray Photoelectron Spectroscopy (XPS)

The x-ray photoelectron spectroscopy (XPS) is also known as the electron spectroscopy for chemical analysis (ESCA) [13, 14]. It is a widely used technique to characterize plasma polymer surfaces (typically ± 3-10 nm). XPS is a powerful technique for the detection of variations in oxidation state and chemical compositions. It provides real time photoelectron imaging of the sample surface (showing only electrons of a chosen energy). When a sample is irradiated in vacuum with x-rays, the interaction between an x-ray photon and an inner-shell electron causes a complete transfer of the photon energy to the electron, which then has enough energy to leave the atom and escape from the surface (photoelectron) [13]. An element can be identified once the binding energy of a particular shell of the atom is known. The binding energy *Eb* of the inner-shell electron can be calculated from the difference between the known x-ray photon energy *hv*, and the kinetic energy *Ek* of the photoelectron, which is measured by an electron energy analyzer:

$$Eb = hv - Ek \qquad (3.1)$$

The photoelectron peaks are associated with a particular core level of a particular element. Subtle changes in the peak positions and shape can provide useful information on the changes in surface chemistry. The XPS machine provides elemental and chemical information about the surface region (first 1 – 30 monolayers) of nearly any solid material. It is useful for

chemically sensitive materials since damage caused by the x-ray beam is minimal. It is also particularly useful for insulating materials such as polymers, oxides and powders where charging effects limits other surface techniques. XPS is sensitive to the top 5 nm of a sample, and thus allows the detection of elemental composition as a function of depth due to the removal of surface layers by ion etching. Measurement results obtained here were carried out on a VSW ESCA X-ray photoelectron spectrometer at the Physics Department of Liverpool [15].

X-ray photoelectron spectroscopy (XPS) is one of the most important techniques for extracting information on the electronic and chemical states of materials. In XPS the energy of the exciting radiation places a limit on the binding energy of the electron energy levels that can be studied with the technique and there is increasing interest in developing high energy photon sources in order to probe deeper core levels [16–18] or to probe deeper below the surface by generating high kinetic energy photoelectrons from shallow core levels [19].

3.2.3 Contact Angle Goniometry

Contact angle measurements give information about the top several Angstrom (Å = 0.1 nm) of a plasma film. [20] The contact angle is defined as the angle between a solid surface and the tangent of the liquid-vapour interface of a liquid drop. [21] Contact angle measurements with water can be used to determine if a plasma film is hydrophilic (low contact angle) or hydrophobic (high contact angle). The measurements provide useful information on the surface composition that polymers undergo upon surface treatment, [22] aging, [23] or migration of functional groups in certain environments. [24]

To illustrate the difference between a hydrophilic and a hydrophobic surface (see figures 3.2 a and b), one polystyrene sample (PS) was treated with helium plasma for 20 seconds while the other was untreated. When a drop of water was placed on the treated surface, the contact angle changed from ~ 90 º to ~ 50 º. In static measurements, the angle θ is measured at a stationary liquid front. [13]

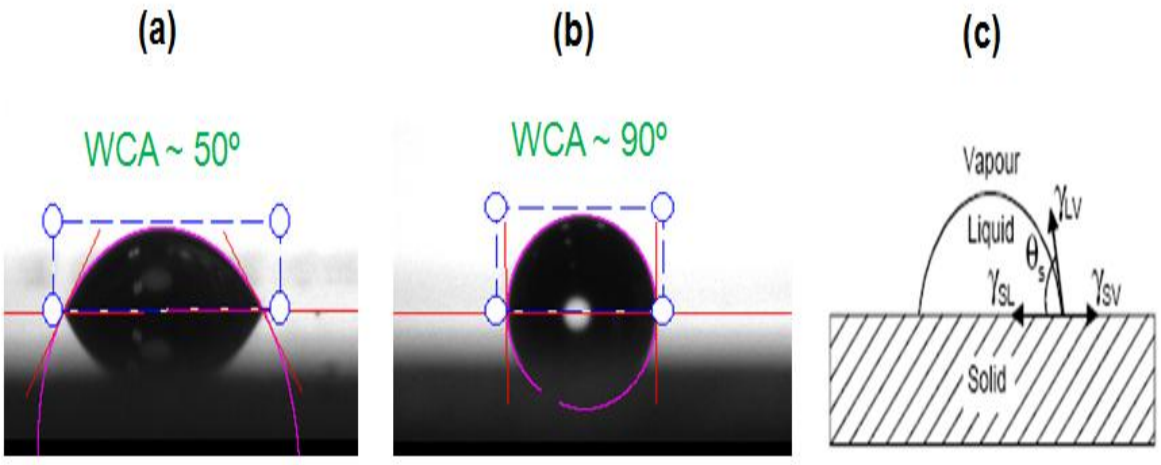

Figure 3.2: (a) Hydrophilic image of a sessile drop on PS surface after treatment. WCA ~ 50 º **(b)** hydrophobic image of a sessile drop for the untreated PS surface. WCA ~ 90 º. **(c)** Shows a schematic of the sessile drop on a solid surface.

Figure 3.2 c. shows a picture of a sessile drop on a solid surface. The contact angle depends on the force balance at the three-phase boundary, defined by Young's equation:

$$\gamma_{LV} \cos \theta = \gamma_{SV} - \gamma_{SL} \qquad (3.2)$$

where γ_{LV} is the surface tension of the liquid in equilibrium with its saturated vapour, γ_{SV} is the surface tension of the solid in equilibrium with the vapour, and γ_{SL} is the interfacial tension between the solid and the liquid. [13]

The wettability of the polymers, determined a few minutes after the plasma treatment, were characterised by depositing 2 μl of deionised water using a KSV CAM100 water contact angle measurement system. This system comprises a firewire video camera, a needle used to dispense a sessile-water droplet (~ 0.2 μL), a syringe holder, an adjustable sample stage and an LED light source. Droplets were positioned in the centre of the sample and ten images (at 1 frame/s) were captured 3 s after the deposition of each drop. For each image the static water contact angle was obtained by curve fitting based on the Young – Laplace equation with the reported contact angle being the average of ten measurements.

3.2.3.1 Water Contact Angle (WCA) Measurement

The polystyrene (PS) samples used were rectangular 6 cm x 1.2 cm (for side-on treatment) and 1 cm x 1.2 cm (for head-on treatment) with thickness of 1.2 mm, (Goodfellow Cambridge Ltd.). Each PS sample was prepared by cleaning in an ultrasonic bath containing isopropanol for 180 seconds, then rinsed with fresh isopropanol and dried out in a pure nitrogen gas stream. The clean samples were then introduced head-on and side-on to the plasma plume for different times ranging from 20 s to 3 minutes.

3.2.4 Optical Profiling System

The WYKO NT1100 Optical Profiling system was used to provide accurate and non-contact surface topography information with a sub-nanometer vertical resolution at 50x magnification.

This device utilizes white light interferometry for high resolution (< 1Å Ra) surface measurements, from sub-nanometer roughness to millimetre-high steps. A vertical measurement range (0.1 – 1 nm), vertical scan speed (up to 7.2 μm/sec) and a measurement array (736 x 480) image setting were selected for the results presented here. The roughness of the PS surface was converted to Ra (roughness average) value by the device software and collected from the computer system.

3.3 Plasma Characterisation Methods

3.3.1 Optical Emission Spectroscopy (OES)

In the OES technique, electrons in the sample emit light which is converted into spectral patterns or a spectrum. The emission spectrum of a chemical element or compound is the spectrum of frequencies of electromagnetic radiation emitted by the element's atoms or the compound's molecules when returned to a lower energy state [25]. Quantitative and qualitative analysis of the material composition are obtained by the measurement of the intensity of the peaks in the spectrum, since it is different for each element in the periodic table. The quantity plotted energy units, is the wavelength times the energy per unit wavelength and thus accurately represents the amount of energy at any wavelength. The OES device used to obtain the emission spectrum is the DH-2000 Spectrometer (Ocean Optics, Inc. USA) combined with Deuterium Tungsten Halogen Light Sources and a DH- 2000 fiber optic cable. It combines the continuous spectrum of deuterium and tungsten halogen light sources in a single optical path. The combined-spectrum light source produces a powerful and stable output from 215 to 2000 nm.

3.3.2. Schlieren Imaging

Schlieren imaging with a field view of 20 cm has been used to observe the patterns of perturbation in the neutral gas density (change in refractive index) due to the interaction of the helium gas with ambient air as it exits the capillary and their interaction with the substrate. This was carried out with a z-configuration system [26] similar to that already used on the microjet system [27] utilising two parabolic mirrors, a light source (continuous xenon arc lamp) and a Photron Fastcam APX RS model high-speed video camera running Photron PFV (Photron Fastcam Viewer) software with a 1 ms shutter speed.

3.3.3 2D Optical ICCD Imaging

Fast imaging was done in order to study the temporal and spatial evolution of the microdischarge using an ICCD camera (Andor DH520). A delay generator (DG645 Stanford Research Systems) was used to generate a pulse width of 100 ns to trigger the ICCD camera. Time-resolved and time-averaged images were obtained over eight (8) ac cycles. A 50 ns exposure time was used for imaging of the microchannel and the plasma bullet evolution. A time resolution of a few milliseconds was used for the observation of the general plasma plume structure.

References

1. R. Wiesendanger, Scanning Probe Microscopy and Spectroscopy, (Cambridge: Cambridge University Press, 1994).

2. Gerd Binnig and Heinrich Rohrer received the Nobel prize for Physics in 1986 for their invention of the scanning tunneling microscope. See also: (a) Binnig G.; Rohrer, H. *Helvetica Physica Acta* **1982,** *55,* 726; (b) Binnig, G.; Rohrer, H.; Gerber, Ch.; Weibel, E.**1982,** *Phys. Rev. Lett.* **1982,** *49,* 57.

3. Miles, M. J. in *Characterization of Solid Polymers; New Techniques and Developments* Spells, S. J. (Ed.), Chapman & Hall, London, UK, 1994.

4. R. D. Piner, J. Zhu, F. Xu, S. Hong, and C.A. Mirkin, Science 283, 661 (1999).

5. Y. Xia and G.M. Whitesides, Langmuir 13, 2059 (1997)

6. Schönherr, H. *Ph.D. Thesis* University of Twente, Enschede, The Netherlands, 1999, ISBN 90 365 1347 2.

7. Baty, A. M.; Leavitt, P. K.; Siedlecki, C. A.; Tyler, B. J.; Suci, P. A.; Marchant, R. E.; Geesey, G. G. *Langmuir* **1997,** *13,* 5702.

8. Ortega-Vinuesa, J. L.; Tengvall, P.; Lundström, I. *Thin Solid Films* **1998,** *324,* 257

9. Ortega-Vinuesa, J. L.; Tengvall, P.; Lundström, I. *J. Colloid Interface Sci.* **1998,** *207,* 228;

10. Lin, J. N.; Drake, B.; Lea, A. S.; Hansma, P. K. *Langmuir* **1990,** *6,* 509.

11. Baty, A. M.; Leavitt, P. K.; Siedlecki, C. A.; Tyler, B. J.; Suci, P. A.; Marchant, R. E.; Geesey, G. G. *Langmuir* **1997,** *13,* 5702.

12. Shibata-Seki, T.; Masai, J.; Ogawa, Y.; Sato, K.; Yanagawa, H. Appl. Phys. A **1998,** 66,625.

13. Chan, C.-M. Polymer surface modification and characterization, Hanser/Gardner Publications, Inc., Cincinnatti, OH, 1994

14. XPS was developed by Professor Kai Siegbahn and his collaborators at the University of Uppsala. For his discovery he received the Nobel prize in 1981. See also: a) Siegbahn, K.; Nordling, C.; Fahlman, R.; Hamrin, K.; Hedman, J.; Johansson, T.; Bergmark, T.; Karlsson, S.-E.; Lindgren, I.; Lindberg, B. *ESCA: Atomic, Molecular, and Solid State Structure Studied by Means of Electron Spectroscopy,* Nova Acta Regiae Sco. Sci.Upsaliensis, Ser. IV, Vol. 20, Almqvist and Wiksells, Stockholm, 1967; (b) Siegbahn, K.; Nordling, C.; Johansson, G.; Hedman, J.; Heden, P. F.; Hamrin, J.; Gelius, U.; Bergmark, T.; Werme, L. O.; Manne, R.; Baer, Y. *ESCA Applied to Free Molecules,* North-Holland,Amsterdam, 1969.

15. P. Weightman, Phys. Scr. 1992, T41, 27

16. S. Diplas, G. Shao, S.A. Morton, P. Tsakiropoulos, J.F. Watts, Intermetallics 7 (1999) 937.

17. S. Diplas, J.F. Watts, S.A. Morton, G. Beamson, P. Tsakiropoulos, D.T. Clark, J.E. Castle, J. Electron Spectrosc. Relat. Phenom. 113 (2001)153.

18. S. Diplas, J.F. Watts, P. Tsakiropoulos, G. Shao, G. Beamson, J.A.D. Matthew, Surf. Interface Anal. 31 (2001) 734.

19. K. Kobayashi, Nucl. Instrum. Meth. Phys. Res. A 547 (2005) 98.

20. Anand, M.; Cohen, R. E.; Baddour, R. F. *Polymer* **1981,** *22,* 361.

21. (a) d'Agostino, R. *Plasma Deposition, Treatment and Etching of Polymer Films,* Acadamic Press, Inc.: San Diego, CA, 1990; (b) Zisman, W. A. *Contact Angle-Wettability& Adhesion,* Gould, R. F. (Ed.); Am. Chem. Soc., Washington, D.C.,1964.

22. (a) Ho, C.-P.; Yasuda, H. *J. Biomed. Mater. Res.* **1988,** *22,* 919; (b) Inagaki, N; Tasaka, S.; Kawai, H.; Kimura, Y. *J. Adhesion Sci. Technol.* **1990,** *4,* 99.

23. Gengenbach, T. R.; Vasic, Z. R.; Chatelier, R. C.; Griesser, H. J. *J. Polym. Sci.: Part A: Polym. Chem.* **1994,** *32,* 1399; (b) Gengenbach, T. R.; Griesser, H. J. *Surf. Interface Anal.***1998,** *26,* 498; (c) Gengenbach, T. R.; Chatelier, R. C.; Griesser, H. J. *Surf. Interface Anal.* **1996,** *24,* 271; (d) Gengenbach, T. R.; Chatelier, R. C.; Griesser, H. J. *Surf. Interface Anal.* **1996,** *24,* 611; (e) Gengenbach, T. R.; Griesser, H. J. *J. Polym. Sci.: Part A: Polym. Chem.* **1999,** *37,* 2191; (f) Gengenbach, T. R.; Griesser, H. J. *J. Polym. Sci.Part A: Polym. Chem.* **1998,** *36,* 985; (g) Gengenbach, T. R.; Griesser, H. *Polymer* **1999,** *40,* 5079; (h) Boenig, H. V. *Fundamentals of Plasma Chemistry and Technology,* Technomic Publishing Co., Inc.: Lancaster, PA, 1988; (i) Yasuda, H. K. *J. Macromol.Sci.-Chem.* **1976,** *A10,* 383.

24. a) Yasuda, H.; Sharma, A. K.; Yasuda, T. K. *J. Polym. Sci. Polym. Phys. Ed.* **1981,** *19,* 285; (b) Yasuda, T.; Okuno, A. K.; Yoshida, K.; Yasuda, H. *J. Polym. Sci. Polym. Phys. Ed.* **1988,** *26,* 1781; (c) Yasuda, T.; Yoshida, K.; Okuno, T.; Yasuda, H. *J. Polym. Sci. Polym. Phys. Ed.* **1988,** *26,* 2061; (d) Kennedy, V. O. *J. Coating Technol.* **1988,** *60,* 37, (e) Brennar, W. J.; Feast, W. J.; Munro, H. S.; Walker, S. A. *Polymer* **1991,** *32,* 1527 (f) van Damme, H. S.; Hogt, A. H.; Feijen, J. *J. Colloid Interface Sci.* **1986,** *114,* 167 (g) Owen, M. J.; Gentle, T. M.; Orbeck, T.; Williams, D. E. in *Polymer Surface Dynamics,* Andrade, J. (Ed.), Plenum Press, New York, 1988.

25. Allen, C.W. Astrophysical Quantities, 3rd edition, 1973, p. 109, 172.

26. Merzkirch ,Flow Visualization (New York: Academic) 1987,Chapter 3

27. J.-S. Oh, O. T. Olabanji, C. Hale, R. Mariani, K. Kontis, J. W. Bradley, J. Phys. D, Appl. Phys. 2011,15, 155206

CHAPTER FOUR

4.0 The Electrical Characterisation of DBDs inside a Microfluidic chip

Abstract

Microfluidic devices were studied here to determine the potential for lab-on-a-chip applications based on the dielectric barrier discharge (DBD) mode of activation. This type of discharge is usually formed between two parallel electrodes, with a separation between 0.1 and 1 mm, where one or both electrodes are covered with a dielectric barrier. Different working conditions were considered: A sinusoidal voltage of up to 9 kV peak to peak with frequencies from 10 kHz to 40 kHz has been applied to the electrodes imbedded in PDMS layers. The micro channel width was maintained at 50 and 100 μm, and the pressure was varied between 35 kPa and 103 kPa above atmospheric pressure, using helium, neon and nitrogen gases respectively, for the formation of the microplasma discharges. This generated micro discharge currents in the range of 0.1 to 12 mA at a flow rate of 0.012 l min^{-1}, and can be seen as current filaments of about 100 ns duration on the time resolved electrical waveform. Current–Voltage (I–V) measurement results obtained show a sharp peak in the discharge current at the breakdown voltage. Results also confirm the dependence of discharge current on frequency, gas composition, microchip geometry and flow rate.

4.1 Introduction

The concept of micro-total analysis system (μTAS) or "lab-on-a-chip" devices has gained a remarkable amount of popularity in various science and engineering fields over the past decade. Most of these interests arise from the possibility of incorporating sample-processing steps such as sample pretreatment, dilution, calibration, separation and detection onto a small dimensioned "chip" of the order of a few tens of microns up to a few centimeters [1 - 4]. Critical to the successful implementation of μTAS technologies are the availability of a simplistic device prototyping and preparation methods, the physical and chemical characterization of the substrate material, and the development of integrated "on-chip" analyte detection methods [5, 6].

Microfluidics has brought many advantages for analytical chemistry applications by the miniaturization of analytical devices. Silicon was the first material used as it is well known in the semiconductor industry and because its properties and processing are well established. Another often used material in microanalysis systems is glass due to its broad study in analytical chemistry and because of its chemical and thermal stability. Although glass has other favorable properties, its micro processing is somewhat challenging, therefore making its use somewhat impractical.

Polymers tend to be more attractive due to their low cost and easy processability [7] and [8], although the drawback is typically their poor thermal and chemical stability. Examples such as polydimethylsiloxane (PDMS) and polystyrene have led to the development of a broad range of techniques, which provide high throughput and high-resolution patterning. PDMS was used here as the preferred dielectric option because it is inert, non-toxic, non-flammable and optically clear, based on the dielectric barrier discharge (DBD) mode of activation.

4.2 Dielectric Barrier Discharges (DBDs)

A Dielectric Barrier Discharge (DBD), known as silent discharge is usually formed between two parallel electrodes with a separation in the order of 0.1 to 10mm, where one or both electrodes are covered with a dielectric barrier. They are normally operated with square wave currents, sinusoidal wave currents or pulses waveforms with frequencies ranging from a few Hz to MHz, but often in the KHz range [9]. The amount of displacement current that can flow through the dielectric is determined by the dielectric constant and thickness. At atmospheric pressure, gas breakdown in the plane gap of the DBD usually occurs in a large number of tiny individual microdischarges and this occurs when the applied voltage exceeds breakdown voltage.

DBDs are strongly non-equilibrium plasmas and are often operated at atmospheric pressure. They have unique properties and characteristics which form the basis for many applications such as ozone generation, plasma display panels, surface engineering processes, gas treatment and excimer lamps [9, 10]. Examples of the DBD characteristics are described in [9 – 12], and demonstrated with low electric power (< 1W), low gas temperature (~ 600 ° K) plasma sources, and excellent dissociation capability for molecular species. These characteristics have been explored at reduced pressures (10-100mbar) in plasma modulation diode laser atomic absorption spectrometry of excited states of chlorine and fluorine, with typically helium or argon as the plasma gases.

Here we investigate the behaviour of the discharge and displacement currents as a function of frequency, gas composition, microfluidic device geometry and flow rate. We find that the breakdown voltage varies slightly with frequency, but changes considerably with gas composition and electrode separation.

4.3 Experimental Setup

The experimental arrangement used in this work is shown in figure 4.1. I (t) and V (t) represent the current and the voltage probes respectively in the schematic.

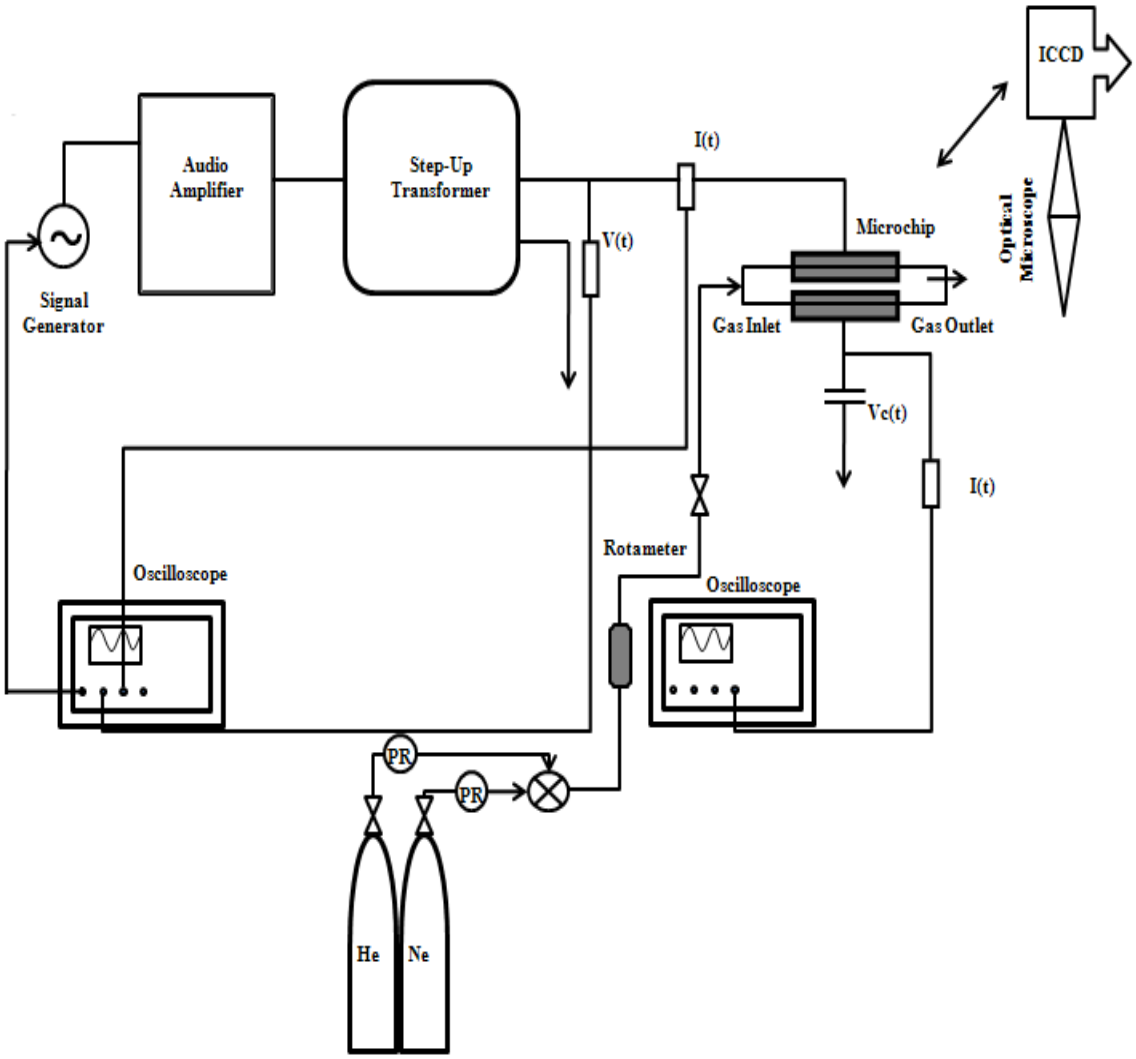

Figure 4.1: A schematic of the experimental setup

The microchip used (shown in figure 4.2) consists of two platinum electrodes of 50 μm thickness and dimensions of 11.3 mm x 14.2 mm that are sandwiched between two parallel polymer (PDMS) layers of about 40mm to 50 mm in length. Figure 4.2 (b) shows the details of

the features in between the two PDMS layers. The thickness of the PDMS dielectric layer varies between 2 mm and 3mm in each case. The thickness of the dielectric barrier between the electrodes and the microchannel is approximately 50 µm. The PDMS microchip presents a quick, simple and reliable method for localised plasma treatment within microchannels.

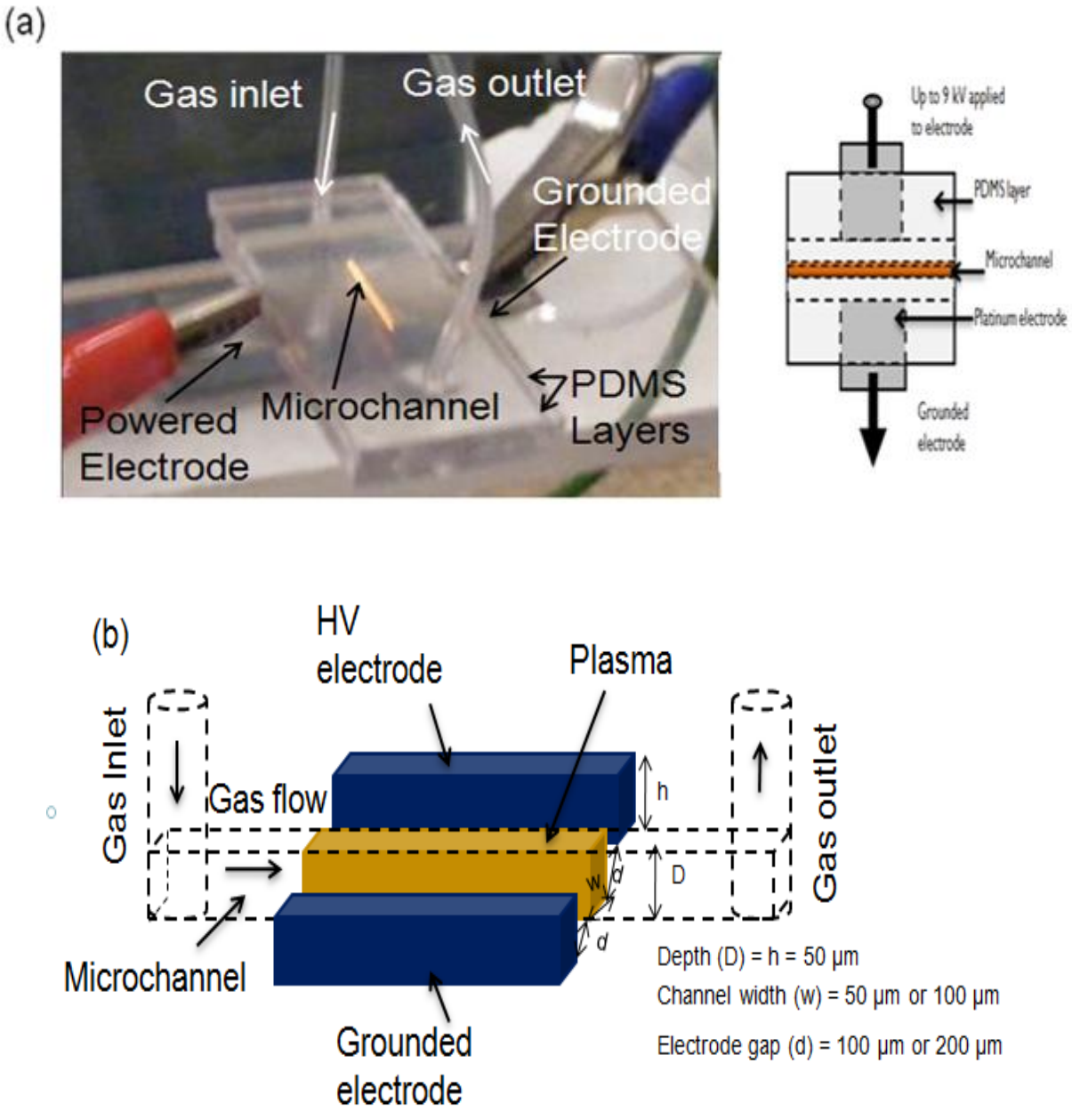

Figure 4.2: (a) The PDMS microchip features (b) Closed features in between the two PDMS layers

We can see from figures 4.2(a) and (b) that the plasma is closed and also confined within the microchannel. Platinum electrodes were used because of their high resistance to corrosion and oxidation. The electrode separations used are 250 μm, 300 μm and 450 μm respectively. The microchannels are 30mm in length, 50 μm in depth and are 50μm and 100 μm wide. Neon and helium gases were used to obtain the results presented here, although nitrogen gas was also used. Pure samples of each gas was made to flow through a PTFE pipe of inner diameter (ID = 0.5mm) and outer diameter (OD = 1.6mm) into the microchannel by the use of a needle gauge and a small transparent tube of (OD = 1.7mm) and (ID = 1.2mm). The flow rate, *f* through the microchannel was varied by adjusting the rotameter/flow meter connected at one end to the gas cylinder and the inlet tube at the other end. A sinusoidal high voltage of up to 9 kV (peak to peak) is applied at frequencies of 10 kHz, 20 kHz and 30 kHz to one of the platinum electrodes, and the other is grounded.

The electrical characterization is based on the work reported by others [13 - 15]. The applied voltage V_{app} (t) was measured with the aid of a 15 kV, 50MHz High voltage probe. The discharge current I_d (t) was determined from the voltage drop V_R(t) across the shunt resistor R = 50 **Ω**, connected in series with the grounded electrode. The equivalent circuit of the present DBD system is illustrated [16]. The charge q (t) transferred across the electrode gap was calculated from the measurement of the voltage drop V_T (t) across the shunt capacitor (100pF), using the expression V_T (t) = Q (t)/C. A streamer -like discharge is revealed by the multi-peak character or hairs of the discharge current.

4.4 Results and Discussions

Typical current I (t) and voltage V (t) electrical waveforms were observed using flowing neon and helium gases at atmospheric pressure, at operating frequencies of 10, 20 and 30 kHz and a flow rate of 0.012 litre min^{-1} . Different electrode gaps or separations were also considered. We find that the current I (t) waveform leads the voltage V (t) waveform by approximately 86º. The current waveform can also be seen with multiple spikes/hairs (shown in green colour in Figure 4.3 (a),(b),(c) and (d)) and these first appear at breakdown voltage and then increases as V_{app} (t) = V (t) is increased from 3 kV to 6 kVp-p. The traces shown in purple colour in figure 4.3 represent the applied voltage from 3kV p-p to 6 kVp-p in steps of 1kV p-p. The scales on the vertical axis are 1kV/div for the voltage traces and 1 mA/div for the current traces. We found that in helium, the breakdown voltage was approximately 6kV across the three different operating frequencies for a 450 μm electrode gap in comparison to just 5 kV p-p for a 250μm gap. This is due to the fact that the capacitance decreases as the gap increases, hence breakdown voltage increases.

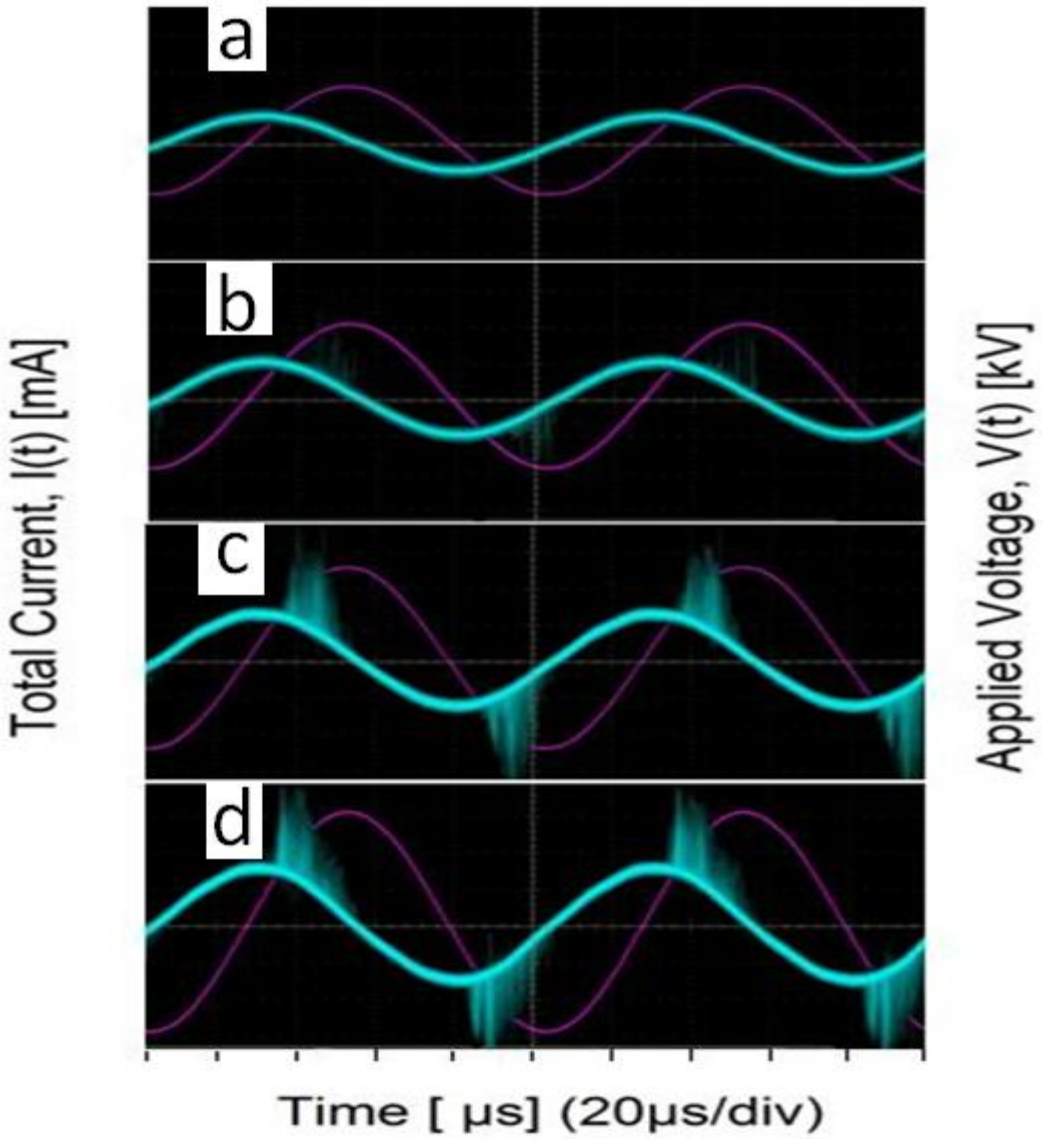

Figure 4.3: Images of the electrical waveform characteristics of a DBD in Neon at a flow rate of 0.012slm. Current traces are shown in green and voltage traces in purple (a) just before breakdown (b) at the start of breakdown (c) after breakdown (d) at higher voltages beyond breakdown

The measured waveform of the total current I (t) consists of two parts, the first part is the displacement current I_D (t) and this corresponds to the amplitude of the current waveform. The second part is the discharge current I_d (t) which corresponds to the multiple spikes or

hairs observed on the current waveform. The discharge current characteristics are in good agreement with published results [17] and are seen as current spikes or hairs or short pulse widths of about 10 – 100 ns, superimposed on the main current curve. We obtained the discharge current by subtracting the traces of the displacement current from the total current and compared it with the measured voltage drop across a shunt resistor R = 50 Ω connected in series with an unbiased electrode and ground using a current probe. This is done by simply replacing the shunt capacitor in figure 4.1 by a 50 Ω resistor. The results appear to be in good agreement.

The measurement results obtained are shown in figure 4.4. Here, neon gas is seen to breakdown at a lower voltage than helium gas due to the higher ionization potential of helium. These breakdown voltages vary slightly with frequency when increased from 10 kHz to 30 kHz. We also see a sharp peak in discharge current at the breakdown voltage as well as variations in breakdown voltage due to changes in gas composition, operating frequency and electrode separation. We have confirmed this filamentary behaviour using optical emission imaging (shown in figures 4.5, 4.6, 4.7 and 4.8) that revealed a non-uniform radial distribution of the microdischarge region.

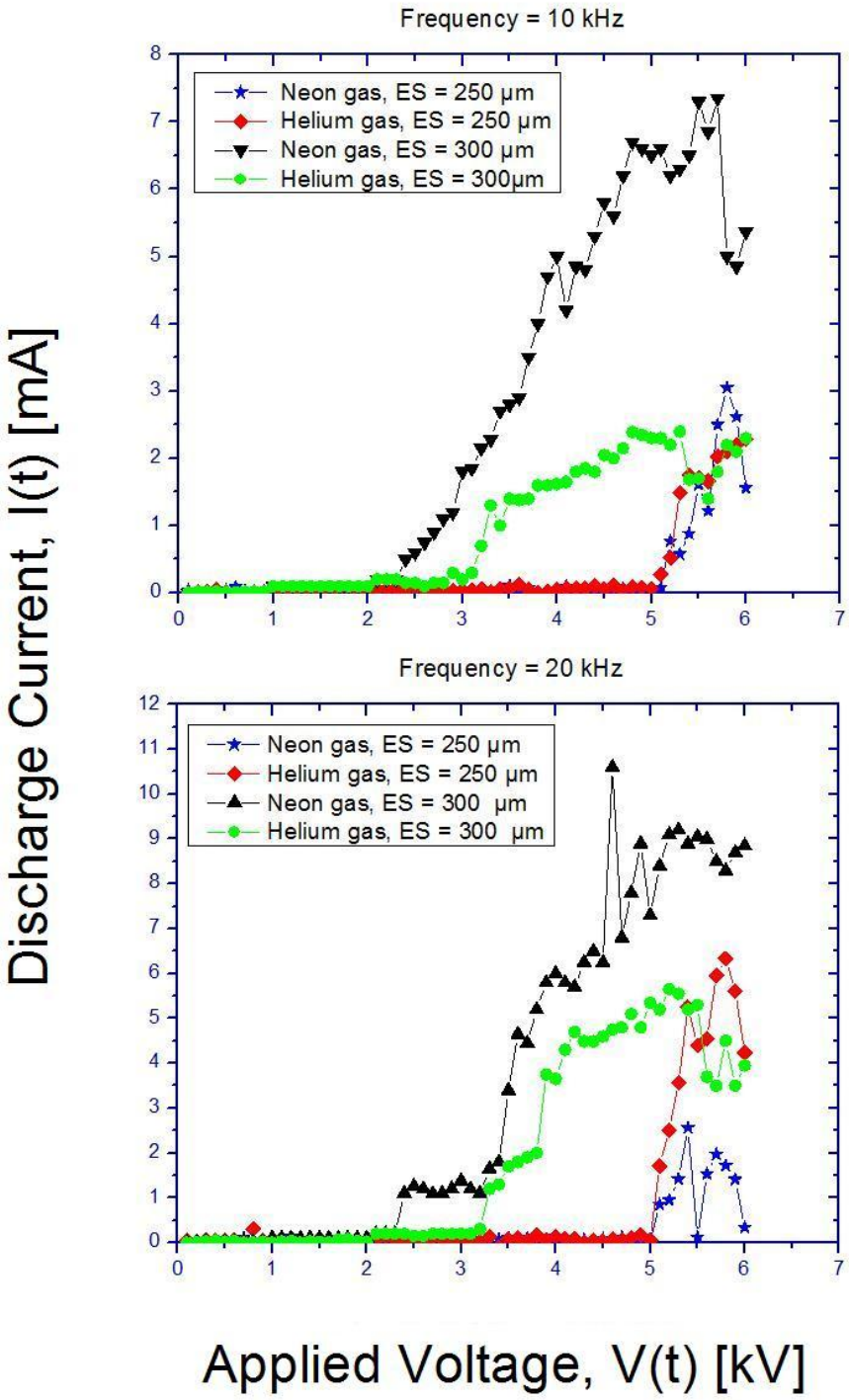

Figure 4.4: The dependence of discharge current on breakdown voltage, frequency and electrode gap. (a) Frequency of 10 kHz (b) at a frequency of 20 kHz

The discharge current increases with decreasing impedance as a result of a frequency increase from 10 kHz to 20 kHz. The phase relationship from the lissajous figures obtained (shown in figure 4.9) also agrees with the results reported by others [18]. The lissajous figures are typically plots of the charge q (t) as a function of the applied voltage V_{app} (t) through one period of the applied voltage. The power dissipated in the discharge was estimated to be around 12 milliwatts and this was observed to decrease with increasing frequency and increase with increasing applied voltage. It is however necessary to further investigate the somewhat elliptical lissajous figures of the filamentary discharge obtained as this is somewhat different from the typical parallelogram expected. Results will help to accurately determine the equivalent.

4.4.1 2-D Optical Imaging

Time averaged and time-resolved images have been used to investigate the behaviour of the microdischarge (in helium for 250 μm gap) within the microchannel using 2D optical ICCD imaging with 50 ns time resolution. The optimum configuration that gives the most stable and intense microdischarge was obtained by varying the applied voltage and the frequency (shown in figure 4.5). Figure 4.6 was obtained by spatially resolving images in figure 4.5. This figure shows in more detail the electric field intensities at different regions within the microchannel. The results show that the microdischarge ignites at preferential regions (at the electrode edges) corresponding to regions of high electric field strengths before expanding along the entire length of the microchannel. The images also show a non-uniform microdischarge at the edges of the microchannel. This is an important factor to consider during surface modification

applications. This is further revealed by time-resolved imaging used to investigate the evolution of the discharge in more detail and shown in figures 4.7 and 4.8.

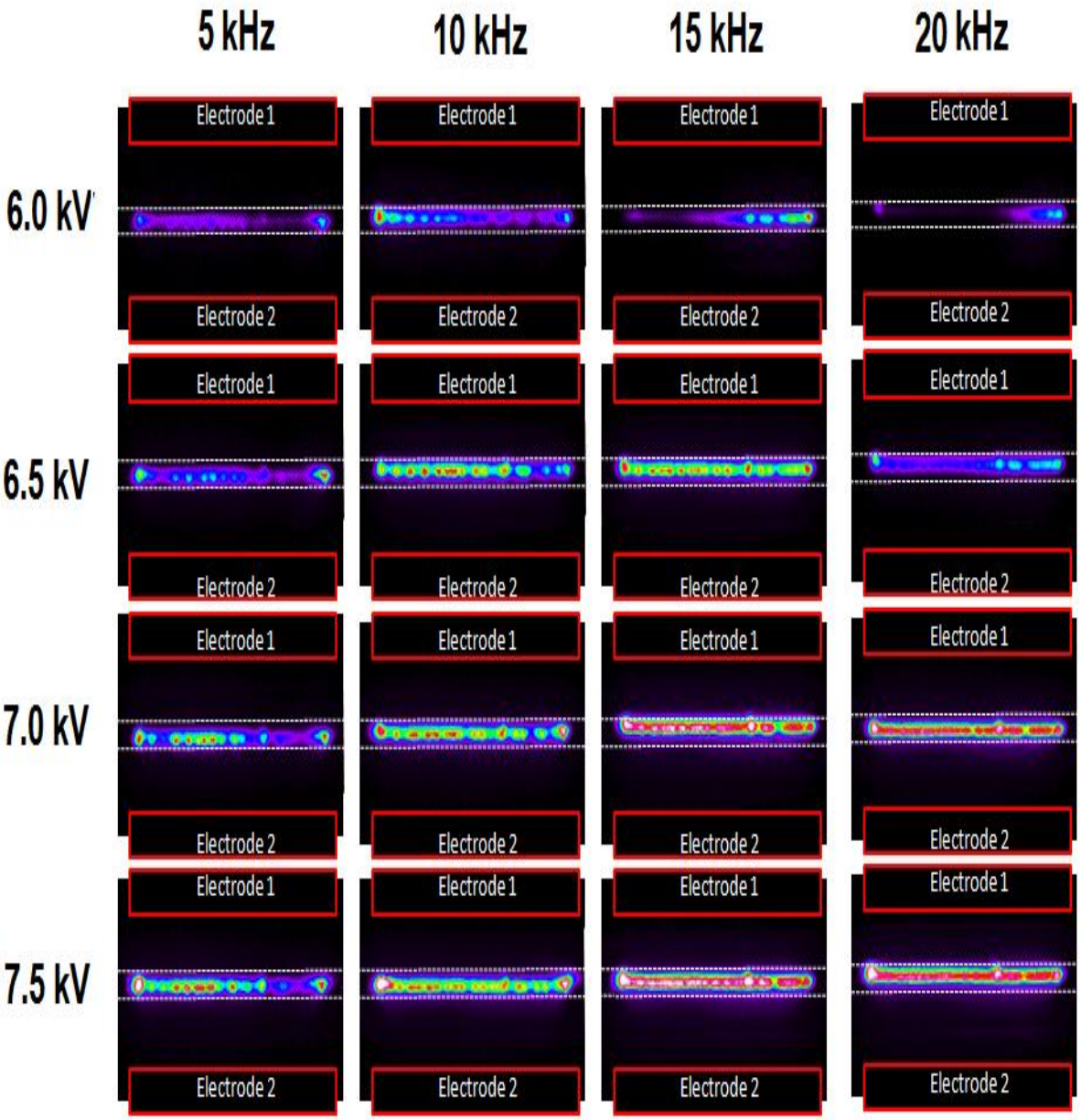

Figure 4.5: Time averaged ICCD image results showing microdischarge emission patterns within the entire microchannel of the microfluidic chip when applied voltage and frequency are varied. 50 ns exposure time. **The yellow bars represent the microchannel (100 μm) boundaries.**

Images in figure 4.7 were acquired during the positive half-cycle at time t = 76.3 to 80.1μs and those in figure 4.8 during the negative half-cycle at time t = 100.3 to 104.1μs. The images show different stages of the discharge evolution along both the x and y axes at a position corresponding to the centre of the microchannel when the applied voltage was V = 7 kV_{p-p} at a frequency f = 20 kHz. The images were acquired with a 50 ns exposure time and at 200 ns intervals. The red-dash bars show the microchannel edges when the upper electrode is the driven electrode and the lower electrode is the grounded electrode.

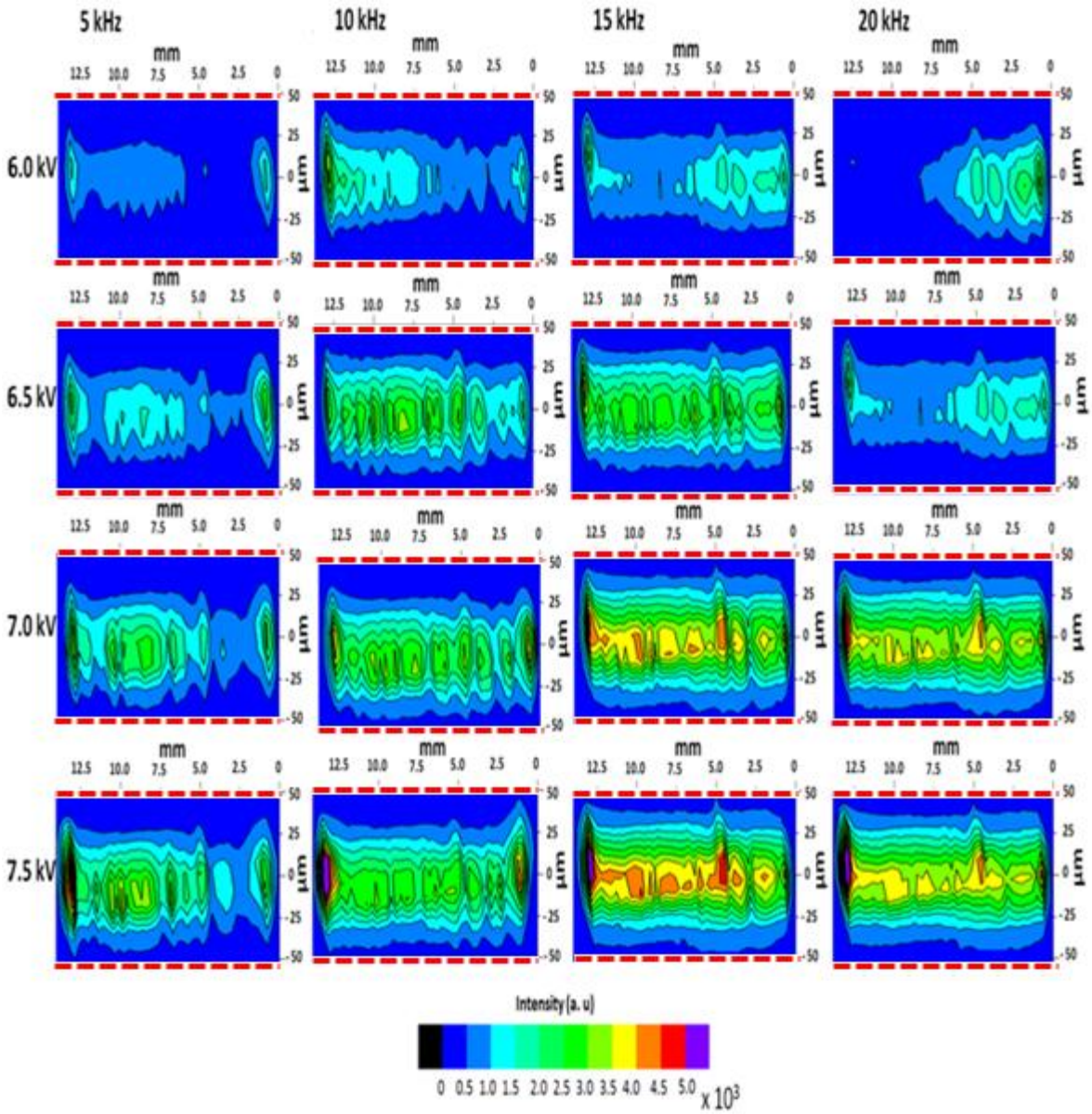

Figure 4.6: Spatially resolved time averaged ICCD image results showing microdischarge emission patterns within the microchannel of a microfluidic chip when applied voltage and frequency are varied. 50 ns exposure time. **The red-dash bars at the top and bottom of each image represent the microchannel (100 μm) boundaries.**

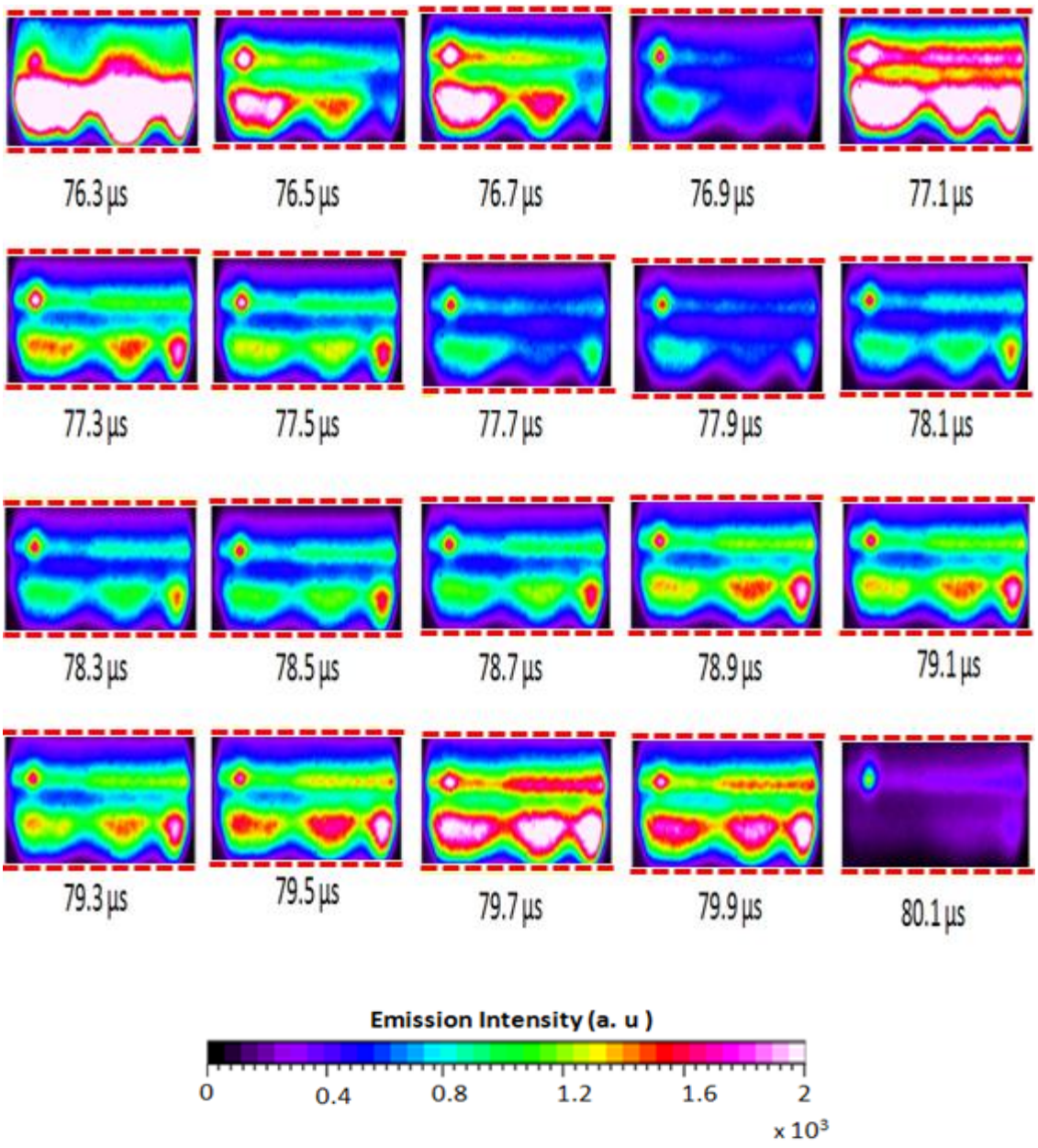

Figure 4.7: Time resolved ICCD images reflecting various phases of the microdischarges occurring in helium (V= 5 kV $_{p-p}$ and f = 20 kHz). Images taken with an ICCD gate of 50ns covering events occurring during the positive ac half-period. At time t = 76.3 µs to t = 80.1 µs. The microdischarge is filamentary. **The red-dash bars at the top and bottom of each image represent the microchannel (100 µm) boundaries.**

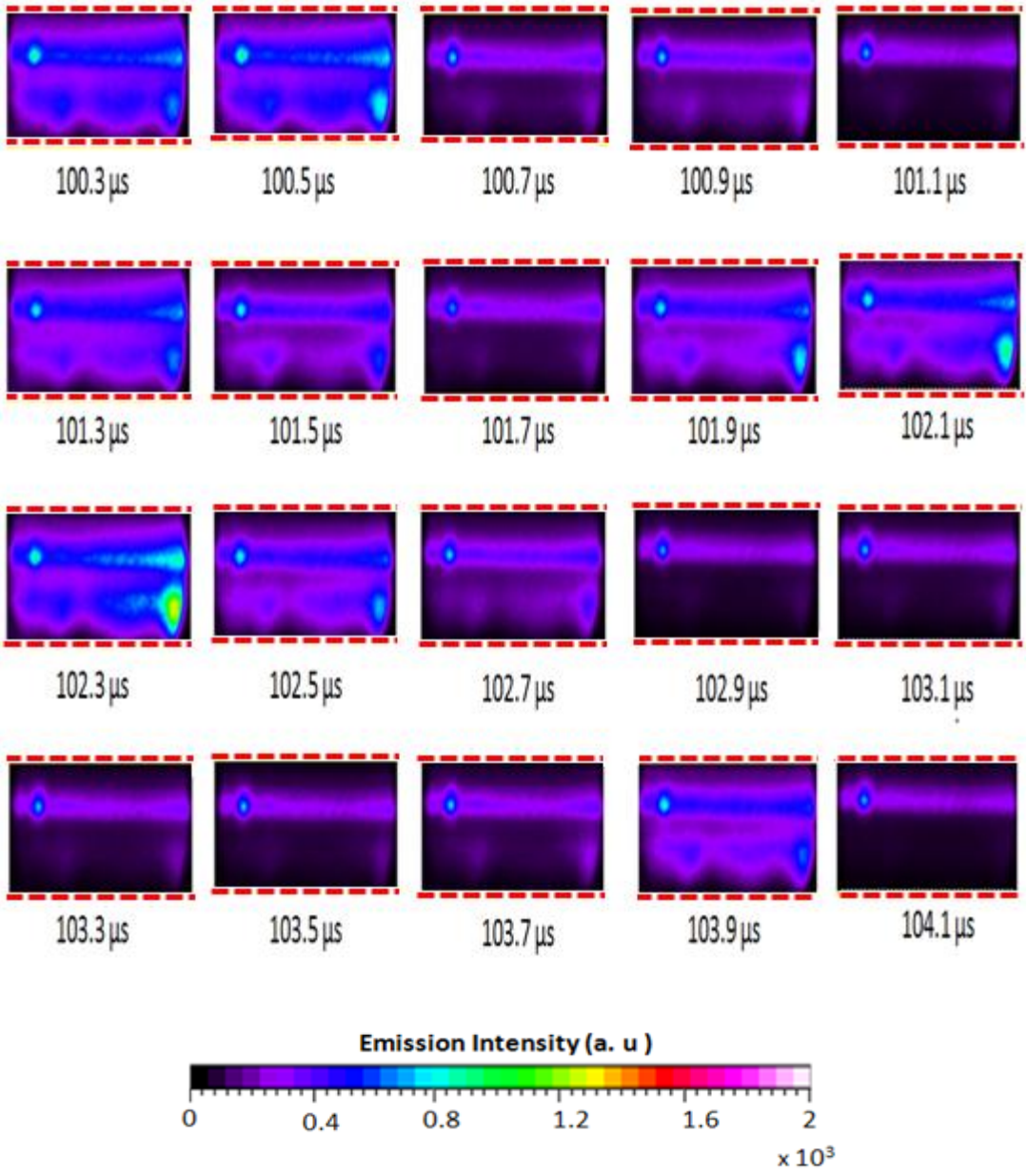

Figure 4.8: Time resolved ICCD images reflecting various phases of the microdischarges occurring in helium (V= 5 kV $_{p-p}$ and f = 20 kHz). Images taken with an ICCD gate of 50ns covering events occurring during the negative ac half-period. At time t = 100.3 µs to t = 104.1 µs. The microdischarge is filamentary. **The red-dash bars at the top and bottom of each image represent the microchannel (100 µm) boundaries.**

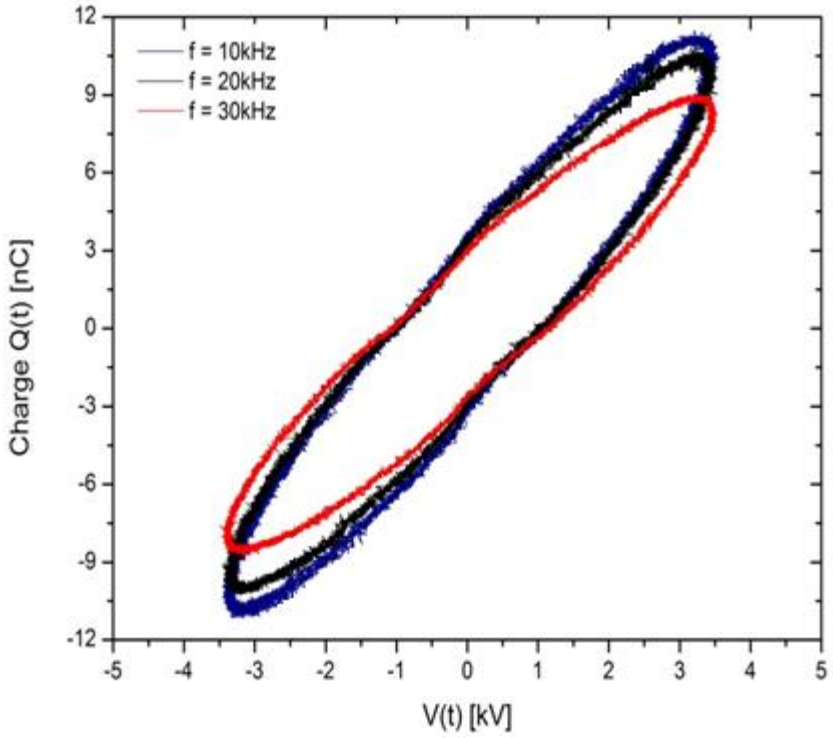

Figure 4.9: Showing variation in phases of Lissajous (Charge-voltage) plot with frequency.

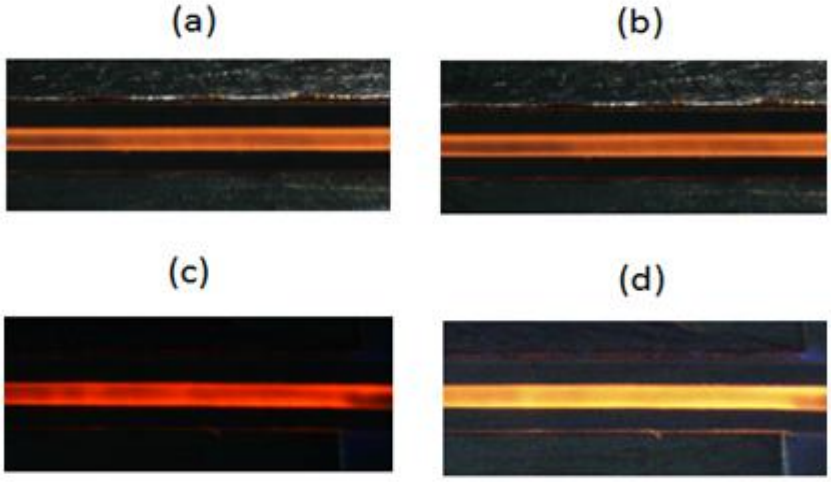

Figures 4.10: Showing variation in microdischarges within the microchannel due to changes in flow rate **(a)** 10 sccm **(b)** 12 sccm **(c)** 14 sccm and **(d)** 16 sccm. Image magnification (x 50).

Typical images of microdischarges observed (in neon gas for 250 μm gap) are shown in figure 4.10. The initially hollow microdischarge observed at a lower flow rate of 10 sccm becomes more and more uniform as the flow rate is increased up to 16 sccm. Hence, the generation of a homogeneous discharge also depends on the flow rate.

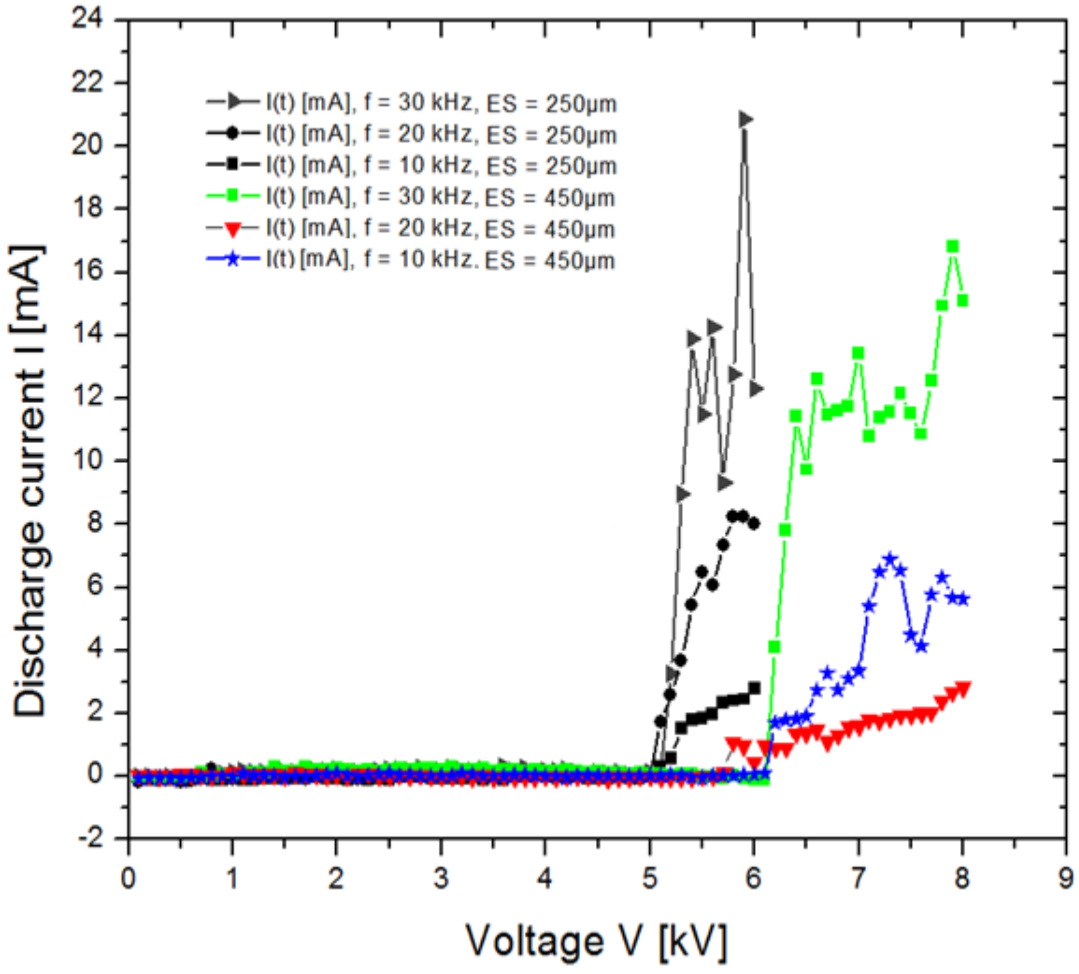

Figures 4.11: The dependence of discharge current on breakdown voltage, frequency and electrode gap. A variation of the electrode gap for instance for helium gas from 250 μm to 450 μm increases the breakdown voltage from about 5.3 kVp-p to 6.3 kV p-p.

4.5 Conclusions

A DBD operating with flowing helium and neon gases in electrode gaps of 250 μm, 300 μm and 450 μm has been studied. Preliminary results confirm that discharge current (0.1 to 12 mA) increases with increasing microchannel width from 50 μm to 100 μm (shown in figure 4.4) when the other parameters are kept constant. The breakdown voltage for pure samples of both gases also dropped significantly with an increase in microchannel width (see figure 4.4). This is however different when the microchannel width is kept constant at 50 μm and the electrode gap varied. A variation of the electrode gap for instance for helium gas from 250 μm to 450 μm increases the breakdown voltage from about 5.3 kVp-p to 6.3 kV p-p (shown in figure 4.11).

From the 2-D optical images and current waveform obtained, we find that the discharges are filamentary and comprise numerous current pulses of short widths (10-100 ns) per half cycle and this is totally different from the behaviour in homogeneous DBD called atmospheric pressure glow discharge (APGD) obtained in previous studies. We find that these numerous current hairs first appear at breakdown voltage and that they appear to increase in number as the voltage is increased further. Our results in figure 4.4 also show that breakdown voltage varies very slightly with frequency and it is maximum at 30 kHz (not shown here). Finally, we have also shown that the discharge current obtained varies depending on the gas composition, electrode gap and the applied frequency.

References

[1] Eijkel J C T, Stoeri H and Manz A 1999 A molecular emission detector on a chip employing a direct current microplasma *Anal. Chem.* **71** 2600–6

[2] Eijkel J C T, Stoeri H and Manz A 2000 A dc microplasma on a chip employed as an optical emission detector for gas chromatography *Anal. Chem.* **72** 2547–52

[3] Von Engel A 1965 *Ionized Gases* (Oxford: Oxford University Press)

[4] Eijkel J C T, Stoeri H and Manz A 2000 An atmospheric pressure dc glow discharge on a microchip and its application as a molecular emission detector *J. Anal. At. Spectrom.* **15** 297–300.

[5] Pearse R W B and Gaydon A G 1950. The Identification of Molecular Spectra (London: Chapman and Hall)

[6] Cserfalvi T and Mezei P 1994 Direct solution analysis by glow-discharge ; electrolyte cathode discharge spectrometry *J. Anal. At. Spectrom.* **9** 345–9

[7] H. Becker, L.E. Loccascio, Polymer microfluidic devices,Talanta 56 (2002), pp 267–287.

[8] Eijkel J.C.T., Stori H., Manz A., A dc microplasma on a chip employed as an optical emission detector for gas chromatography, Anal. Chem. 72 (2000) 2547-2552.

[9] J.R. Roth, Industrial plasma engineering, Principles, vol. 1, IOP Publishing, Philadelphia, 1995.

[10] U. Kogelschatz, B. Eliasson, W. Egli, From ozone generators to flat television screens: history and future potential of dielectric-barrier discharges, Pure Appl. Chem. 71 (1999) 1819–1828.

[11] M. Miclea, K. Kunze, G. Musa, J. Franzke, K. Niemax, The dielectric barrier discharge — a powerful microchip plasma for diode laser spectrometry, Spectrochim. Acta Part B 56 (2001) 37–43.

[12] M. Miclea, K. Kunze, J. Franzke, K. Niemax, Plasmas for lab-on-the-chip applications, Spectrochim. Acta Part B 57 (2002) 1585–1592.

[13] Okazaki S, Kogoma M, Uehara M and Kimara Y 1993 *J. Phys.D: Appl. Phys.* **21** 889–92.

[14] Massines F, Rabehi A, Decomps Ph, Gadri R, S`egur P and Mayoux Ch 1998 *J. Appl. Phys.* **83** 2950-57.

[15] Tochikubo F, Chiba T and Watanabe T 1999 *Japan. J. Appl.Phys.* **38** 5244–50.

[16] G Nersisyan and W G Graham 2004 *Plasma Sources Sci. Technol.* **13** 582-587

[17] Flores-Fuentes, A et al (2009); Electrical Model of an Atmospheric Pressure Dielectric Barrier Discharge cell, Vol 37, 1

[18] R. Valdivia-Barrientos et al (2006); Analysis and electrical modeling of a cylindrical DBD configuration at different operating frequencies, Plasma Sources Science and Technology, Vol. 15, pp 237 – 245

CHAPTER FIVE

5.0 ICCD Imaging and Electrical Characterisation of "patterned" DBD

Abstract

We have used current-voltage (IV) and time-resolved 2-D optical imaging to investigate an atmospheric pressure dielectric barrier discharge (DBD) in a bonded microchannel using patterned electrodes. The microdischarge was produced using a sinusoidal voltage of up to 5 kV_{p-p} (peak-to-peak) at frequencies of 10, 20 and 30 kHz using flowing helium gas. The microchannel width and depth were fixed at 50 μm. The discharge operation is in filamentary mode. Results show that the microdischarges are initiated in preferential regions that correspond to high electric fields. The discharge expands along the microchannel and electrode gaps at speeds of 100 - 200 ms^{-1} respectively. We have obtained global current densities J (A/cm^2) of up to 8 A/cm^2 across the electrode gap when a maximum electrical power of P (Watts) of ~ 2 W was supplied.

5.1 INTRODUCTION

Dielectric barrier discharges within bonded microchannels utilize a variety of noble gases and can be operated at or near atmospheric pressure. Additional applications to that previously discussed include biological and biomedical applications such as; for coating open glass

microchannels for isoelectric focusing (IEF) based protein separation [1, 2], for introducing stable plasma-polymerized acrylic acid (pp.AAc) on PDMS microchannels [3], for plasma polymerisation of low fouling tetraethylene glycol dimethyl ether (plasma polymerised tetraglyme,pp.TG) onto glass microfluidic channels and PTFE surfaces [4] ,for other application in immobilization and grafting of polymers [5 - 8] and for generating patterns of SiO_2, amino and epoxy groups [9, 10]. Many experimental and theoretical investigations suggest that the electrical breakdown in DBDs can either be filamentary or diffuse [11 - 17]. Recently we have characterised two similar microplasma microfluidic (MMC) chips [18]. Here, in order to better understand the temporal and spatial emission behaviour of the microdischarges, we have used standard current-voltage measurements and time resolved measurements using a high speed ICCD camera with 50 ns exposure time

5.2 EXPERIMENTAL SETUP

The experimental arrangement used in this work is in [18] and shown in figure 5.1. The microfluidic chip consists of identically patterned electrodes sandwiched between two PDMS layers. The microdischarge was driven by a sinusoidal voltage with frequencies of 10, 20 and 30 kHz and peak-to-peak voltage amplitudes of up to 5 kV_{p-p}.

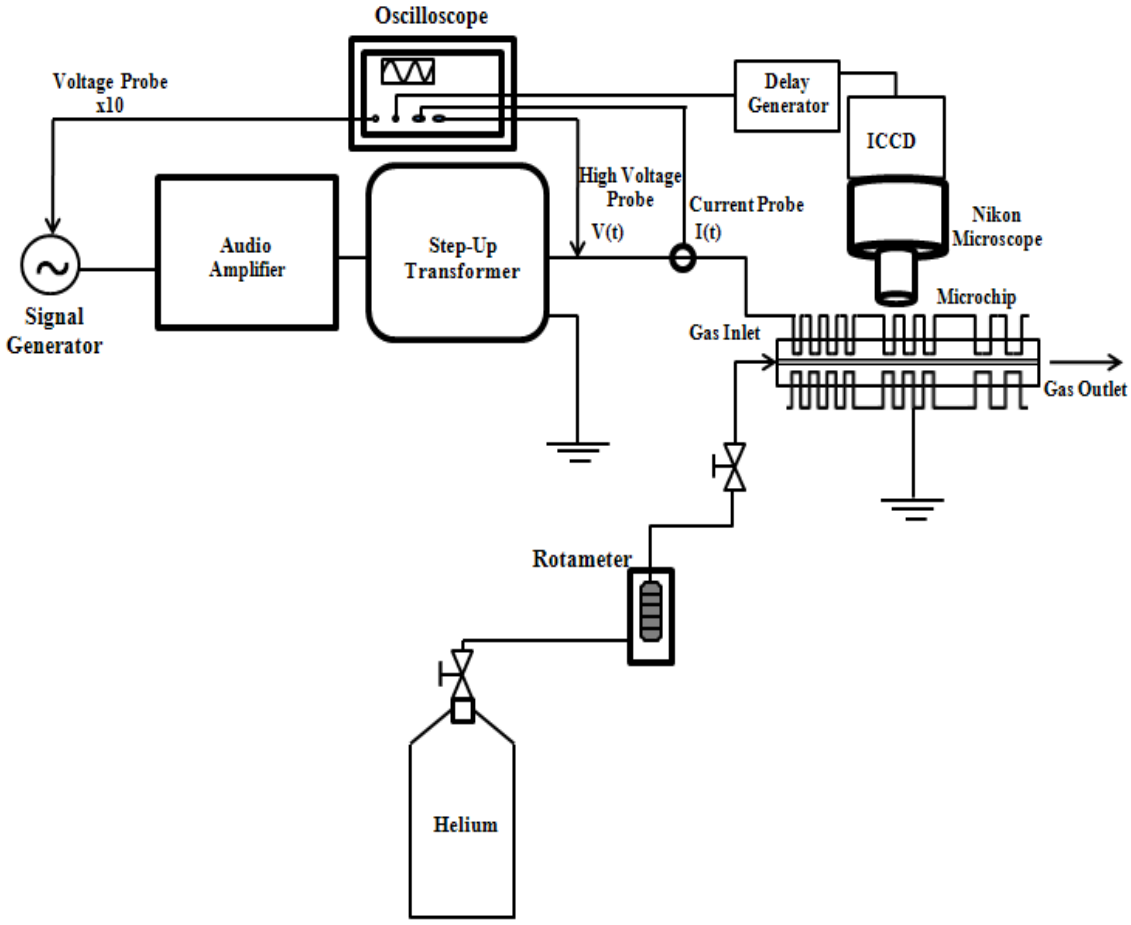

Figure 5.1. A schematic of the experimental setup showing the DBD configuration used.

Helium gas (99.996% purity) was used at a constant volumetric flowrate for all experiments. The gas flow was manually controlled by a rotameter (Omega FLT-39ST) connected to the Ethyl Vinyl Acetate (EVA) inlet tubing on the other end via a Polytetrafluoroethylene (PTFE) tube. Figure 5.2 shows a photograph of the microchip and a schematic of the electrode layout are shown in figure 5.3. The DBD is confined by PDMS between the two parallel arrays of electrodes separated at a distance of 150 μm. The electrode pattern allowed the investigation

of two regions of the microchannel of different electrode lengths *L* (a) L = 300 μm and (b) L = 500 μm. The channel width and height are fixed at 50 μm. The distance between the electrode array edge and the microchannel edge on each side was fixed at 50 μm in all regions.

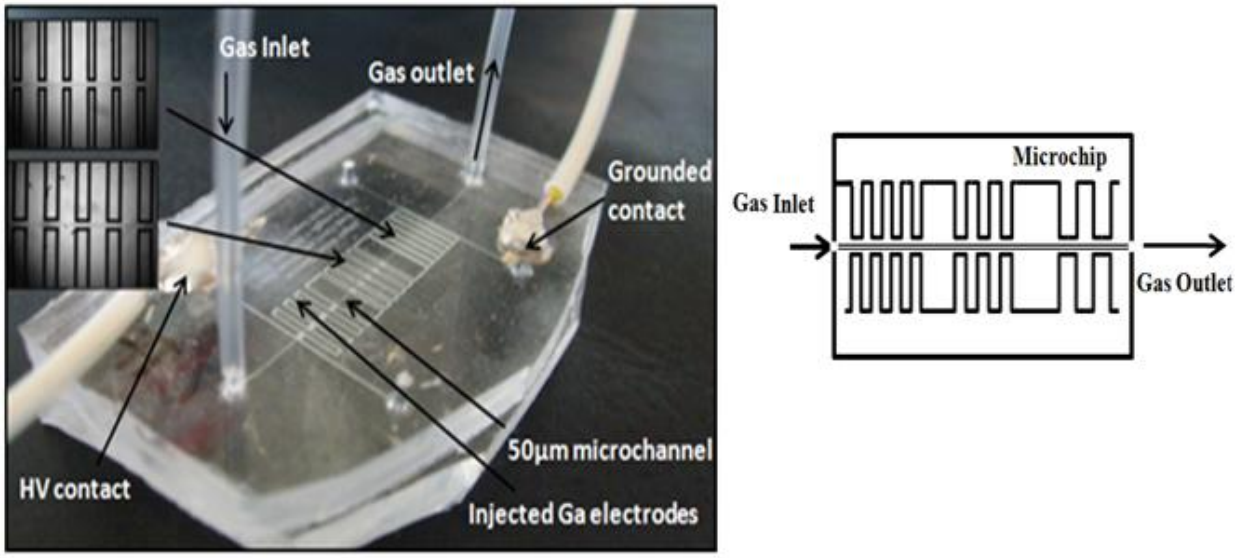

Figure 5.2. An image of a microfluidic chip containing injected gallium electrodes

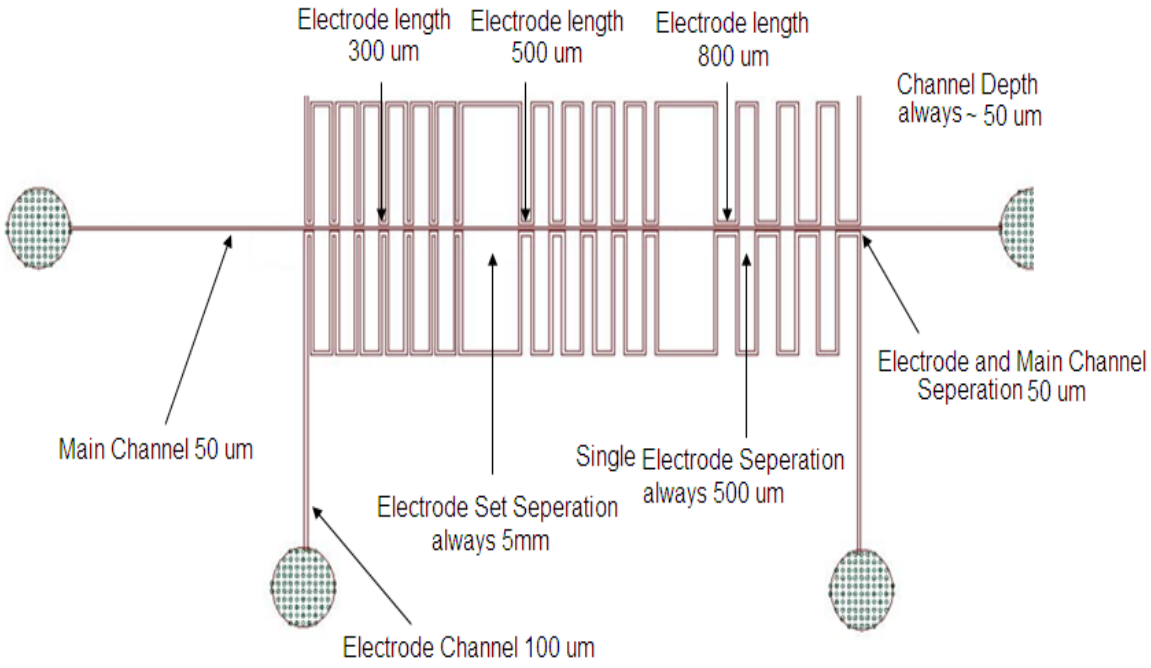

Figure 5.3. A schematic of microfluidic chip features showing electrode geometry and internal dimensions.

Time-resolved imaging was done in order to study the temporal and spatial evolution of the microdischarge using an ICCD camera (Andor DH520, 1024 x 256 pixels), attached to a Nikon microscope (magnification factor of x20) at a working distance of 3.8 mm. The temporal evolution and the spatial distribution of the microdischarge was obtained in the range of (0.1 -1) mm in the horizontal (x) direction i.e. along the microchannel, and in the range of (1 – 150) μm in the vertical (y) direction i.e. across the electrode gap. A delay generator (DG645 Stanford Research Systems) was used to generate a pulse of 100ns to trigger the ICCD camera. For these experiments, a fixed applied voltage of 4.3 kV_{p-p} and a frequency of 30 kHz were used. The time-resolved images were averaged over 8 ac cycles of the voltage or current waveform.

5.3 RESULTS and DISCUSSIONS

5.3.1 Electrical Characterisation

The microdischarge properties were determined from current-voltage measurements and optical 2D ICCD imaging. At atmospheric pressure, due to high collision rates, a growing electron avalanche can generate appreciable charge density at its tip after travelling a short distance. Since the microdischarge is confined within the microchannels, charge deposition on the dielectric surface becomes significant. Figures 5.4 and 5.5 show results obtained for filamentary discharge mode as a function of frequency and applied voltage. The discharge current was obtained from the measurement of the voltage drop across a 50 Ω shunt resistor connected in series with the grounded electrode in a method described in [18]. The first discharge mode obtained is known as the filamentary mode and this is shown in figure 5.4.

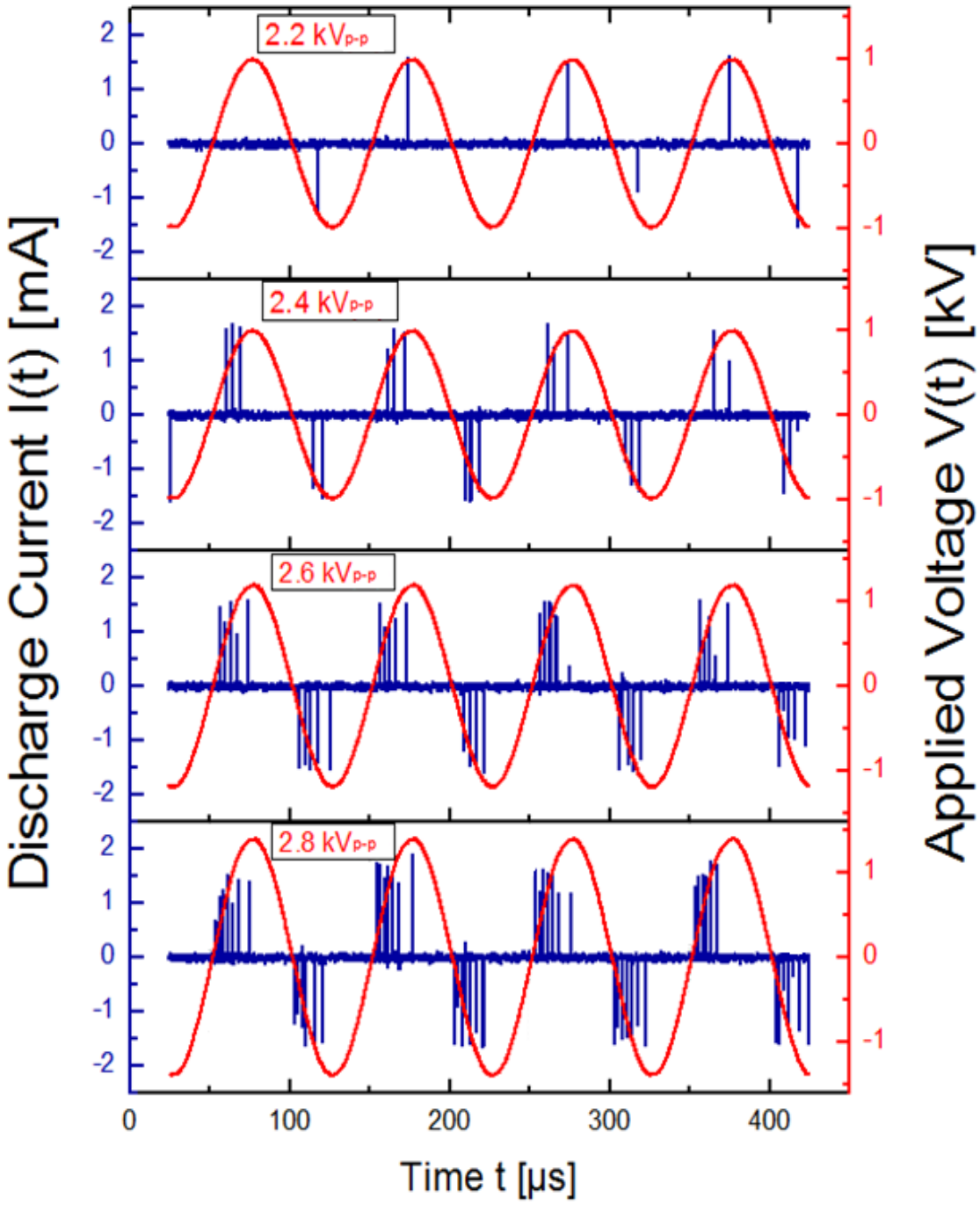

Figure 5.4. The discharge current waveform in filamentary mode when the applied voltage V (t) is increased from 2.2 kV_{p-p} to f 2.8 kV_{p-p} at f = 10 kHz in steps of 200 V. The voltage trace is shown in red colour while the discharge current trace is shown in blue colour.

In this discharge situation, individual microdischarges compete for the available surface area of the dielectric to deposit their discharge pattern. They also encounter residual charges occurring from previous discharge phases. Impinging ions, photons and charged species produce secondary electrons that feed into the microchannel. When the microchannel is sufficiently covered by the discharge, a thin region of high electric field and high positive-ion densities is established. Subsequently, charge accumulation at the dielectric surface leads to a local collapse of the electric field in the area defined by the surface charge. This effect limits the duration of the microdischarge to a few nanoseconds [19, 20]. From figure 5.4, we obtained the discharge current-voltage characteristics in filamentary mode at a fixed frequency of 10 kHz with applied voltage increasing from 2.2 to 2.8 kV_{p-p} in steps of 200 $V_{p-p.}$ The experimental difficulty was to stabilize a single filamentary discharge sufficiently to do repetitive measurements. Another difficulty was the limitation of the scope bandwidth (300 MHZ) to capture the same exact filament each time. In many cases, pulsed experiments are preferred for such measurements.

The filamentary mode of discharge is characterised by multiple current filaments that appear randomly and are typically about 10 - 100 ns in duration. These filaments appear just before the voltage climbs to a maximum for the positive half-cycle and before it reaches a maximum for the negative half-cycle. The filaments are seen to increase in number and in amplitude in some cases as the applied voltage were increased. A possible explanation could be that the dielectric barrier limits the growth of the filaments resulting from an increase in applied voltage, and this subsequently generates another filament and so on [19, 20]. In addition, the number density of microdischarge locations at the electrode surface rises with power density, which depends on the applied frequency and the peak voltage. During the rising part of the external voltage, additional

microdischarges are initiated at new locations because the presence of residual charges on the dielectric has reduced the electric field at positions where microdischarges have already occurred. Visible observation of the discharge in this mode shows a non-uniform discharge emission pattern and a bright blue glow. This is because higher currents are obtained at breakdown voltage due to the fact that the local field due to charge separation resulting from the difference in drift velocities of electrons and ions are superimposed on the applied field. The collisional ionization in this high-field region causes fast propagation of the ionization region and the formation of a bright plasma glow in the microchannel.

On voltage reversal, however, the next microdischarges will form at old microdischarge locations. This is known as the memory effect and is due to charge accumulation on the dielectrics from the previous discharges. In this period of opposite sign, it takes less external voltage swing to reach breakdown since the voltage has collapsed at these locations. Consequently, high-voltage low frequency operation tends to distribute the microdischarges on the available dielectric surface, while low-voltage, high-frequency operation tends to reignite the old microdischarge channels every half period. Here, at frequencies above 10 kHz, the discharge filaments become closer and fewer in number with some filaments overlapping each other (see figure 5.5). Figure 5.5 shows the discharge current-voltage characteristics in filamentary mode at a fixed frequency of 30 kHz with applied voltage increasing from 3.0 – 5.0 kV_{p-p}.

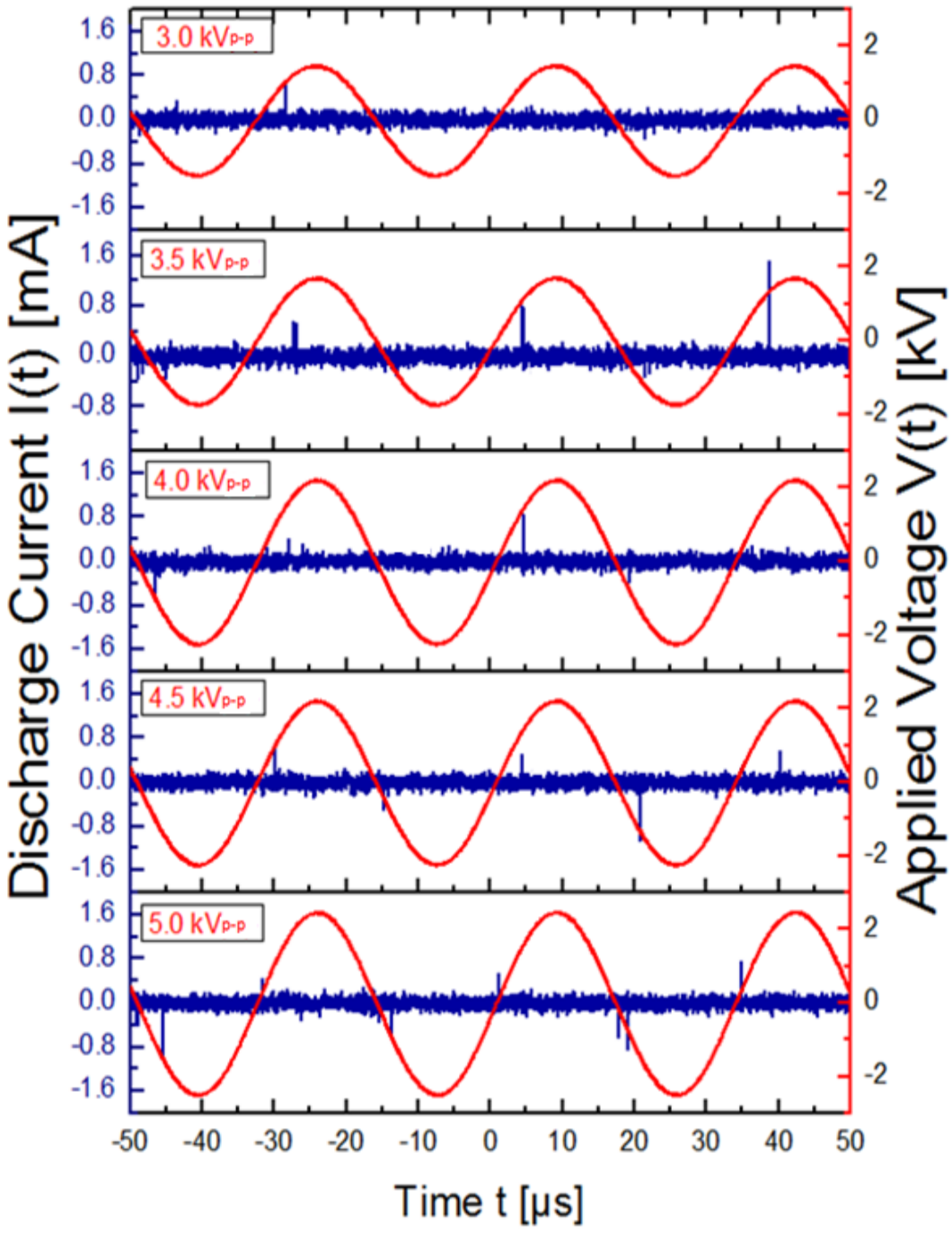

Figure 5.5: The discharge current waveform in filamentary mode when the applied voltage V (t) is increased from 3.0 kV $_{p\text{-}p}$ to 5.0 kV $_{p\text{-}p}$ at f = 30 kHz in steps of 500 V.

Here, very few filaments per half-cycle which alternate in each half cycle of the applied voltage are obtained. A possible explanation is that, if the repetition frequency is high enough, there may be additional memory effects due to residual gas heating and the presence of charged and excited species left over from the previous half period [19, 20]. Although, it has repeatedly been demonstrated that diffuse discharges can be obtained in barrier discharge configurations at about atmospheric pressure and gap widths up to several centimetres, this was not found in our case.

5.3.2 Optical Characterisation

Further investigation of the microdischarge behaviour was done using 2D optical ICCD imaging. Firstly, time - averaged images were taken across sections of the microchannel in order to determine whether or not the discharge behaviour was similar across electrode gaps of different length L. This was found to be the case from time averaged images obtained for different electrode lengths L = 300 μm and 500 μm and shown in figure 5.6a. Secondly, comparisons were made between discharges of the same electrode length. An example is shown in figure 5.6b for electrode length L = 500 μm. Here, the discharge patterns are both similar, so that we can expect our study of one electrode pair each of different lengths L = 300 μm and 500 μm to reflect the microdischarge behaviour in others.

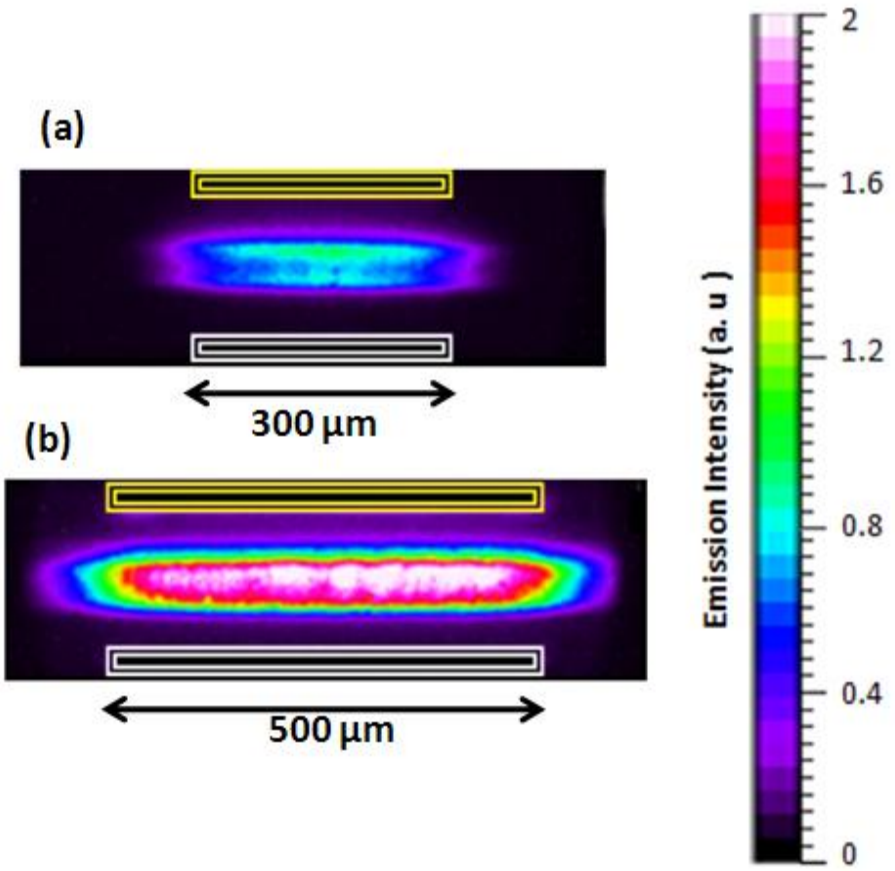

Figure 5.6 a: Time-averaged images of microdischarges driven by an ac voltage of 4.3kV_{p-p} for two different electrode lengths **(a)** L = 300 µm and **(b)** 500 µm.

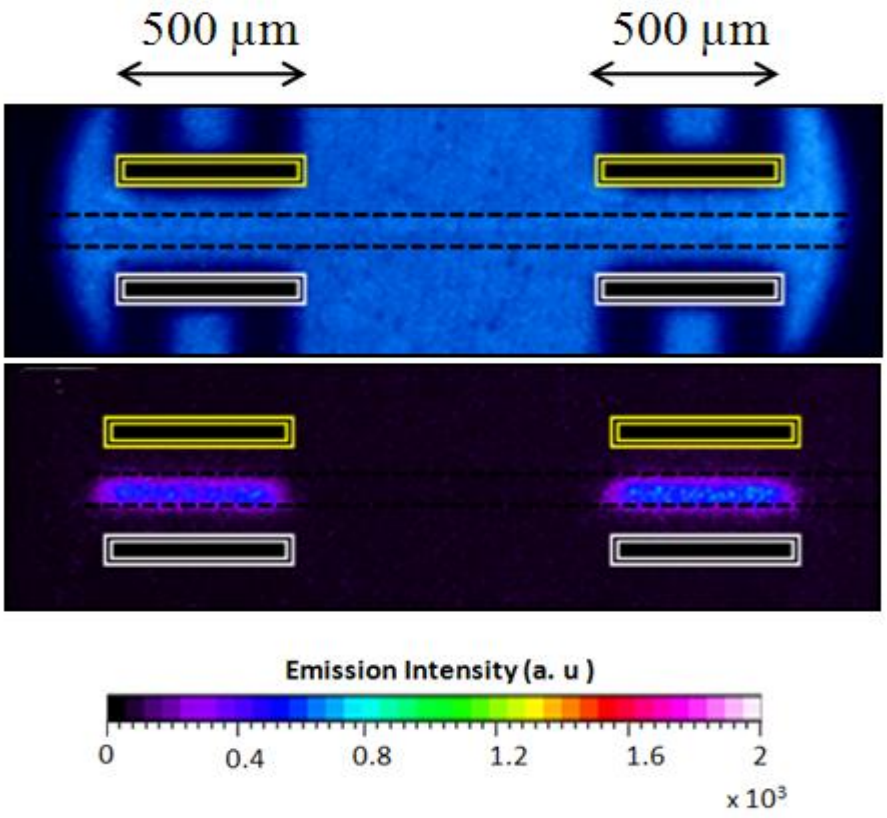

Figure 5.6 b: Time-averaged images of microdischarges driven by an ac voltage of 4.3kV$_{p-p}$ for the same electrode length. The top image shows the stage setting used while the bottom image shows time-averaged images for two individual electrode gaps with L = 500 µm

Time-resolved imaging was then used to investigate the evolution of the discharge in more detail and is shown in figures 5.7a and 5.7b. Images in figure 5.7a were acquired during the positive half-cycle and those in figure 5.7b during the negative half-cycle. For each figure, two sets of images are shown for electrode of length L = 300 µm (a – c) and L = 500 µm (d – f). The images were acquired with a 50 ns exposure time and they show different stages of the discharge

evolution along both the x and y axes. The applied voltage was V = 4.3 kV_{p-p} at a frequency f = 30 kHz. The upper electrode is the driven electrode and the lower electrode is the grounded electrode.

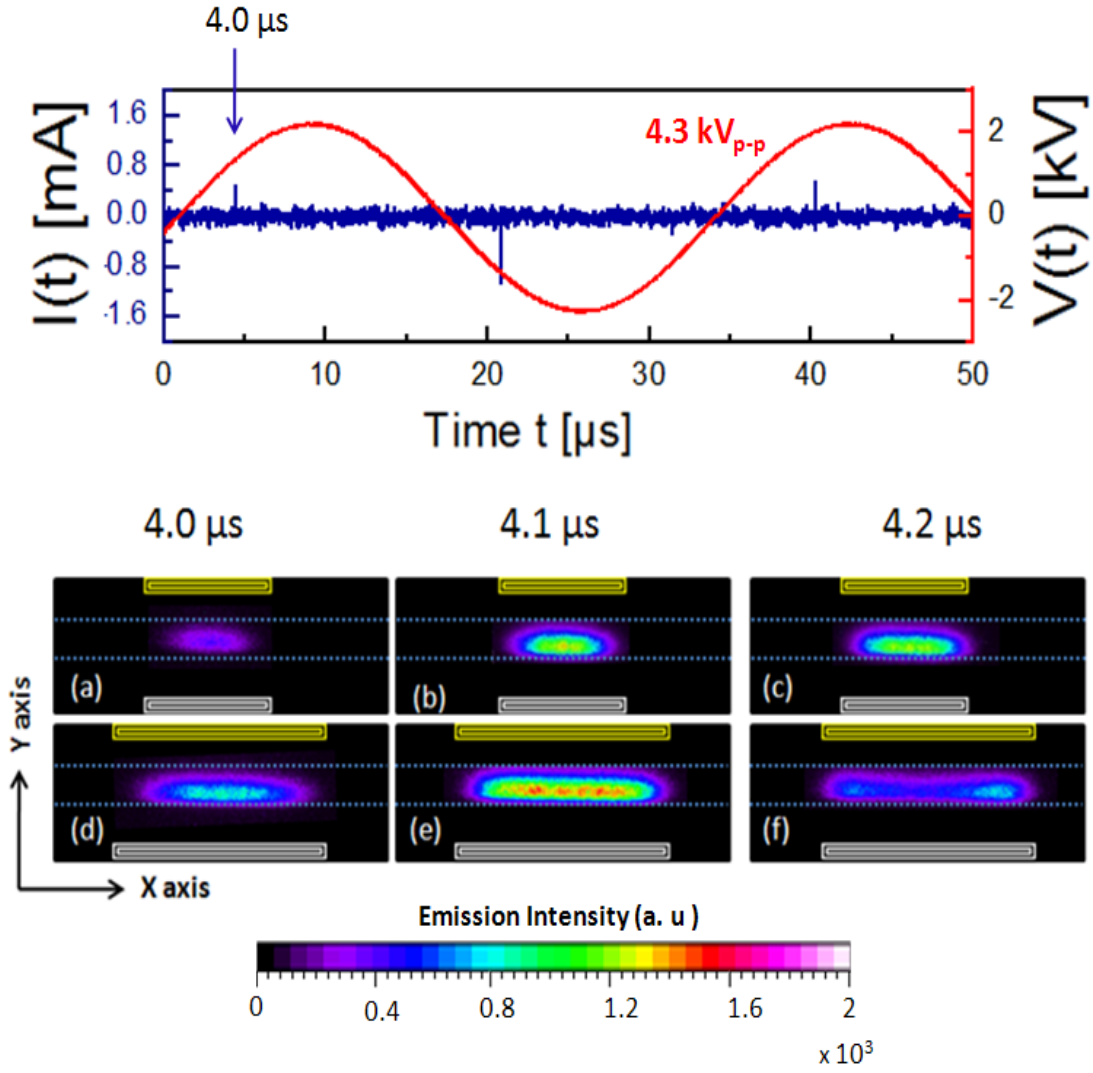

Figure 5.7a: Time resolved ICCD images reflecting various phases of the microdischarges occurring in helium (V= 4.3kV $_{p-p}$ and f = 30 kHz). Images taken with an ICCD gate of 100ns covering events occurring during the **(a)** Positive ac half-period. At time t = 4.0 µs, t = 4.1 µs and t = 4.2 µs. The driven electrode is shown on top while the counter electrode is shown at the bottom.

For both electrodes in figure 5.7a, the microdischarge first appears at the centre of the electrode lengths and equidistant from the electrode edges. Maybe this corresponds to the region with the narrowest electrode gap and highest electric field in volts per metre (v/m). The early development of the discharge in the middle of the electrode gap is clearly seen at time t = 4.0 μs before extending both upstream and downstream (at t = 4.1 μs and t = 4.2 μs) along the x axis. At later times, the discharge appears uniform, covering an area corresponding to the electrode length until its decay at t = 14.0 μs. A possible explanation is that when the x component of the electric field increases, it causes broadening of the discharge along the x axis due to decreasing charge concentration at the original centre position and so on as the charges respond to increasing electric fields at the electrode edges.

Now looking at the other half of the ac cycle (shown in figure 5.7b), the discharge re-ignites again at t = 22.4 μs. From the images obtained in the negative half-cycle when t = 22.4 μs and t = 22.5 μs, two intense emissions are seen at the corners of the electrodes. This could be attributed to the localisation of high electric fields and surface charge accumulation on the dielectric surface nearer the electrode edges from the previous discharge cycle resulting in increased charge density. It is well known that charges accumulate on the dielectric surface exposed to the discharge. Therefore, we can expect an enhancement of charge density near the electrode edges due to the discharge. Numerous studies also suggest that surface conditions seem to play a significant role for the stabilization of the discharge [21 – 24].

Etching of the dielectric surfaces, geometry, the surface composition and roughness, as well as the second emission coefficient of the dielectric are also factors that govern the behaviour of the discharge.

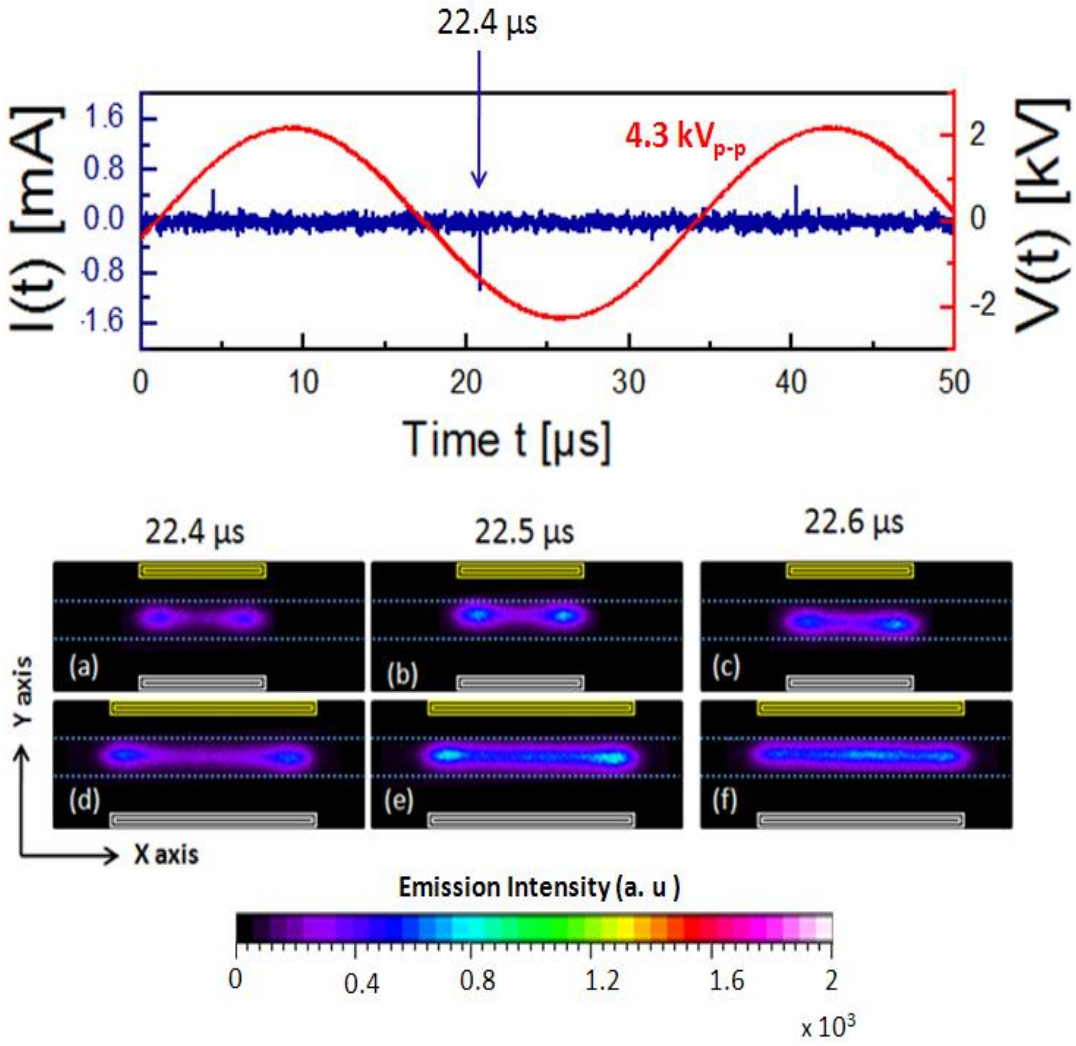

Figure 5.7b: Time resolved ICCD images reflecting various phases of the microdischarges occurring in helium (V= 4.3kV $_{p-p}$, and f = 30 kHz). Images taken with an ICCD gate of 100ns covering events occurring during the **(a)** Negative ac half-period. At time t = 22. 4 µs, t = 22. 5 µs and t = 22. 6 µs. The driven electrode is shown on top while the counter electrode is shown at the bottom.

At a later time t = 22.6 μs, we notice a broadening of the discharge both upstream and downstream across each length of the electrodes. After t = 22.6 μs, a more uniform emission is again observed across the entire gap along the x axis. Figure 5.8 shows the expansion of the discharge along the x-axis for both L = 300 μm and L = 500 μm.

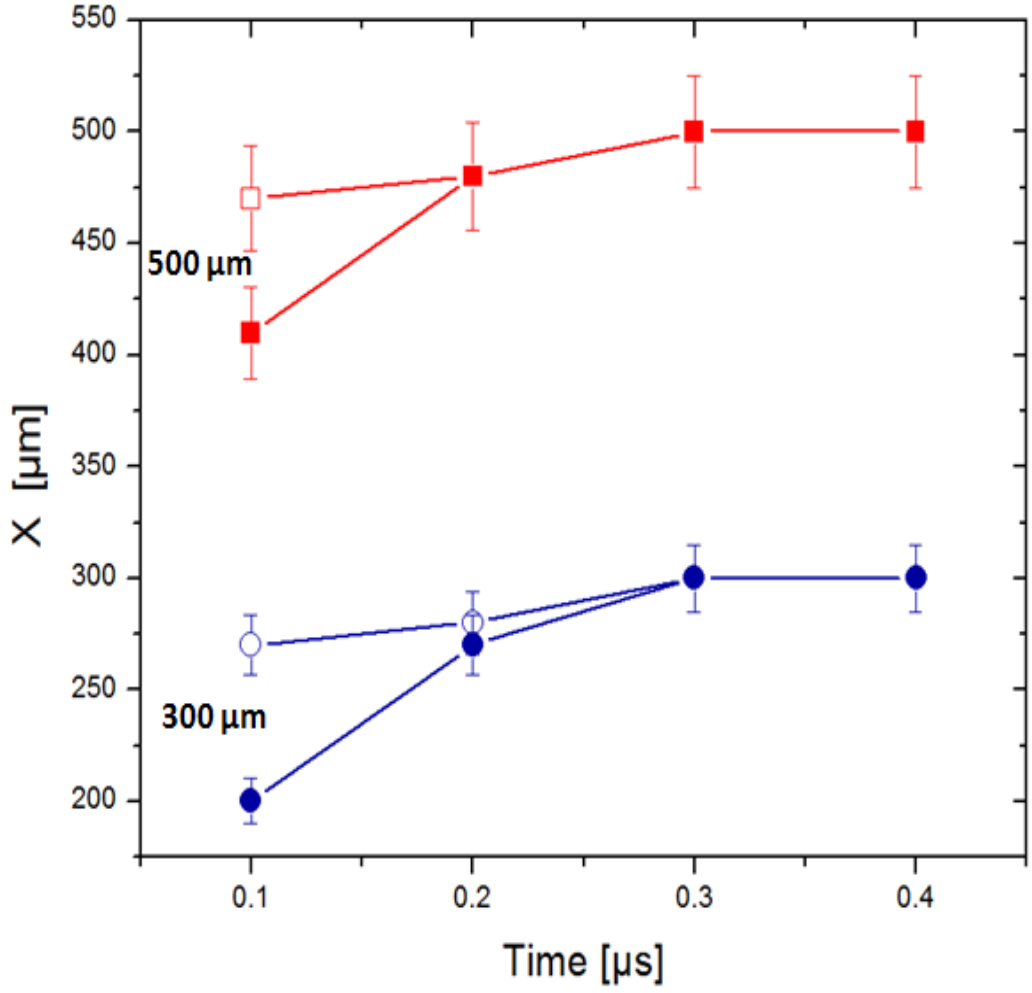

Figures 5.8: Shows the expansion of the microdischarge along the microchannel (x-axis) direction against time. For electrode gaps at L = 300 μm and L = 500 μm. The open symbols are for the negative half-cycle and the closed symbols for the positive half-cycle.

The values obtained are shown with an error bar of 5 %. Since the discharge expansion is limited by the microchannel width i.e. 50 μm in the y-axis direction, we have only estimated an expansion of about 100 – 200 m in the x- axis direction. This corresponds to an average expansion of (10 – 20) μm every 100 ns.

Table 5.1: Shows the physical parameters used to calculate current density

Depth **D (m)**	**Length** **L (m)**	**Width** **W (m)**	**2(DL+LW+DW)** **Area (m^2)**
50×10^{-6}	300×10^{-6}	50×10^{-6}	6.5×10^{-8}
50×10^{-6}	500×10^{-6}	50×10^{-6}	10.5×10^{-8}
50×10^{-6}	800×10^{-6}	50×10^{-6}	16.5×10^{-8}

The maximum electrical power P (Watts) ~ 2 W supplied to the system has been calculated from values obtained using the expression $P = I V \cos\theta$, where $\theta = 86^\circ$ is the phase difference between the current and voltage traces. Low values of current densities J (A/cm^2) of up to ~ 8 A/cm^2 were obtained across the electrode gaps using the values calculated in Table 5.1. These values are extremely small in comparison to high current densities of ~ 1000 A/cm^2 for 1 mm gap at 1 bar in air when low-pressure glow discharges were scaled to atmospheric pressure [20].

5.4 CONCLUSIONS

Dielectric barrier discharges can exhibit a variety of different discharge modes including filamentary and diffuse modes, depending on the gas composition, the dielectric surface properties and the operating conditions. The distinct mode observed was the filamentary mode, generated in microchannels of lengths L = 300 μm and L = 500 μm of a patterned microfluidic chip. This mode of discharge is characterised by multiple current filaments that appear randomly and are about (10 – 100 ns) in duration. These current filaments appear and alternate in each half cycle of the applied voltage. Visible observation of the microchannel in this mode reveals a bright blue glow.

The behaviour and evolution of the microdischarges were studied using time resolved ICCD imaging and electrical voltage-current measurements. Time resolved images show that the microdischarge ignites at the centre for the positive half-cycle and at the edges for the negative half-cycle within the microchannel. The microdischarge ignition and evolution have been interpreted based on the surface charge accumulation on the dielectric electrodes. High intensity emission region are seen for both positive and negative half-cycles, possibly in regions of high electric fields and lower intensities in the surrounding regions.

References

1) M. Loughran, S. W. Tsai, K. Yokoyama, I. Karube, Curr. Appl. Phys. 2003, 3, 495

2) S.-W.Tsai, M. Loughran, A. Hiratsuka, K. Yano, I. Karube, Analyst 2003, 128, 237

3) V. Barbier, M. Tatoulian, H. Li, F. Arefi-Khonsari, A. Ajdari, P. Tabeling, Langmuir .2006, 22, 5230

4) M. Salim, G. Mishra, G. J. S. Fowler, B. O'Sullivan, P. C. Wright, S. L. McArthur, 2007. Lab Chip, 7, 523

5) A. J. Beck, F. R. Jones, R. D. Short, Polymer 1996, 37, 5537

6) T. Hayakawa, M. Yoshinari, K. Nemoto, Biomaterials. 2004, 25, 119

7) R. Jafari, M. Tatoulian, W. Morscheidt, F. Arefi-Khonsari, React. Funct. Polym. 2006, 66, 1757

8) A. K. Walker, H. Qiu, Y. Wu, R. B. Thimmons, G. R. Kinsel, Anal. Biochem., 1999, 271, 123

9) C. Geßner, V. Bartels, T. Betker, U. Matucha, C. Penache, C.-P. Klages, Thin Solid Films. 2004, 459, 118

10) S. Kreitz, C. Penache, M. Thomas, C.-P. Klages, Surf. Coat. Technol. 2005, 200/1-4, 676

11) G. Nersisyan and W. G. Graham, Plasma Sources Sci. Technol.2004,13

12) U. Kogelschatz, IEEE Trans. Plasma Sci. 2002, 30

13) I. Radu, R. Bartnikas and M. R. Wertheimer J. Phys.D: Appl. Phys. 2004, 37 449

14) N. Gherardi, G. Gouda E. Gat ,A. Ricard and F. Massines, Plasma Sources Sci. Technol.2000, 9 340

15) J. Guikema J, N. Miller, J. Niehof, M. Klein and M. Walhout, Phys.Rev. Lett. 2000, 85 3817

16) I. Brauer I, C. Punset, H. G. Purwins and J. P. Boeuf, J. Appl. Phys. 1999, 85, 7569

17) P. Xu and M. J. Kushner, J. Appl. Phys. 1998, 84, 4153

18) O. T. Olabanji and J. W. Bradley, Surf. Coat. Technol. 2011, 205, S516

19) U. Kogelschatz, Plasma Chem. Plasma Process. 2003, 23, 1

20) U. Kogelschatz, B. Eliasson and W. Egli, Dielectric-Barrier Discharges. Principles and Applications; J. Phys. IV. France 07 (1997), pp C4 - 47

21) N. Tandon, A. Marsano, R. Maidhof, K. Numata, C. MontouriSorrentino, C. Cannizzaro, J. Voldman and G. Vunjak-Novakovic, Lab Chip, 2010, 10, 692–700.

22) K. J. Lee, K. A. Fosser and R. G. Nuzzo, Adv. Funct. Mater., 2005,15, 557–566

23) S. A. Al-Bataineh, E. J. Szili, A. Mishra, S. J. Park, J. G. Eden, H. J.Griesser, N. H. Voelcker, R. D. Short, D. A. Steele. Plasma Processes and Polymers, 2011, 8, 695 -700

24) K. S. Lim, W.-J. Chang, Y.-M. Koo and R. Bashir, Lab Chip, 2006, 6,578–580.

CHAPTER SIX

6.0 Head-on surface modification and spatio-temporal behaviour of a micro- jet

Abstract

We report a systematic study of the behaviour of an atmospheric-pressure microjet using standard electrical characterisation, Schlieren photography and optical 2D imaging. The microjet was created in a capillary tube of about 1mm diameter using flowing helium gas. A sinusoidal voltage of up to 8 kV_{p-p} with frequencies from 10 kHz to 30 kHz has been applied to two copper ring electrodes covering the capillaries and separated at a distance of 2 cm. Schlieren photography of the helium outflow shows two distinct regions i.e. laminar and turbulent regions. The length of the laminar region varies from 2 to 5 cm and appears to increase with increasing flow rate up to 2.25 slm before decreasing. Above this flow rate, the length of the laminar region decreases and more turbulence is observed. Also, the visible plasma plume extends out of the capillary up to a distance of 2 cm when the flow rate is increased. The intensity of this plume changes with increasing frequency and applied voltage. Water contact angle measurement results from treated polystyrene (PS) samples exposed directly facing the microjet reveals a change from a hydrophobic to a hydrophilic surface. A ripple like effect with a much larger area than that of the capillary is seen on treated samples positioned "head-on" and up to a nozzle-substrate distance of 3 cm. AFM imaging of the treated region provides information on the morphology of the treated surface.

6.1. INTRODUCTION

Microplasmas have attracted more and more attention due to their unique characteristics, such as weakly-ionized, boundary dominated phenomena and high ion density. Some have been developed in environmental, UV radiation source and plasma-reactors fields [1, 2]. Microplasmas operated either at atmospheric or reduced pressure exist in various configurations. Among these are, direct current (dc) discharge glow discharges used as molecular emission detectors as demonstrated in [3, 4], electrolyte-as-cathode glow discharges (ELCAD) [5, 6], liquid-sampling atmospheric pressure glow discharges e.g. [7, 8], miniature inductively coupled plasmas [9], capacitively coupled radio-frequency discharges [10 -12], microwave induced plasmas using microstrip technology [13], dielectric barrier discharges [14 - 16], microstructure electrode discharges (MSD) e.g.[17, 18] and other variations [19]. Diagnostic studies of various microplasmas have been carried out using a variety of established techniques ranging from electrical characterization to various optical diagnostics methods and plasma mass spectrometry. These include time-averaged and time-resolved studies. The basic parameters that characterize microplasmas include I-V characteristics, electron density, and temperature, as well as electron energy distribution, radiative properties and gas temperature. Excitation of microplasmas in various configurations can occur by direct current (dc), pulsed dc, alternating current (ac), radiofrequency (rf), and microwave sources. Here, we have characterised our microjets using standard current-voltage electrical measurements, ICCD imaging and Schlieren imaging.

Figure 6.1 shows an operation in a capillary surrounded by two ring electrodes, where the dielectric barrier discharge is between the electrodes, and where gas flow extends the plasma out of the capillary. Applications of this atmospheric pressure dielectric barrier discharge

include the detection of chemical warfare analytes, for the detection of gas phase compounds [20], drugs and explosives, medical applications [21, 22], surface modification [23, 24], wound treatment [25], sterilization [25, 26], and for process control, food and safety [27].

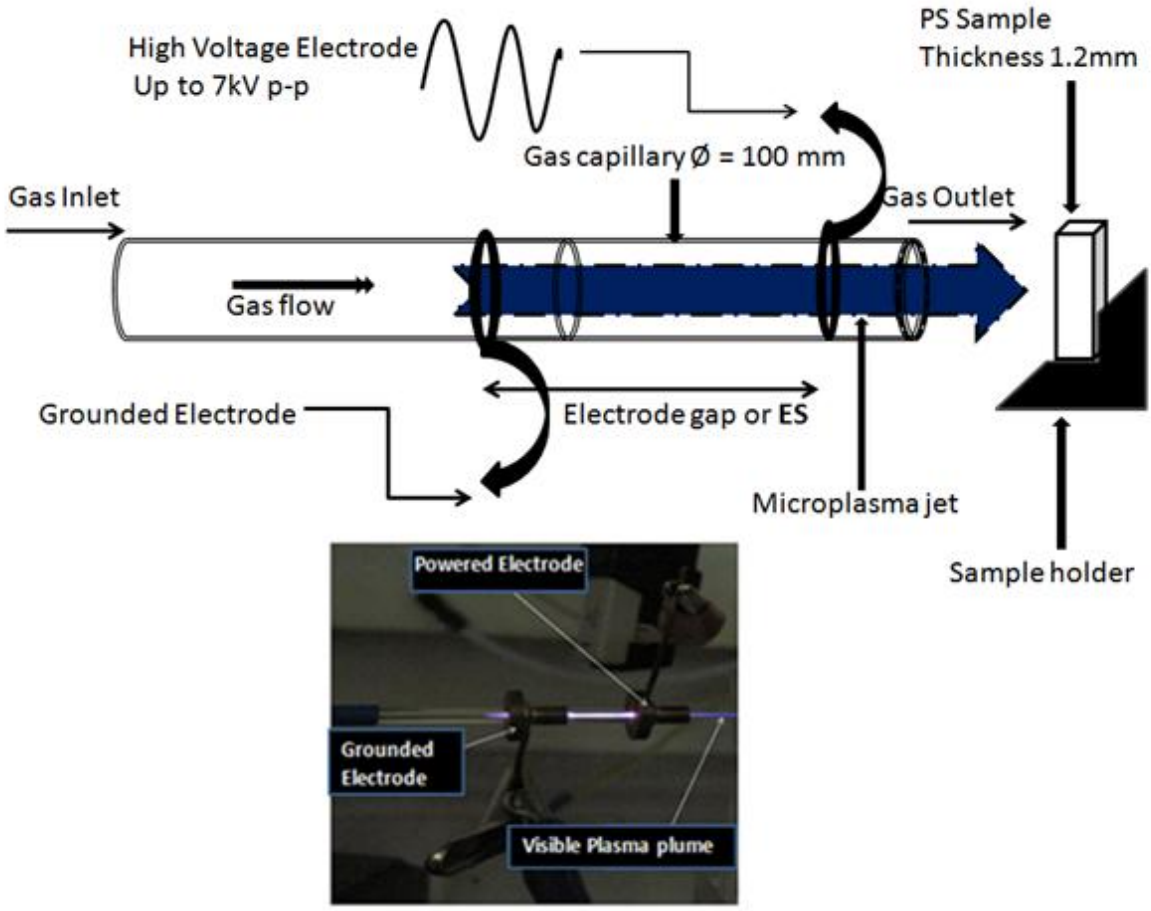

Figure 6.1: A schematic of the microplasma jet setup

6.2 Experimental Setup

6.2.1 Power Supply

The experimental arrangement used is based on the dielectric barrier discharge mode of operation and similar to that reported in [28] and previously discussed (see chapter 3). The gas flow was manually controlled by a Rotameter (Omega FLT-39ST) connected to a Polytetrafluoroethylene (PTFE) tube on one end and the gas cylinder on the other. The flow rate F_R (standard litres per minute, slm) through the capillary was varied between 0.67 slm and 5.4 slm by adjusting the rotameter/flow meter. A sinusoidal high voltage of up to 8 kV_{p-p} is applied at frequencies of 10, 20 and 30 kHz to one of the copper ring electrodes while the other is grounded. We have used this configuration to calculate lowest and highest exit gas velocities of 14.13 m s^{-1} and 114.6 m s^{-1} at flow rates of 0.67 slm and 5.4 slm respectively. This was done at a frequency of 30 kHz, assuming no gas leakage in the system and laminar gas flow in the glass capillary.

6.2.2 Water Contact Angle (WCA) Measurement

The microplasma jet setup (shown in figure 6.1) has been used for the surface treatment of polystyrene (PS) samples (thickness 1.2 mm, Goodfellow Cambridge Ltd.). Each PS sample was prepared as described (see chapter 3). The clean samples were then introduced head-on to the plasma plume for 1 and 2 minutes respectively.

6.3 Results and Discussions

6.3.1 Voltage-current measurements

Standard electrical (Voltage-Current) measurements were obtained at a frequency of 10 and 20 kHz when the applied voltage was increased up to 9 kV_{p-p}. Figure 6.2a shows the time varying total current waveform characteristics as a function of the applied voltage V (t) at a frequency of 20 kHz. Here, we notice one distinct peak per half cycle in the current waveform at and beyond breakdown voltage, similar at 10 kHz and 30 kHz. The peak duration is of the order of a few microseconds (~ 3 μs).

The sinusoidal displacement current observed in the waveform (which can be measured without gas flow) was removed from the total current waveform to give the true discharge current value. Figure 6.2b also shows the total current characteristics as a function of applied voltage with and without (w/o) plasma jet struck. The points a and b correspond to the point at which breakdown occurs at 10 kHz and 20 kHz respectively when the applied voltage is increased up to 9 kV_{p-p}. Here, we notice that breakdown voltage changes slightly when the applied frequency was increased from 10 to 20 kHz respectively but ~ 7 kV_{p-p} across the three frequencies. These variations in frequency and applied power become significant during sample treatment because they cause changes in the lengths of the laminar and turbulent regimes. Within the capillary, the main discharge contains neutrals, photons, He metastables and charged species such as electrons and positive He^+ ions. Outside of the capillary, the plasma plume interacts with ambient air forming new ionic and excited species, such as O^+, OH^+, O^*, O^- and N_2^+ [30, 31].

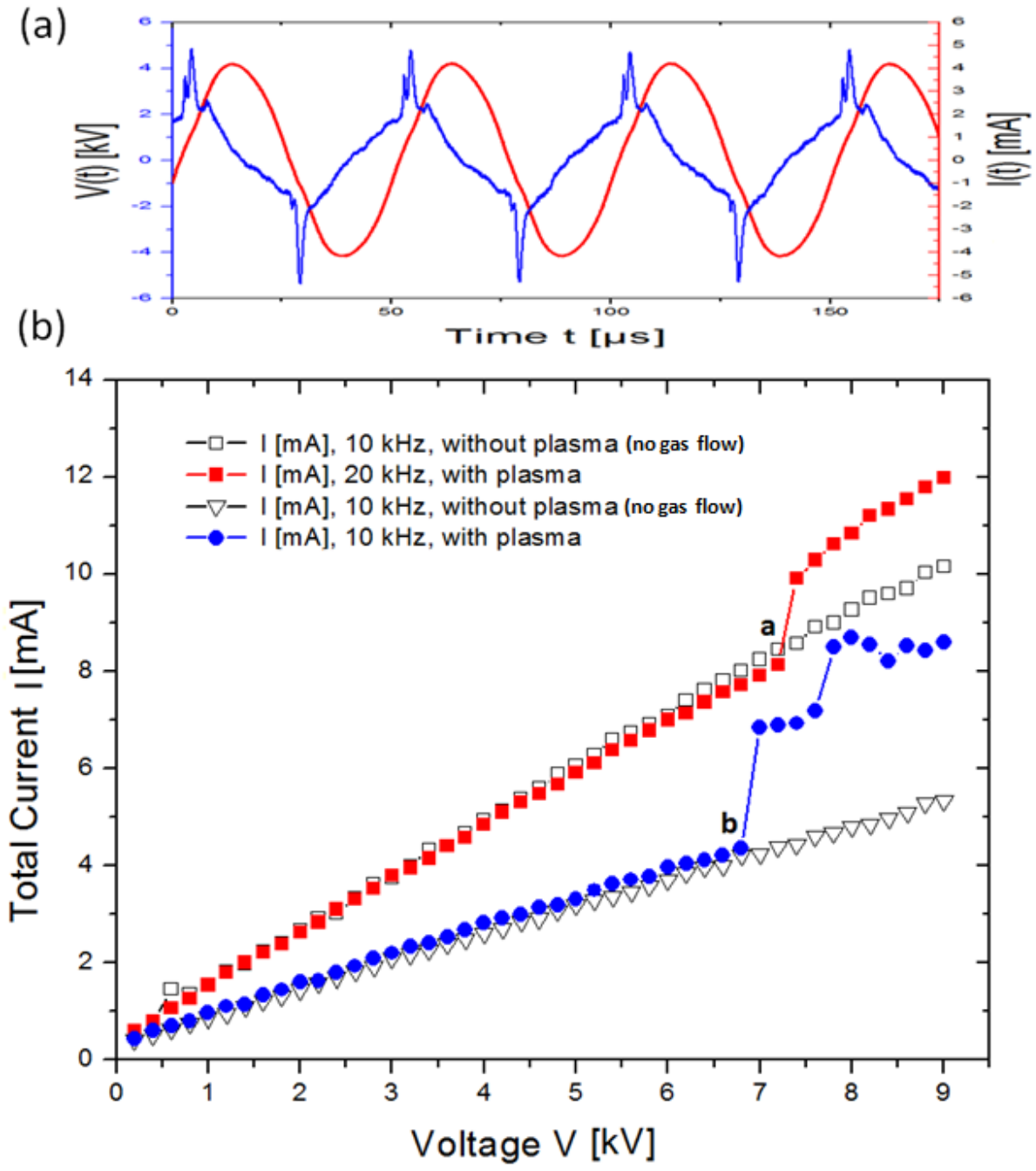

Figures 6.2: (a) A graph showing the relationship between total current I (t) in milliamperes and applied voltage V (kV). **(b)** Current-Voltage relationship when applied frequency is varied from 10 kHz to 20 kHz with plasma struck and without (w/o) plasma struck. Points a and b correspond to breakdown voltage at 10 kHz and 20 kHz respectively.

6.3.2 Time-averaged and Time-resolved Measurements

Time averaged and time-resolved images have been used to investigate the behaviour of the plasma plume using 2D optical ICCD imaging with 50 ns time resolution. The optimum configuration that gives the most stable, intense and longest length of the plasma exit plume was obtained by varying the applied voltage and the frequency (shown in figure 6.3).

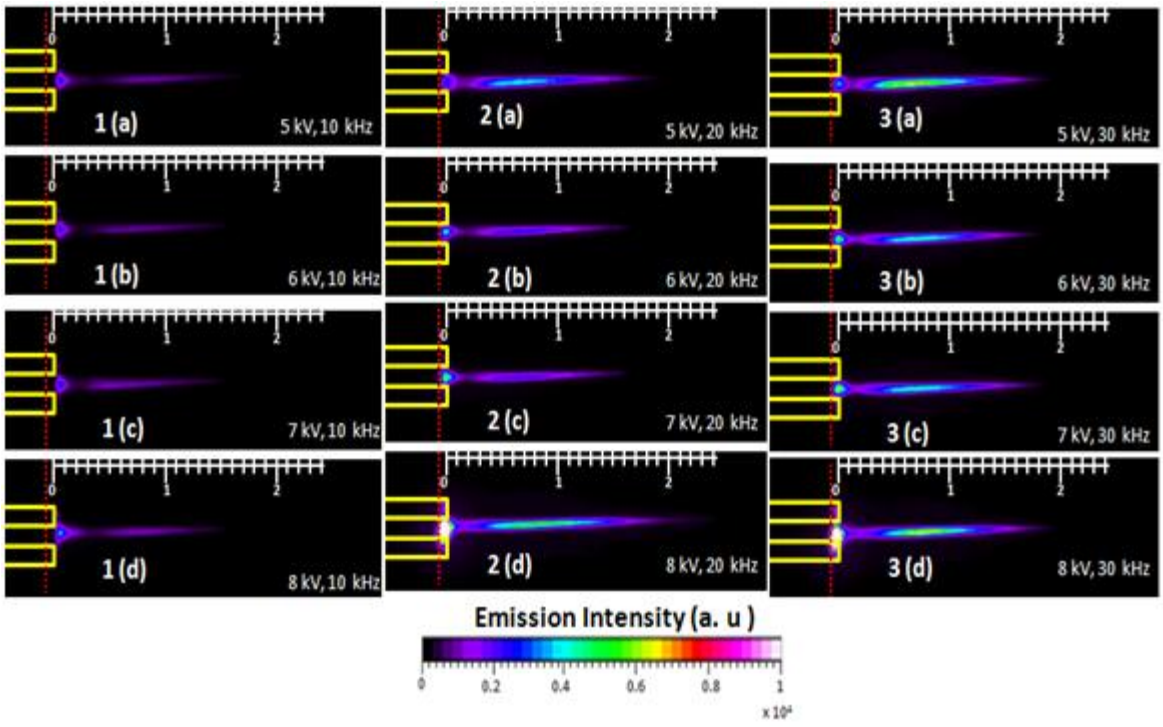

Figure 6.3: Time averaged ICCD images showing the effects of changes in the applied voltage from 5 - 8 kV_{p-p} (a to d) and applied voltage frequency from 10 to 30 kHz on the plasma plume behaviour.

This figure 6.3 shows variations in the visible plasma plume length and intensity as a function of applied frequency from 10 - 30 kHz and applied voltage from 5 - 8 kV, for a fixed flow rate of 3.6 slm. Here, we notice an increase in plasma plume length and intensity as the applied voltage is increased from 5 - 8 kV (a to d).

However, changes in the localisation or diameter of the visible plasma plume are completely negligible.

As the frequency is increased from 10 - 30 kHz (1 to 3), the change in the localisation of the visible plasma plume becomes noticeable and this causes the plume to broaden along its radial and axial centres. Further investigation into the spatiotemporal behaviour of the plasma bullets as they exit the nozzle was carried out. As described in [32], plasma bullets are fast moving discrete regions of ionization contained within the plasma plume. The results obtained are shown in figures 6.4 for 10 kHz, 20 kHz and 30 kHz respectively.

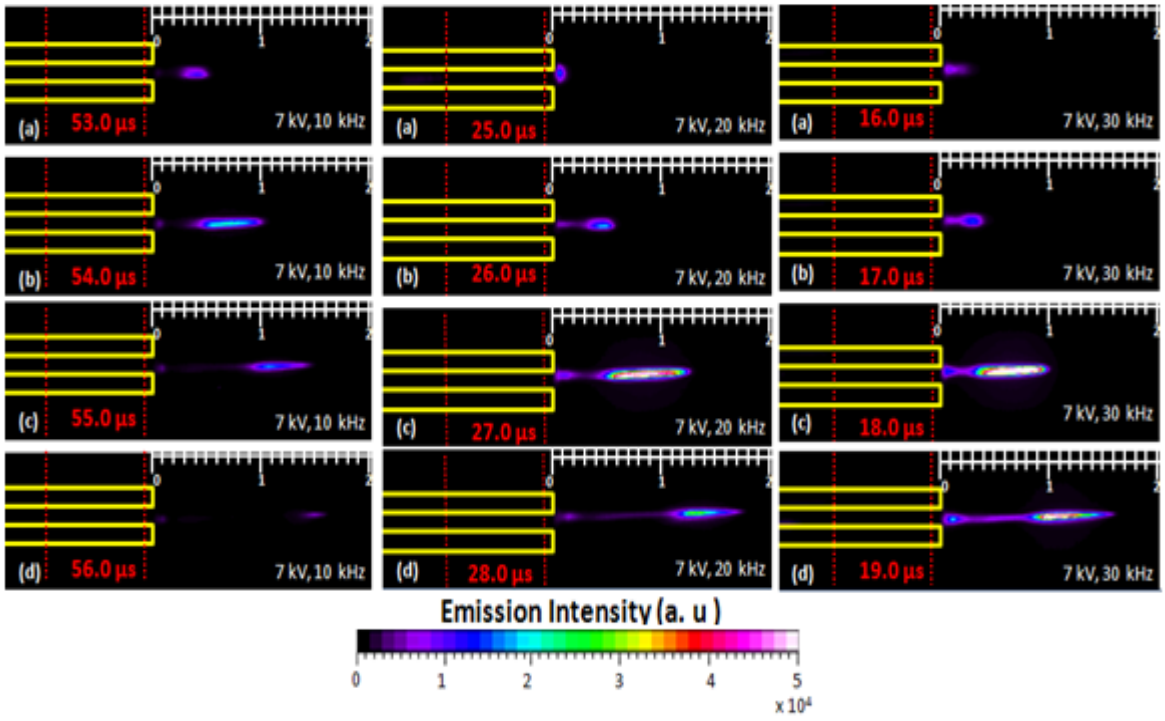

Figure 6.4: Time resolved ICCD imaging of plasma bullets obtained with a 50 ns time resolution, flow rate F_R = 3.6 slm and applied voltage of 8 kV_{p-p}. The image shows the spatiotemporal behaviour of the bullets at a frequency f = 10, 20 and 30 kHz.

Here, individual plasma bullets are seen as they exit the nozzle figure 6.4 (a to d). The regions marked in red-dashed lines correspond to the non-visible regions due to the opaque nature of the driven electrode. A fixed flow rate of 3.6 slm has been used to calculate bullet speeds of ~ 8 km/s as the bullet escapes out of the nozzle. It subsequently propagates for a few microseconds before decelerating to ~ 4.6 km/s at f = 10 kHz, ~ 5 km/s at f = 20 kHz and ~ 6 k/s at f = 30 kHz over the next few nanoseconds.

This behaviour is in good agreement with those obtained in [33] and other studies [32, 34, 35]. Continuous gas speed at the exit of the nozzle has been calculated to be ~ 77 m/s. The Reynolds number (R_e) was calculated using the expression $R_e = V L/\nu$, where V refers to the mean fluid velocity, L refers to the minimum system scale length (for 1mm nozzle diameter) and ν refers to the kinematic viscosity of the fluid (1.22×10^{-4} for helium and 1.57×10^{-5} $m^2s^{-1}$for air, both at 300 K). This gives a R_e value of ~ 630 in the laminar regime for helium and a value of ~ 4900 in the turbulent regime for air because laminar flows occur at low Reynolds number (< 2000) while turbulent flows occur at high Reynolds number (> 4000) [36].

6.3.3 Head- on surface treatment

The surface morphology of treated PS surface has been investigated. AFM images of treated PS samples positioned head-on to the plasma plume at a nozzle-sample distance of 10 mm for 3 minutes reveal surface damages and non-uniform surface modification. In this particular case, the frequency was maintained at 10 kHz. Results reveal holes and ripple effects on treated surfaces (shown in figures 6.5 and 6.6 respectively).

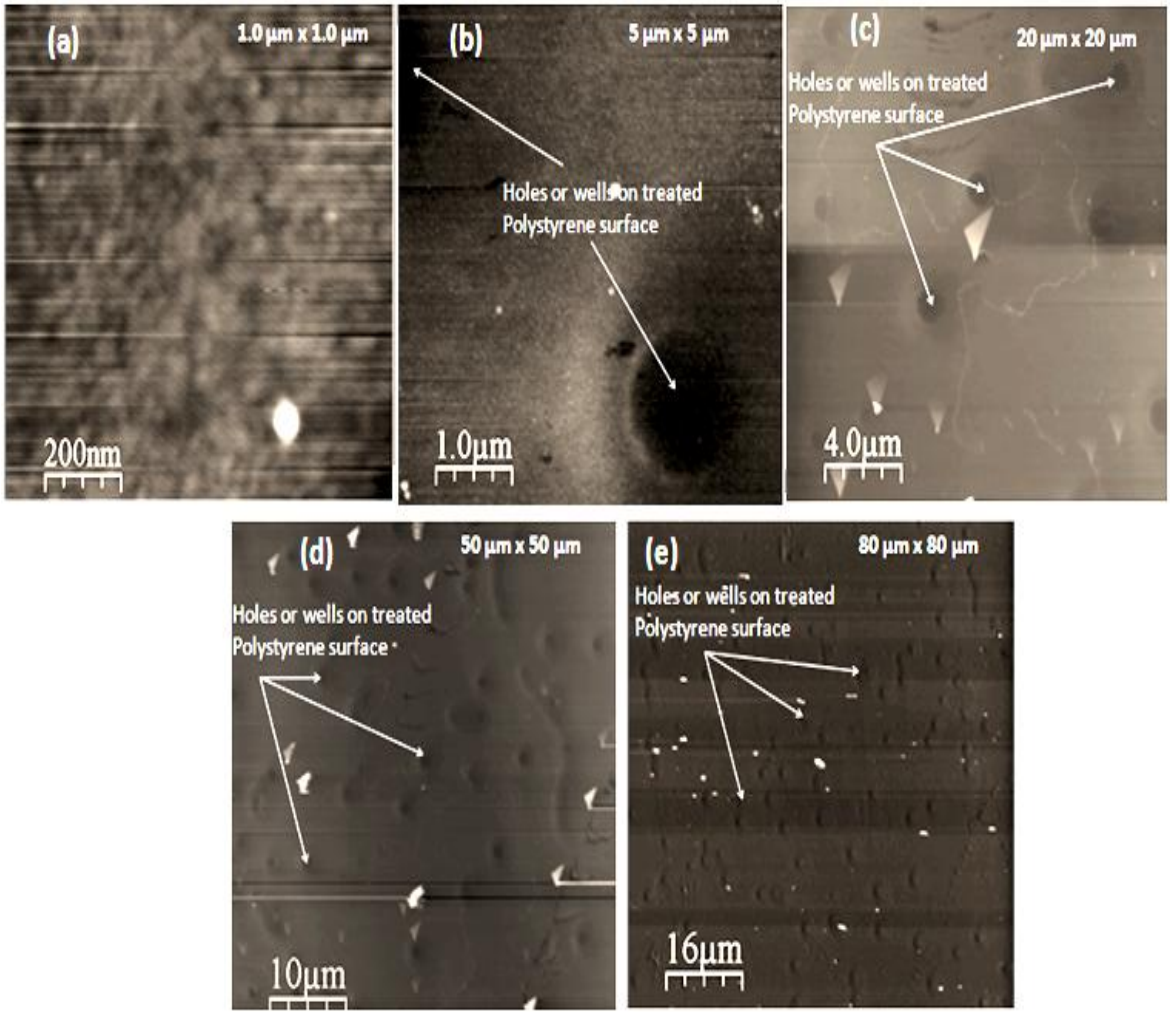

Figures 6.5: AFM images showing holes/wells observed on treated PS surface after a period of 3 minutes using flowing helium gas. V = 8 kV_{p-p}, f = 10 kHz, F_R = 1.38 slm. **(a)** 1 µm x 1 µm **(b)** 5 µm x 5 µm **(c)** 20 µm x 20 µm **(d)** 50 µm x 50 µm **(e)** 80 µm x 80 µm

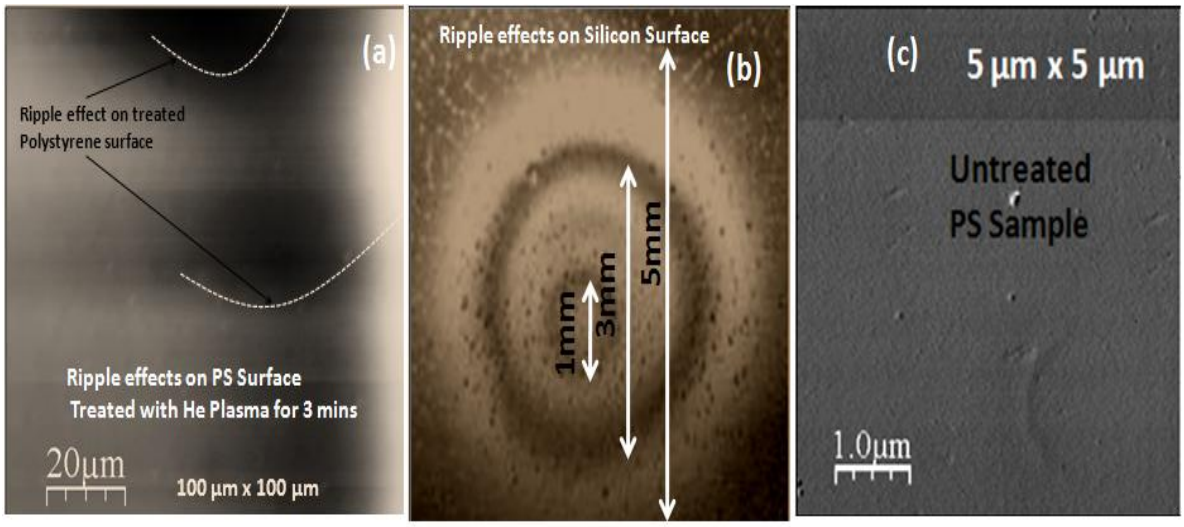

Figures 6.6: Images showing surface morphology and "ripple effect" on **(a)** AFM image of PS sample after a treatment period of 3 minutes using flowing helium gas. V = 8 kV_{p-p}, f = 10 kHz **(b)** microscopic image of ripple effect on silicon surface and **(c)** AFM image of untreated PS sample (size: 5 µm x 5 µm)

Figure 6.5 shows holes/wells and damages on the treated PS Surface. This could be due to bond breaking on the polystyrene surfaces resulting from heavy bombardment from newly created ionic species, charged species as well as species such as UV or VUV photons within the plasma plume travelling at a high impact velocities ~ 4 to 6 km/s and directly hitting the PS surface.

Figures 6.6 a and b show examples of ripple effect. The ripple effect is a pattern showing concentric ring regions of different depths where the highest level of treatment is obtained at a region corresponding to the radial centre of the plasma plume. This spot then appears to propagate isotropically in all directions like a water ripple.

For clarity purposes, an example of a ripple effect on a silicon surface positioned at a similar distance from the nozzle-tip is also shown in figure 6.6 b. This image was taken with the aid of an optical microscope. Here, the region of the highest treatment on the treated PS surface appears to be in the middle of the ripple and tends to progressively spread outwards in all directions until it reaches a maximum diameter corresponding to the region of lowest treatment. In this work, this diameter can sometimes increase beyond a factor of five times (x5) the capillary diameter. A suggestion that the region of the highest surface treatment may be due to an inner core of VUV photons surrounded by an envelope of radical species at large distances from the visible plume has also been reported [24].

6.3.4. Schlieren Imaging results

Schlieren imaging of the plasma plume reveals two distinct regions corresponding to the laminar and turbulent regions. The first region is the laminar region (pre-onset of visual instability) and it is usually slightly longer than the visible plume while the turbulent region (post-onset of visual instability) is invisible to the naked eye. Figures 6.7 and 6.8 show the relationship between the changes in the length of both discharge regions when the applied voltage (kV) and flow rate F_R (slm) are varied.

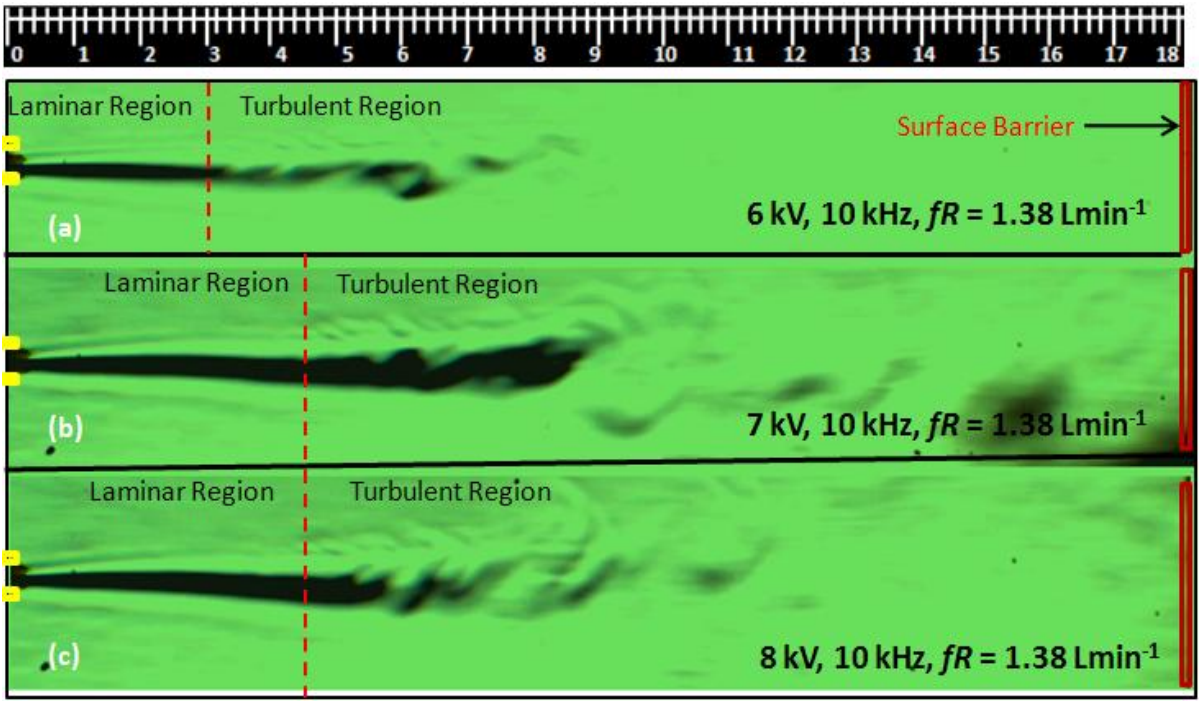

Figures 6.7: Schlieren photographs showing various lengths of laminar and turbulent flows as a function of increasing applied voltage from a to c when applied voltage is increased from 6 to 8 kV_{p-p}. Flow rate was maintained at F_R = 1.38 slm.

From figure 6.7, as the applied voltage is increased from 6 to 8 kV keeping the flow rate constant at F_R = 1.38 slm, we notice an increase in the length of the laminar region up to a certain point beyond which a further increase in voltage no longer affects the length of the laminar region but instead creates more turbulence.

Figure 6.8 on the other hand shows the changes in the laminar region at a fixed applied voltage of 8 kV. Here, we notice an increase in the length of the laminar region as the flow rate is increased from 0.67 to 2.25 slm i.e. a to c and subsequently a decrease in the length of

the laminar region as the flow rate is increased beyond 2.25 slm up to 4.4 slm i.e. d and e. Changes also occur in the laminar and turbulent regions when the plasma is struck in comparison to when the plasma isn't struck (Shown in figure 6.9).

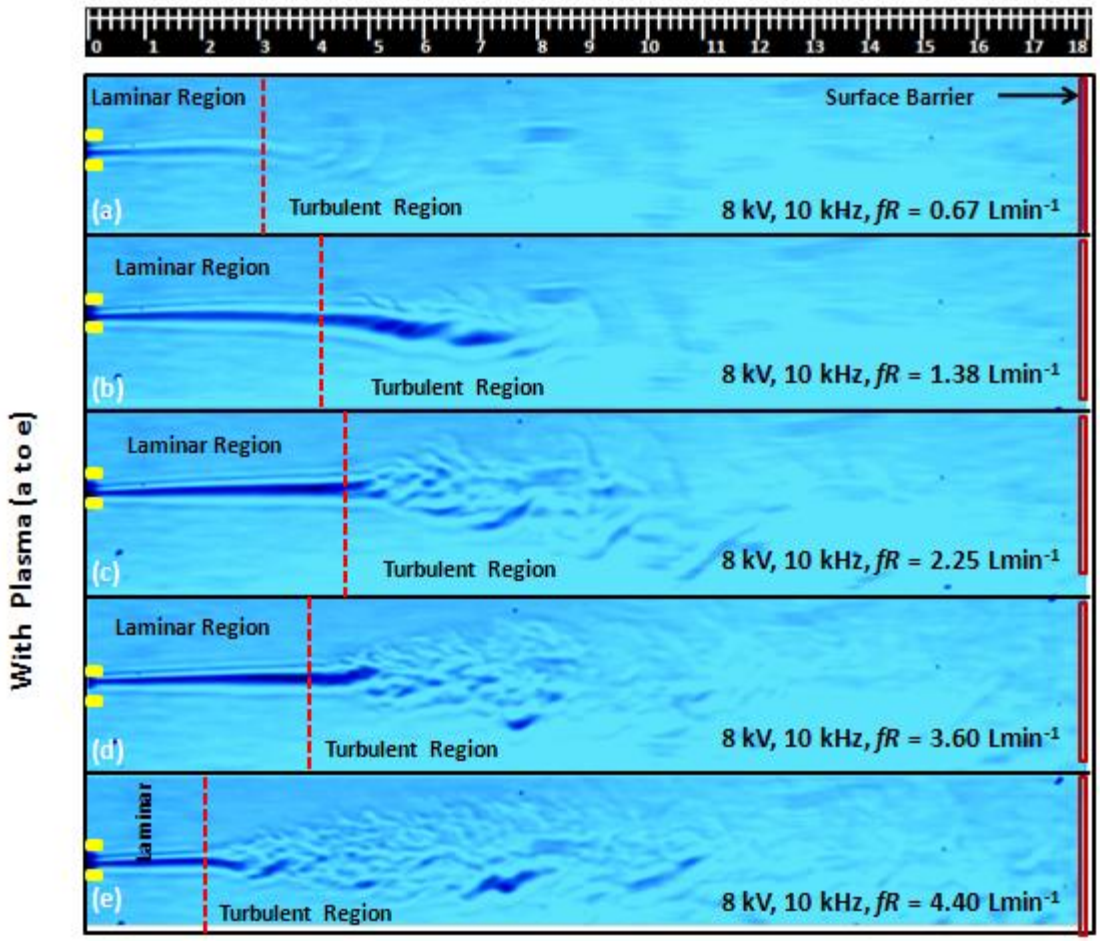

Figure 6.8: Schlieren photographic images showing changes in laminar and turbulent flows when the flow rate is increased from F_R = 0.67 slm to 4.4 slm. i.e. a to e with plasma struck. The plasma was operated at a peak voltage of 8 kV_{p-p}, frequency f = 10 kHz and at an electrode gap of 20 mm.

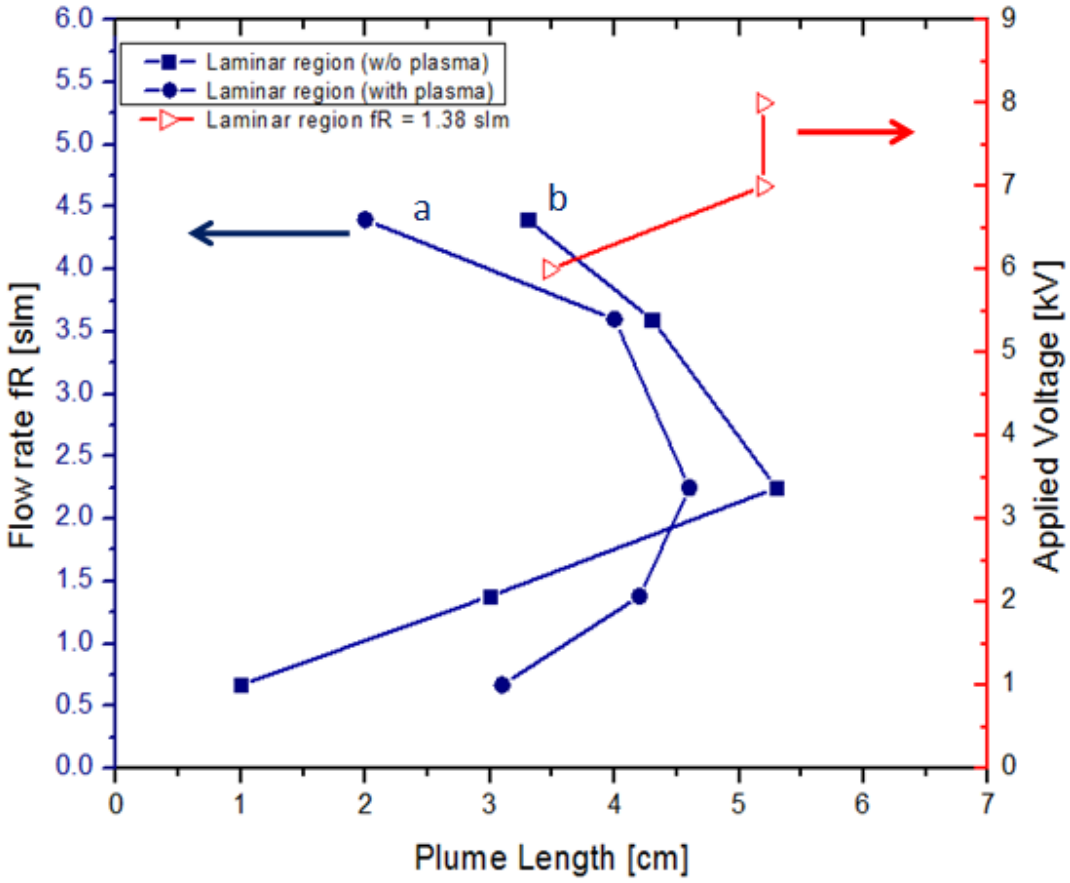

Figures 6.9: A graphical representation showing the relationship between plume length and flow rate for **(a)** with plasma struck and **(b)** without plasma struck. The graph also shows the variation in plume at a fixed flow rate F_R = 1.38 slm when the applied voltage is increased from 6 to 8 kV_{p-p}.

From previous studies [33], the mechanisms responsible for changes in length of the laminar region when the plasma is struck can be attributed to (1) the combination of gas heating through elastic electron-neutral collisions and (2) ion momentum transfer to the neutral gas thus resulting in higher exit gas velocities and earlier turbulences from increased flow rates.

The correlation between the plasma plume length and gas flow rate has also been reported by Oh et al [33] and Mericam-Bourdet et al [37].

Here, at flow rates of 0.67 to 2.25 slm, the presence of plasma is seen to reduce the length of the laminar region. Similar studies [29] suggest that this shortening or contraction behaviour is attributable to two possible mechanisms. These are (1) gas heating resulting from electron collisions and (2) momentum transfer from ions to neutral gas atoms. Since it is possible that neutral gas atoms become heated upon collision with electrons thus leading to a decrease in the local density and an associated increase in the exit flow velocity. Other studies [35, 36] suggest momentum transfer from positive ions within the plasma bullet to the neutral gas atoms, thus increasing the gas fluid exit speed.

6.3.5 OES Results

Optical emission spectroscopy (OES) has the advantage of being a non-intrusive and non-perturbing procedure. Although temperature measurements, deploying OES, may be obtained from the analysis of high-resolution rotational bands in the emission spectra of suitable electronically excited diatomic molecular species present in the discharge, the most frequently utilized bands are those from the second positive system (SPS) of N_2 and the first negative system (FNS) of N_2^+ [38]. The optical emission spectrum (see figure 6.10) between 300 nm and 800 nm of the atmospheric pressure glow discharge (APGD) in high purity helium is very similar to that reported by others [39, 40]. This spectrum was obtained using the 1 mm ID capillary at a flow rate of 1.38 slm when the applied voltage was fixed at 8.0 kV_{p-p}.

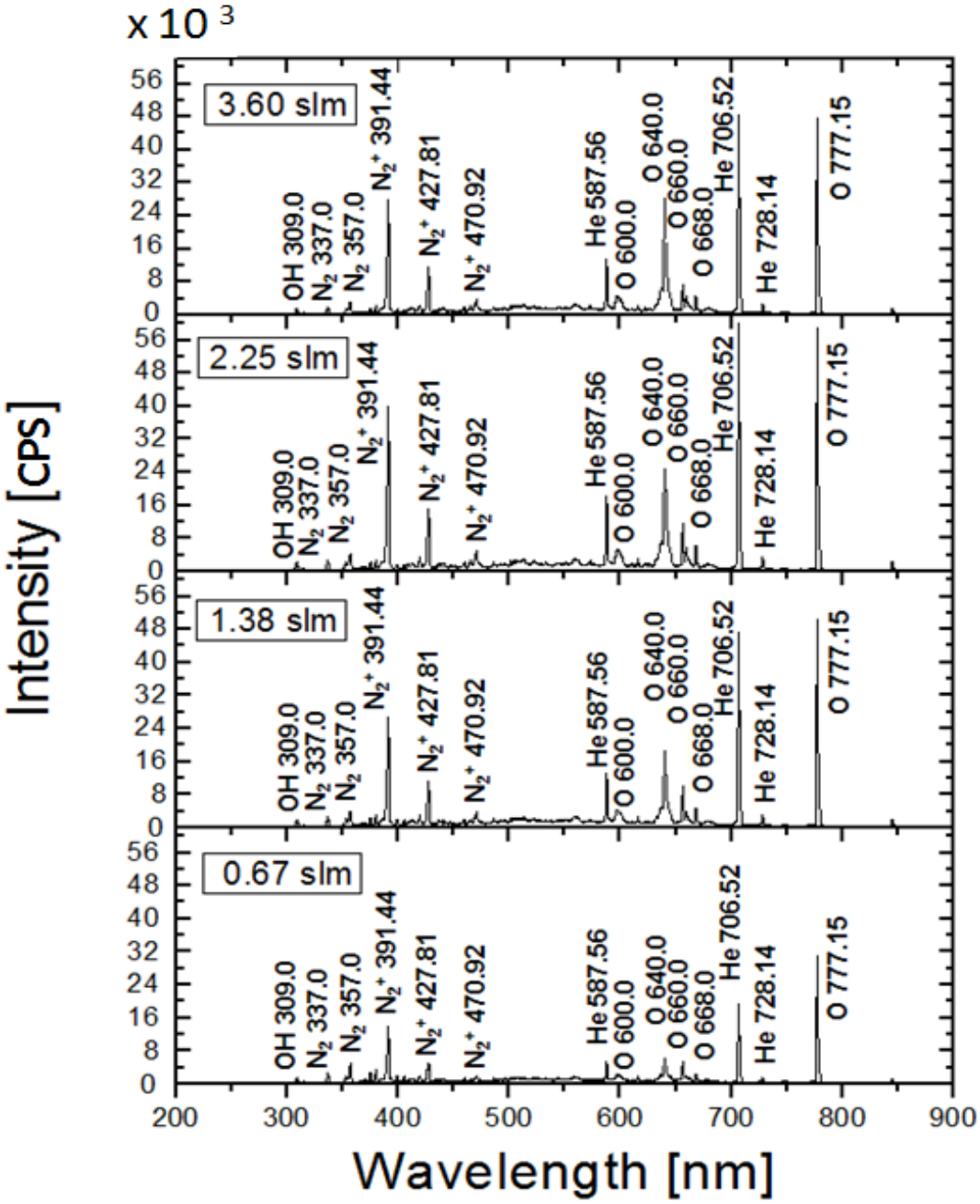

Figure 6.10: A typical emission spectrum in "pure" He. Flow rate was varied from 0.67 to 3.60 slm, keeping other parameters constant.

Figures 6.11, 6.12 and 6.13, show the influence of the flow rate, operating frequency and the applied voltage respectively on the emission intensities of the active species within the plasma.

The increase in emission lines was somewhat linear across the spectrum for figures 6.11 and 6.12. Figure 6.11 shows an increase in the emission intensity of each spectral peak as the flow rate was increased from the lowest value at 0.67 slm until it saturates at 2.25 slm.

From figure 6.12, an initial increase in emission intensity of the spectral lines is observed when frequency is increased from 10 to 20 kHz and later, a subsequent decrease as the frequency is increased further to 30 kHz. In figure 6.13, we clearly see an increase in spectral peaks as the applied voltage is varied from 5 to 8 kV. For results presented in figures 6.11, 6.12 and 6.13, we assumed laminar gas flow since the spectrum was acquired close to the capillary orifice, just before the plasma exits the nozzle. We have neglected differences in density distributions of various plasma species by taking spectral measurements in the same position when varying parameters. As suggested by Bogaerts et al [41], we expect the fluxes of plasma species to increase with increasing flow rate from 0.67 slm to 3.6 slm because a higher flow rate means a higher convection velocity and hence a large contribution of convection as transport mechanism and therefore a higher flux.

Also, an increase in applied power results in more rapid collisions of the plasma species which causes higher increases in current and hence higher spectral peaks are obtained for the plasma species. We have not discussed the relative roles of the various transport mechanisms, i.e., diffusion, migration and convection for the various plasma species in detail as they can only be explained using computational fluid models similar to that discussed in [41]. However, in all discharges emission lines from SPS N_2 ($C^3\Pi_u$ – $B^3\Pi_g$) and FNS N_2^+ ($B^3\sum_u^+$ – $X^2\sum_g^+$) bands, triplet oxygen at 777 nm ($3^5P \rightarrow 3^5S$), and the $3^3S \rightarrow 2^3P$ transition at 706.5 nm from He could be clearly identified [40]. The most intense line was observed at K = 391.4 nm for N_2^+ while fainter helium lines were observed at 587.6 nm ($3^3D \rightarrow 2^3P$).

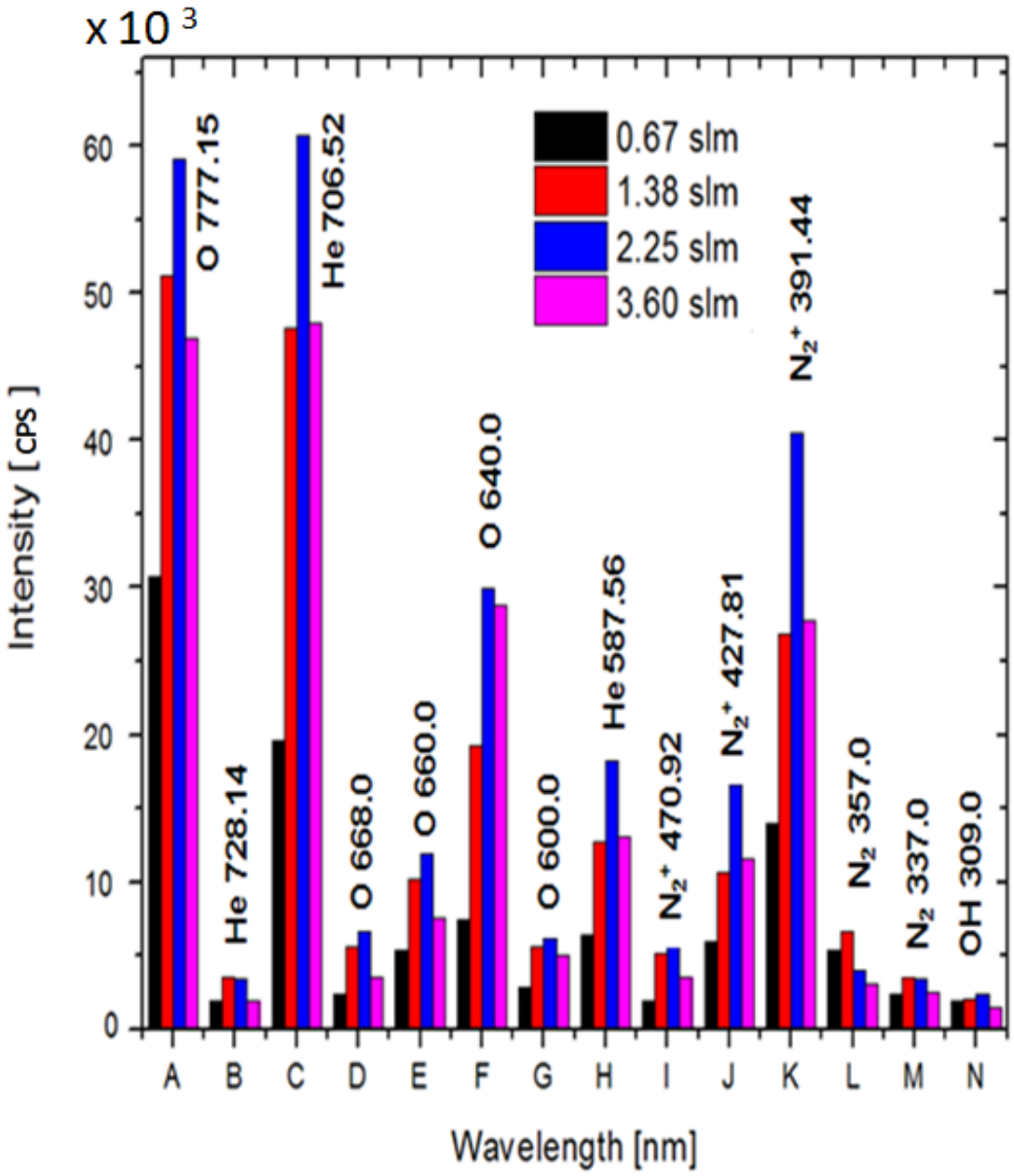

Figure 6.11: A typical emission spectrum from 300 nm to 800 nm in "pure" helium. The figure shows the influence of changes in flow rate on the emission intensities of active species within the plasma.

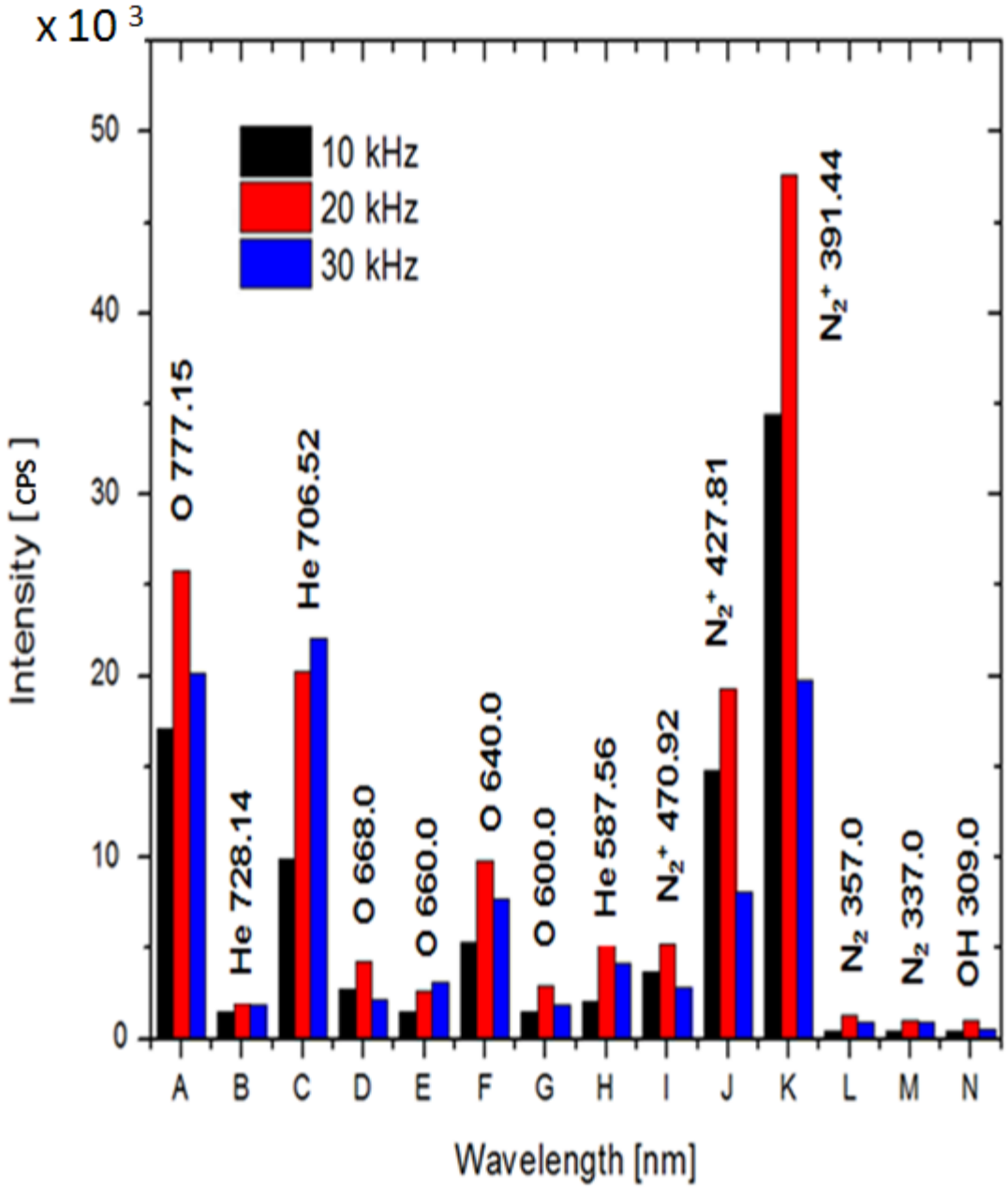

Figure 6.12: A typical emission spectrum from 300 nm to 800 nm in "pure" helium. The figure shows the influence of changes in frequency on the emission intensities of active species within the plasma.

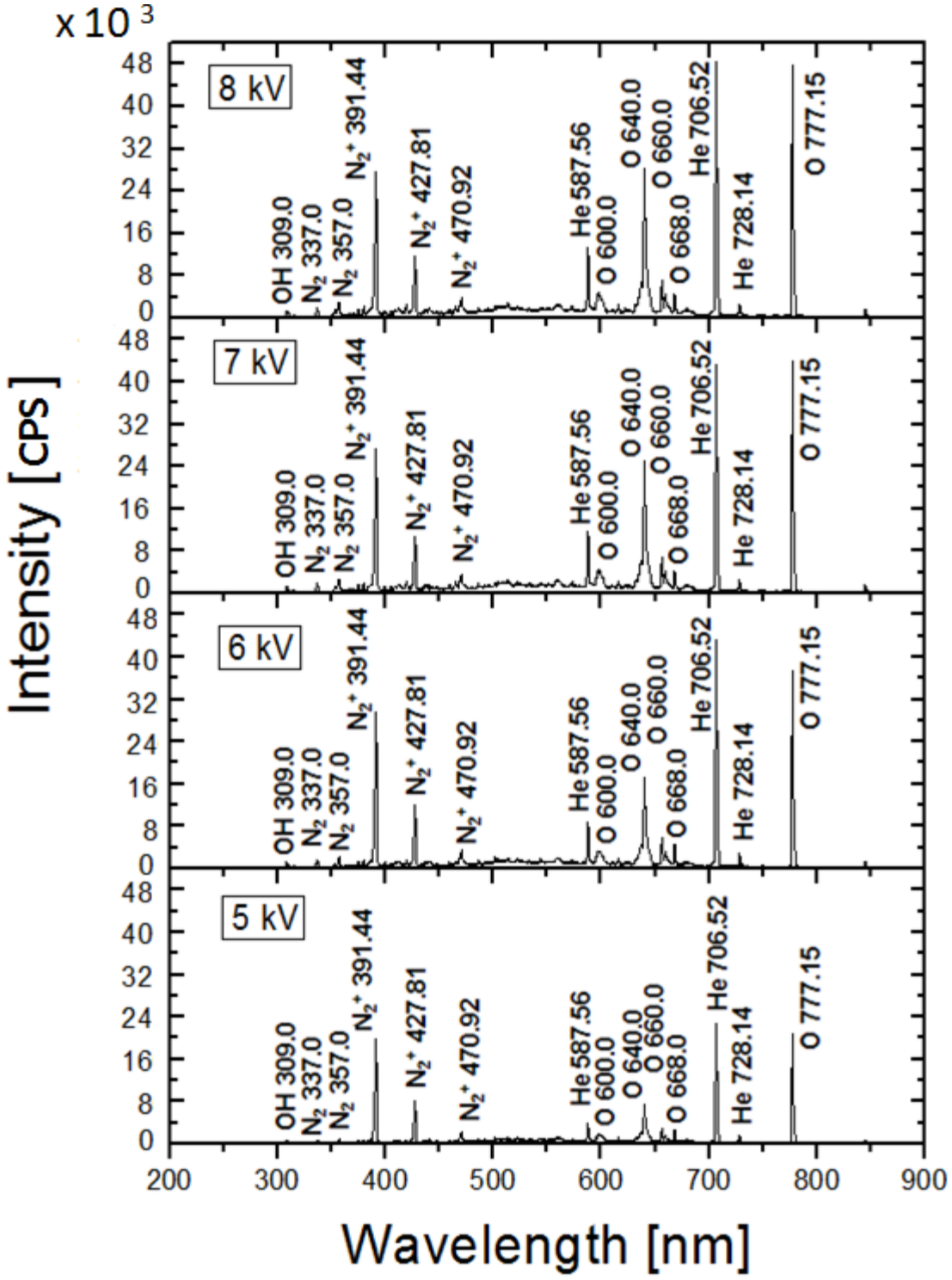

Figure 6.13: A typical emission spectrum from 300 nm to 800 nm in "pure" helium. The figure shows the influence of changes in applied voltage on the emission intensities of active species within the plasma.

Figure 6.14 shows the second positive system for N_2. The band heads are 353 and 357 nm respectively. The rotational temperature is 300 °K and the vibrational temperature is 3800 °K. The rotational and vibrational temperatures T_r and T_v of N_2 were determined by direct comparison between the experimentally measured molecular band (shown in black) of N_2 ($C^3\Pi_u \rightarrow B^3\Pi_g$, ($\Delta\nu$ = -1, at 357 nm) and the simulated (shown in red) using Specair [42]. The difference between the vibrational and rotational temperatures is indicative of significant levels of non-equilibrium state in the N_2 discharge [43].

6.3.6 Polymerisation

The mechanism of plasma polymerisation involves various interactive processes of species with each other, the surroundings and the treated sample. This complex process is not yet fully understood. However, since ions, free radicals, electrons as well as excited molecules are present in plasma, it is important to identify the dominant species that control this mechanism. Here, we have investigated how the rate of plasma polymerisation depends on the nature of the monomer gas as well as parameters such as flow rate, pressure, power, frequency, electrode gap and configuration. In general, at low flow rates, there is an abundance of reactive species so the polymerisation rate is limited only by the availability of monomer supply. However, high flow rates give rise to high levels of monomer concentration, thus the polymerisation rate depends on the residence time as a result. At intermediate flow rates, a maximum is obtained from these competing processes [44].

6.3.6.1 Polymerisation Setup

The configuration used is similar to that shown in figure 6.1. The monomer solutions used were obtained from (Sigma- Aldrich). Prior to deposition, helium gas was fed through one of the inlet PTFE tubes at a flow rate of 1.38 slm into a mixing chamber containing a pure solution of the monomer. The outlet tube containing a mixture of the monomer vapour and helium were then connected via a tee-connector anfd another flow meter to a pure helium gas supply that flows into the capillary (ID = 1mm) of the microjet. Here, we have observed the effects of changing parameters such as applied power, monomers and flow rates on the elemental composition of treated PS samples. The PS samples were placed in a glass substrate holder and directed towards the plasma plume head-on. The reactions were carried out in a fume cupboard. Monomer flow (1.38 slm), gas pressure (1.0 bar), and sample position were held constant throughtout the experiment. After each PS sample treatment, the samples were sent for XPS analysis. To minimise the effect of ageing, the samples were analysed within 2 days after removal from the vacuum chamber.

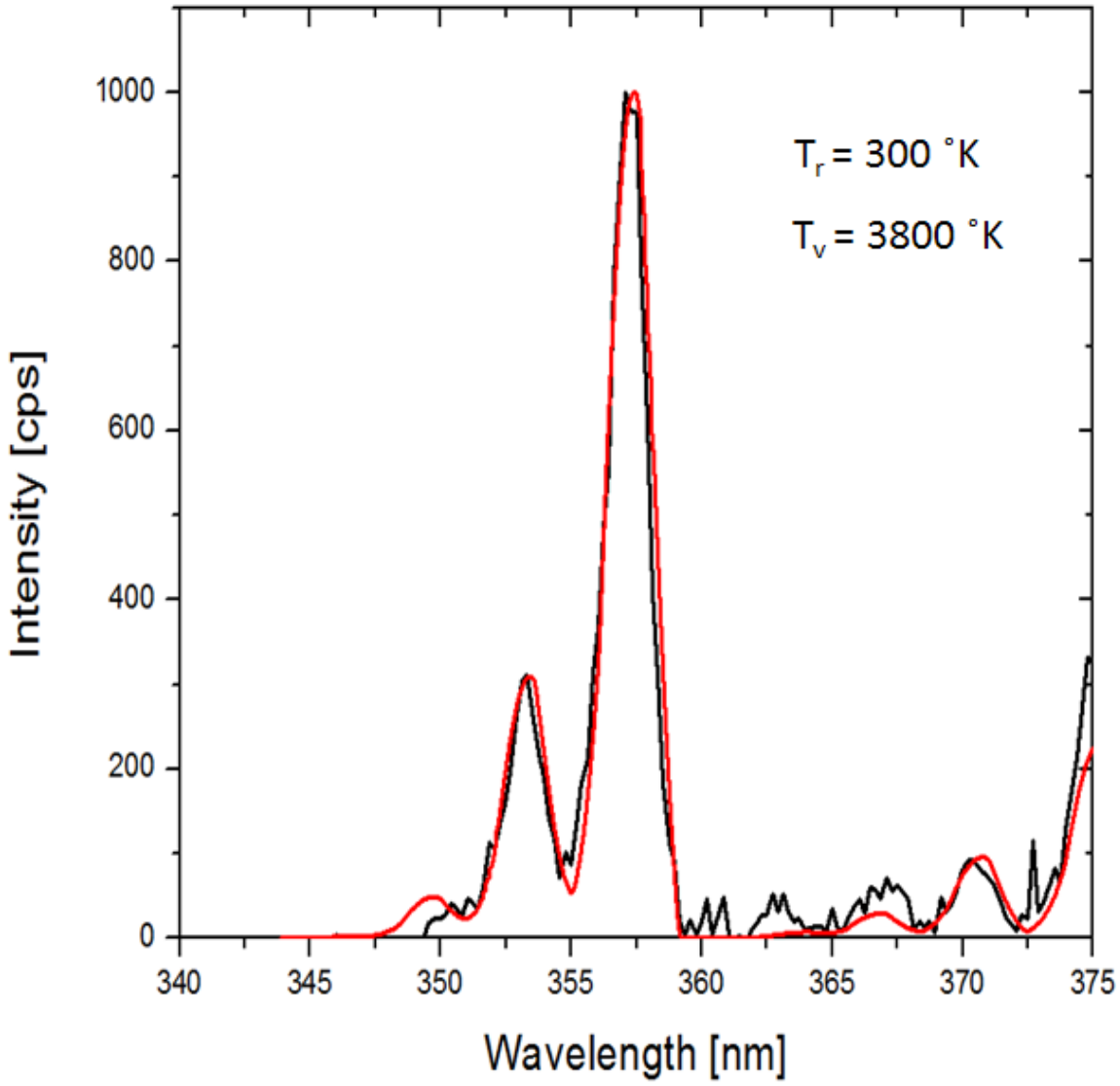

Figure 6.14: Shows the second positive system for N_2. The band heads are 353 and 357 nm respectively. The measured rotational temperature is 300 ˚K and the vibrational temperature is 3800 ˚K.

6.3.7. XPS Results

XPS analysis gives more insight into the likely mechanisms and species involved in the modification process. Figure 6.15 shows the XPS spectra results obtained for survey scans of O 1s and C 1s present in samples 1 to 6 following plasma treatment. The PS samples were exposed to plasma with the following parameters (See Table 6.1).

Table 6.1: Treatment parameters for PS samples

Sample PS	**Voltage V (kV)**	**Frequency F (kHz)**	**Helium He %**	**Allylamine $C_3H_5NH_2$%**
1	7.0	30	100	0
2	8.0	30	100	0
3	7.0	30	0	100
4	8.0	30	0	100
5	7.0	30	Mixture	
6	8.0	30	Mixture	

Photoemission of the 1s level is particularly important as a probe of the electronic structure of these materials since the 1s XPS peak is expected to possess the simplest shape due to the absence of spin–orbit splitting and the fact that the exchange splitting is expected to be a minimum due to the small overlap between 1s and unfilled d orbitals [45].

XPS has been utilised to study treated PS surface at distance of 2 cm from the plume and as a function of applied power. From figures 6.15 a to f, the peaks corresponding to C 1s and O 1s

have been identified in each case for samples 1 to 6. We have also shown the effects of increases in applied power from 7 to 8 $kV_{p-p.}$ This can be seen when comparing figures 6.15 a & b, c & d, and e and f respectively. Samples 2, 4 and 6 were treated with higher power when the voltage applied was increased from 7 to 8 kV_{p-p} while samples 1, 3 and 5 were treated with a slightly lower applied voltage of 7 kV_{p-p}.

The untreated PS usually contains approximately 99% carbon and 1% oxygen [46, 47]. Samples were treated with a 1 mm capillary diameter (ID) and at a nozzle – sample distance of 2 cm for 20 seconds. Following treatment of the PS surface, the surface had incorporated more oxygen of up to ~10 to 20 %. Additionally, the atomic surface concentration of carbon decreased by ~10 to 20 % (See figure 6.15 a – f). We also clearly see the development of a nitrogen peak with Binding energy of ~ 403 eV in figures 6.15 (c to f). This peak is due to the presence of the NH_2 functional group in allylamine compound, and is seen to increase with increasing applied power. Previous studies in low pressure plasma systems have shown that the incorporation of oxygen into PS mostly occurs in the vacuum chamber from impurities such as water vapour, whereas incorporation due to exposure to the atmosphere is much smaller [46]. In addition, the spectra are shifted in energy to align the 1s peaks and in some cases the broadening effect is observed for the main peaks. Similar findings have been reported previously [48 – 50].

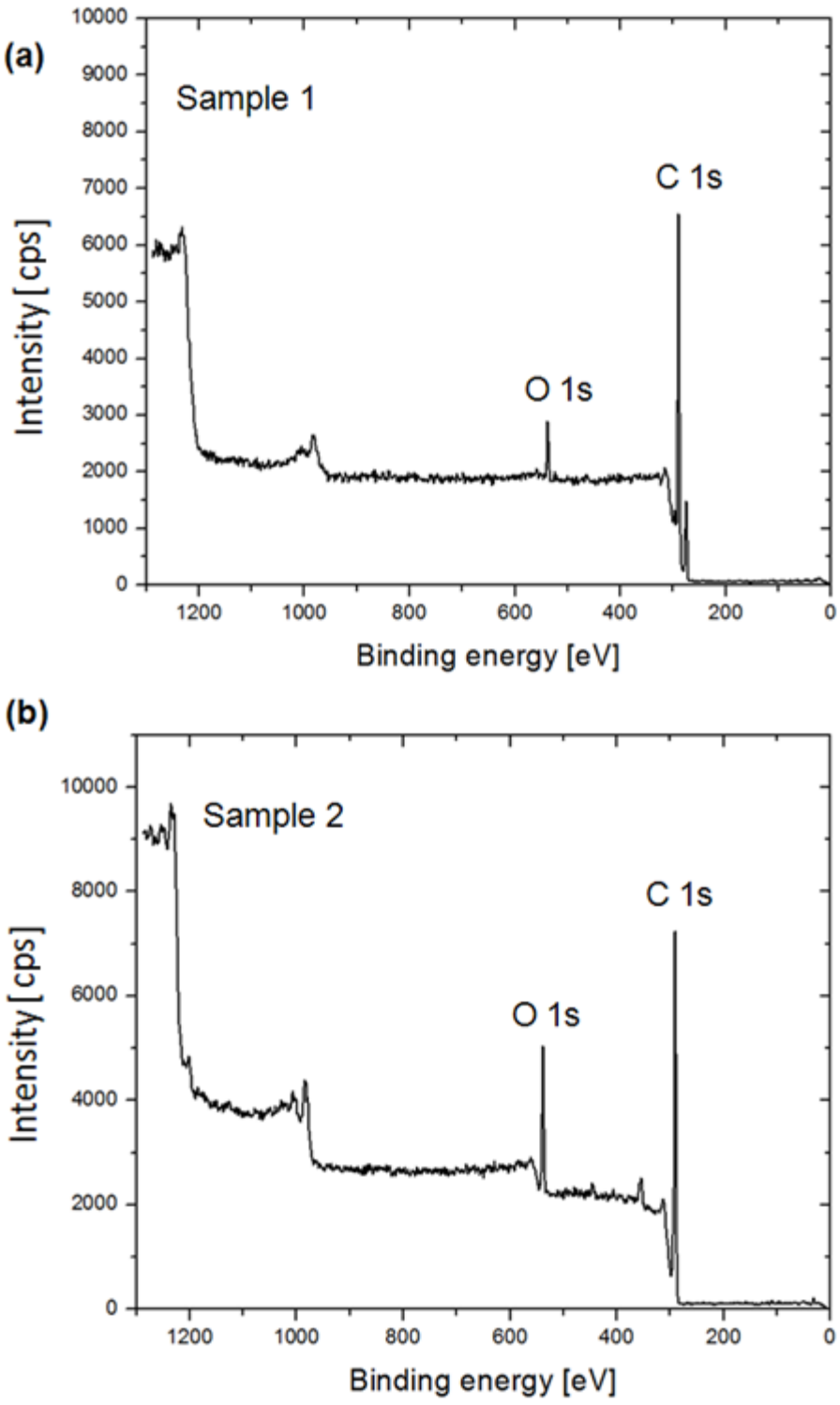

Figure 6.15: Survey XPS spectra of the treated region of PS surface **(a)** with pure helium plasma at 7 kV_{p-p} (sample 1) **(b)** with pure helium plasma at 8 kV_{p-p} (sample 2)

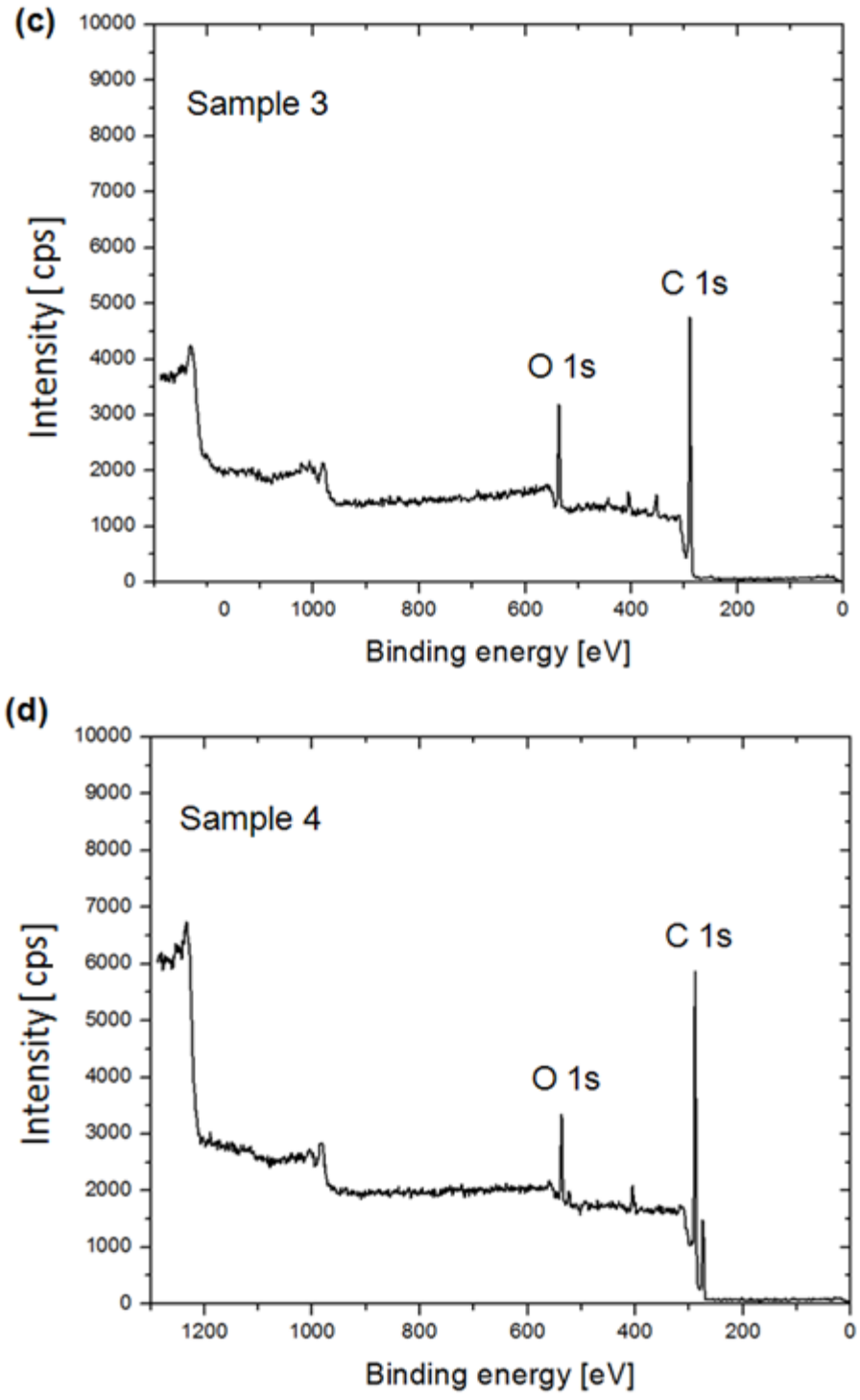

Figure 6.15: Survey XPS spectra of the treated region of PS surface **(c)** with pure allylamine discharge at 7 kV_{p-p} (sample 3) (**d)** with pure allylamine discharge at 8 kV_{p-p} (sample 4)

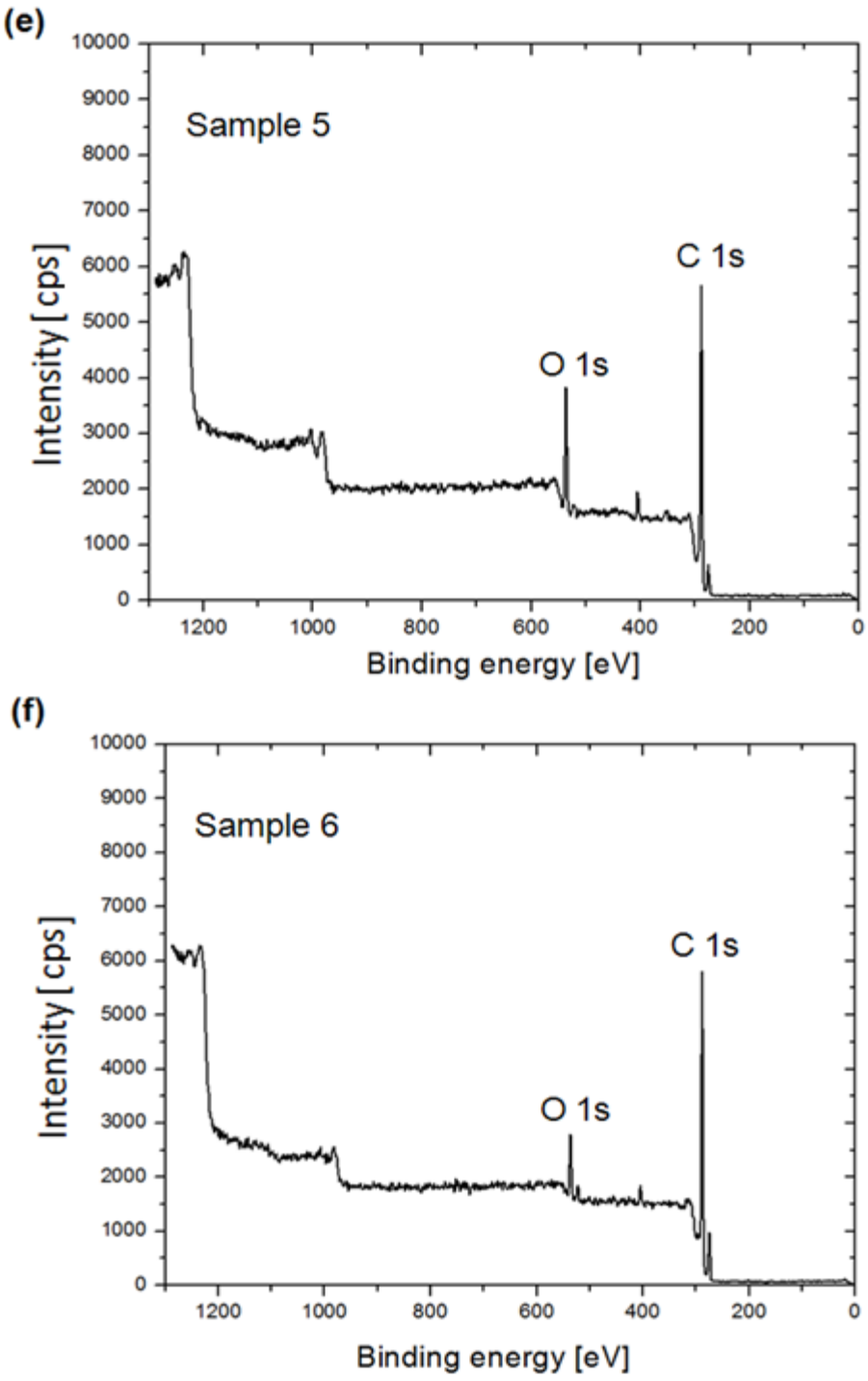

Figure 6.15: Survey XPS spectra of the treated region of PS surface **(e)** with a mixture of He and allylamine at 7 kV_{p-p} (sample 5) (**f)** with a mixture of He and allylamine at 8 kV_{p-p} (sample 6)

To provide more accurate quantitative information from the XPS spectra, we have obtained high resolution XPS spectra (figures 6.16 a to f) for C 1s and O 1s detected in samples 1 to 4 and O 1s for samples 5 and 6. Figures 6.17 a and b show the influence of x-ray exposure for a period of 24 hours. Here, we have observed that when the samples were left in the spectrometer for a day before obtaining the XPS spectra, the emission intensities for the C 1s and O 1s appear to change significantly. The reason for these changes in peak intensities and the formation of new ones is not well understood and has to be investigated further. However, we conjecture that these changes are probably caused by exposure to surrounding x-rays since the possibility of changes due to ageing in vacuum is highly unlikely over this short period of time (i.e. 24 hours).

We think that x-rays may play a significant role in the growth of new peaks as well as in the modification of existing peaks. This finding may become significant for biomedical applications, especially for cell attachment applications and others application that require the immobilization of chemical species such as DNA or proteins onto plasma treated surfaces.

Advances in biomaterials, stem cells and tissue engineering have created unique opportunities to fabricate tissues in the laboratory from combinations of engineered extracellular matrices (scaffolds) and cells. Among the major challenges facing tissue engineering is the need for the development of complex and biomechanical functionality in laboratory- grown tissues for transplants. Here, we have treated six different 3-D scaffolds with the microjet at a voltage of 8 kV and a frequency of 30 kHz.

The scaffolds were exposed to plasma containing a mixture of He and allylamine. We have investigated the influence of different treatment times 10, 20 and 40 seconds on the percentage composition of carbon and nitrogen in the treated scaffold using XPS and plotted the results against the depth profile as shown in figures 6.18 a and b.

We have also investigated the effects of different nozzle-subtrate distances D = 1, 1.5 and 2 cm respectively. The results are also shown in figure 6.18 a and b. In general, the percentage composition of carbon seems to change by ~ 5 % for depths of up to 7 mm while the nitrogen percentage composition appears to initially increase to ~ 2 % at a depth of 1 mm and then decreases to ~ 0.75% at D = 2 mm before eventually falling to ~ 0 % as the depth increases beyond 3 mm..

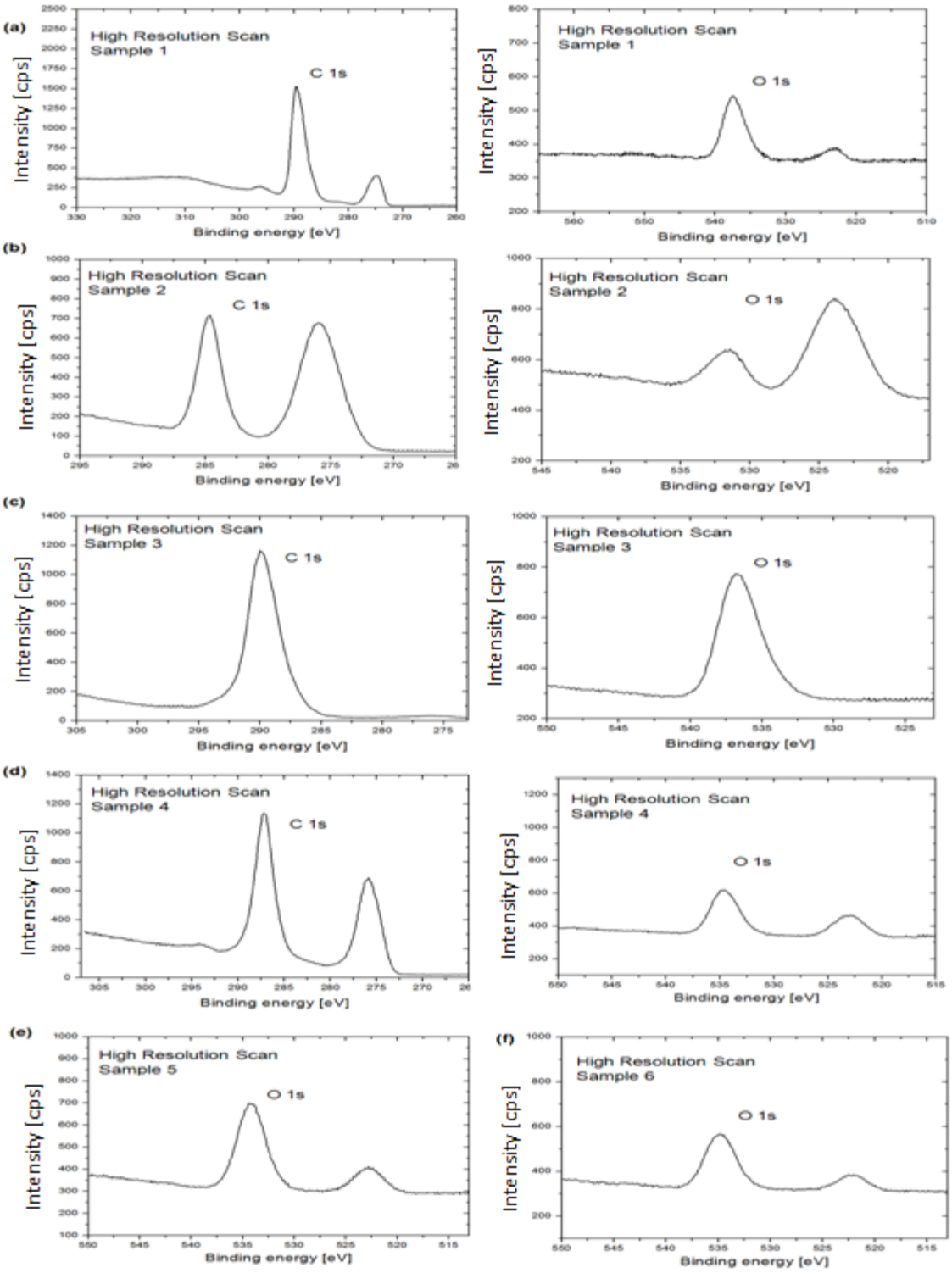

Figure 6.16: High resolution XPS spectrum of the treated region of PS surface **(a)** C 1s and O1s for sample 1, **(b)** C 1s and O1s for sample 2 , **(c)** C 1s and O1s for sample 3, **(d)** C 1s and O1s for sample 4 **(e)** O1s for sample 5 and **(f)** O1s for sample 6.

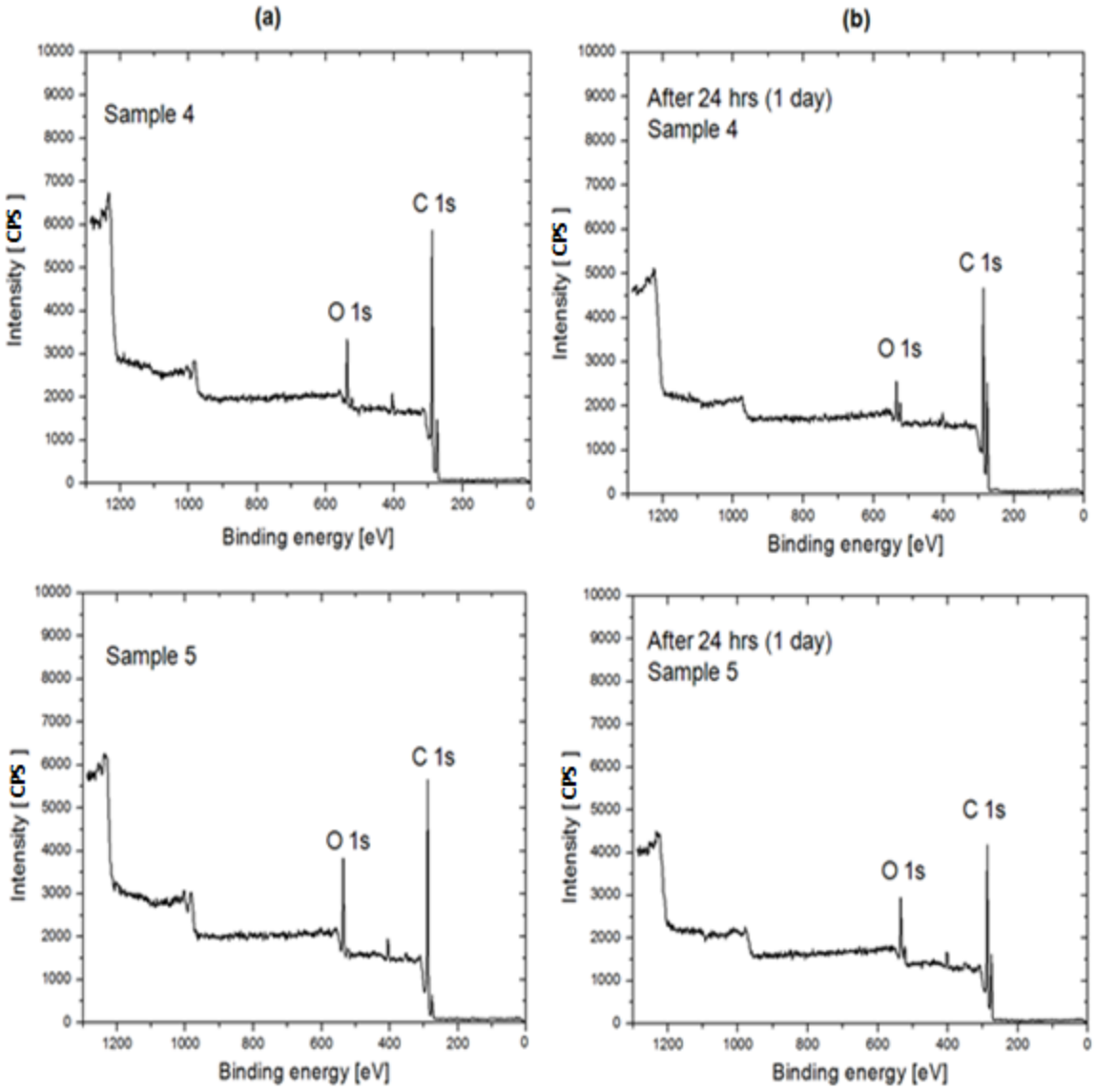

Figure 6.17: Survey XPS spectra of the treated region of PS surface for samples 4 and 5 **(a)** for immediate scans **(b)** after 24 hours. Growth of new peaks and changes in existing peaks observed probably due to exposure to x-rays for longer times.

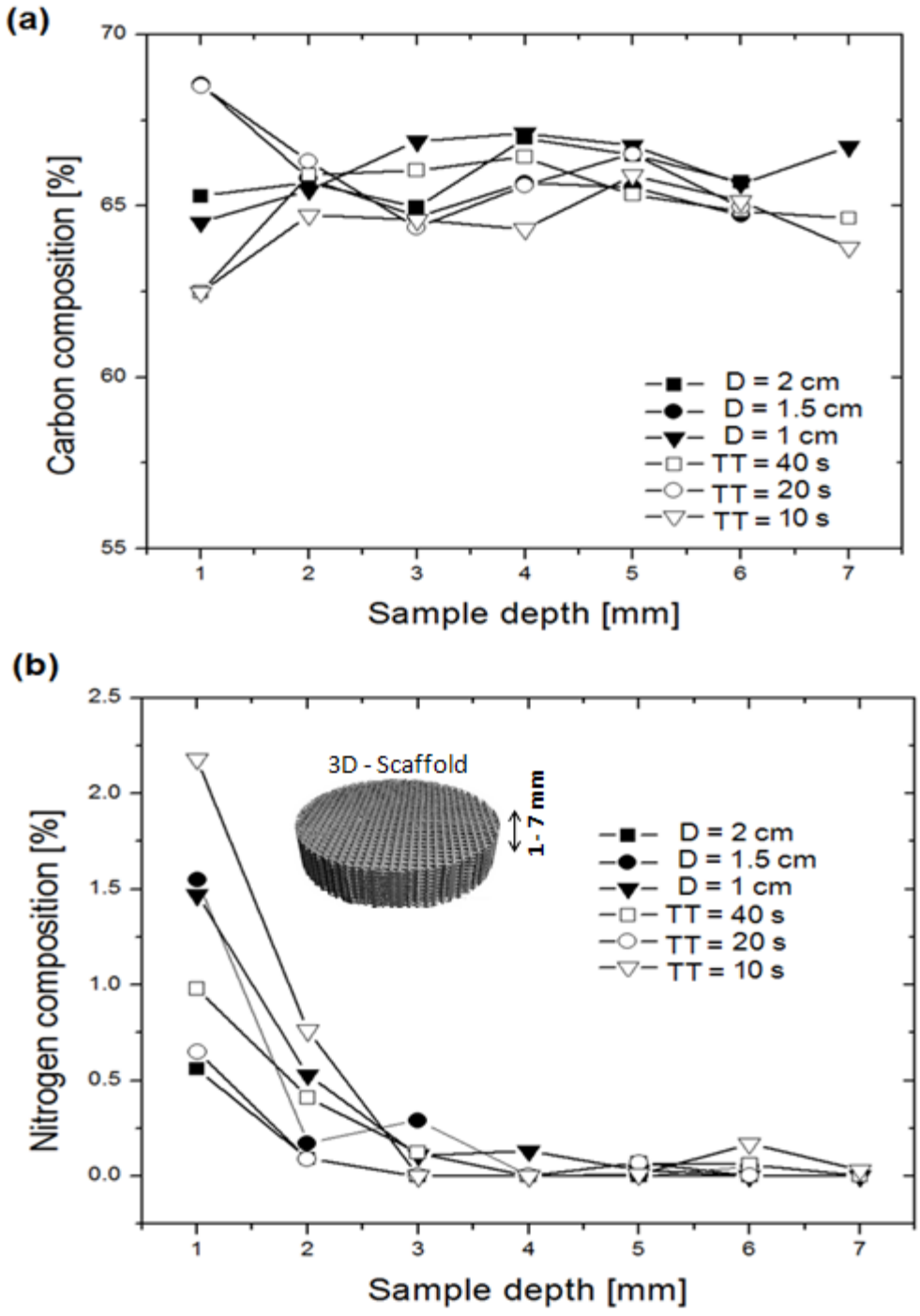

Figure 6.18: Shows the XPS depth profile analysis for treated 3-D Scaffold for different treatment times (TTs) and different nozzle-sample distances D (cm). **(a)** Carbon composition (%) **(b)** Nitrogen composition (%)

6.4 CONCLUSIONS

We have studied the behaviour of an atmospheric pressure microjet using 2D optical imaging, Schlieren photography and basic standard electrical (current-voltage) measurements. We have investigated two different regions observed i.e. laminar and turbulent as well as the interaction of the visible plasma plume with a polystyrene substrate. We have shown that the lengths of the laminar and turbulent regions increases or decreases depending on operating parameters i.e. frequency, voltage and flow rate. The OES results obtained show an increase in spectral peaks with increasing flow rate from 0.67 to 3.6 slm, since we expect the fluxes of plasma species to increase with increasing flowrate resulting in a higher convection velocity and hence a larger contribution of convection as the transport mechanism. We have also shown that an increase in applied power causes higher increases in the current and hence higher spectral peaks due to more rapid collisions of the plasma species contained within the plasma We have used XPS to probe the electronic structure of PS surface at a distance of 2 cm from the plume. The peaks corresponding to O 1s and C 1s in the six samples indentified are seen to increase with increasing applied power from 7 to 8 kV_{p-p} .The untreated PS surface which usually contains 99 % carbon and 1 % oxygen showed an increase of ~ 10 to 20 % in oxygen concentration and a reduction of ~ 10 to 20 % in carbon concentration following treatment for 20 s. In addition, the development of nitrogen peaks with binding energy ~ 403 eV due to the presence of NH_2 functional group in the allylamine compound are also seen, and these appear to increase with increasing applied power. Other factors such as long exposures to x-rays can also have a significant effect but more experiments are required to verify this.

References

1. S.-J. Park, K.F. Chen, S.H. Sung, J. SID 13 (2005) 949.

2. K.H. Becker, K.H. Schoenbach, J.G. Eden, J. Phys. D: Appl. Phys. 39 (2006) R55.

3. J.C.T. Eijkel, H. Stoeri, A. Manz,An atmospheric pressure dc glow discharge on a microchip and 1st application as a molecular emission detector, J. Anal. At. Spectrom. 15 (2000) 297–300.

4. F.G. Bessoth, O.P. Naji, J.C.T. Eijkel, A. Manz, Towards an on-chip gas chromatograph: the development of a gas injector and a dc plasma emission detector, J. Anal. At. Spectrom. 17 (2002) 794–799.

5. T. Cserfalvi, P. Mezei, P. Apai, Emission studies on a glow discharge in atmospheric pressure air using water as a cathode, J. Phys. D 26 (1993) 2184–2188.

6. P. Mezei, T. Cserfalvi, M. Janossy, Pressure dependence of the atmospheric electrolyte cathode glow discharge spectrum, J. Anal. At. Spectrom. 12 (1997) 1203–1208.

7. W.C. Davis, R.K. Marcus, An atmospheric pressure glow discharge optical emission source for the direct sampling of liquid media, J. Anal. At. Spectrom. 16 (2001) 931–937.

8. R.K. Marcus,W.C. Davis, An atmospheric pressure glow discharge optical emission source for the direct sampling of liquid media, Anal. Chem. 73 (2001) 2903–2910.

9. Y. Yin, J. Messier, J.A. Hopwood, Miniaturization of inductively coupled plasma sources, IEEE Trans. Plasma. Sci. 27 (1999) 1516–1524.

10. S.D. Anghel, T. Frentiu, E.A. Cordos, A. Simon, A. Popescu, Atmospheric pressure capacitively coupled plasma source for the direct analysis of nonconductive solid samples, J. Anal. At. Spectrom. 14 (1999) 541–545.

11. A. Bass, C. Chevalier, M.W. Blades, A capacitively coupled microplasma (CC mu P) formed in a channel in a quartz wafer, J. Anal. At. Spectrom. 16 (2001) 919–921.

12. A.M. Bilgic, E. Voges, U. Engel, J.A.C. Broekaert, A low-power 2.45 GHz microwave induced helium plasma source at atmospheric pressure based on microstrip technology, J. Anal. At. Spectrom. 15 (2000) 579–580.

13. J. Hopwood, F. Iza, Ultrahigh frequency microplasmas from 1 pascal to 1 atmosphere, J. Anal. At. Spectrom. 19 (2004) 1145–1150.

14. M. Miclea, K. Kunze, J. Franzke, K. Niemax, Plasmas for lab-on-the-chip applications, Spectrochim. Acta Part B 57 (2002) 1585–1592.

15. J. Franzke, K. Kunze, M. Miclea, K. Niemax, Microplasmas for analytical spectrometry, J. Anal. At. Spectrom. 18 (2003) 802–807.

16. C. Penache, M. Miclea, A. Bräuning-Demian, O. Hohn, S. Schössler, T. Jahnke, K. Niemax, H. Schmidt-Böcking, Characterization of a highpressure microdischarge using diode laser atomic absorption spectroscopy, Plasma Sources Sci. Technol. 11 (2002) 476–483.

17. R.J. Skelton Jr., H.-C.K. Chang, P.B. Farnsworth, K.E. Markides, M.L. Lee, Radio-frequency plasma detector for sulfur selective capillary gaschromatographic analysis of fossil-fuels, Anal. Chem. 61 (1989) 2292–2298.

18. J.A.C. Broekaert, The development of microplasmas for spectrochemical analysis, Anal. BioAnal. Chem. 374 (2002) 182–187.

19. J. Franzke, K. Kunze, M. Miclea, K. Niemax, Microplasmas for analytical spectrometry, J. Anal. At. Spectrom. 18 (2003) 802–807.

20. J.I. Baumbach, M. Westhoff, Ion mobility spectrometry to detect lung cancer and airway infections, Spectrosc. Eur. 18 (2006) 22–27.

21. W. Vautz, D. Zimmermann, M. Hartmann, J.I. Baumbach, J. Nolte, J. Jung, Ion mobility spectrometry for food quality and safety, Food Addit. Contam. 23 (11) (2006) 1064–1073.

22. W. Vautz, J.I. Baumbach, J. Jung, Beer fermentation control using ion mobility spectrometry, J. Inst. Brew. 112 (2006) 157–164.

23. Szili E J, Al-Baraineh S A, Bryant P M, Short R D, Bradley J W and Steele D A 2011, Plasma Process. Polym, Vol 8, pp 38 – 50

24. Oh J-S, Bradley J W, Doherty K G, Sheridan C M, Williams R L, Bowfield A, Unsworth P and Weightman P 2010 Proc. AVS 57th Int. Sym. and Exhibition (Albaquerque, NM, 17 – 22 October 2010) p 33

25. Fridman G, Friedman G, Gustol A, Shekhter A B, Vasilets V N and Fridman A 2008. Plasma Process. Polym. Vol 5, pp 503 - 33

26. Lee K, Paek K-H, Ju W-T and Lee Y 2006 J. Microbiol. 44, pp 269 – 275

27. Okazaki S, Kogoma M, Uehara M and Kimara Y 1993 *J. Phys.D: Appl. Phys.* **21** 889

28. O. T. Olabanji and J.W. Bradley; The development and analysis of plasma microfluidic devices, Surface and coatings technology, 2011

29. Merzkirch W 1987; Flow Visualization (New York: Academic) Chapter 3

30. Stoffels E, Aranda-Gonzalvo Y, Whitmore T D, Seymour D L and Rees J A 2007; Plasma Sources Sc. Technology, Vol 16 pp 549

31. Urabe K, Morita T, Tachibana K and Ganguly B N 2010. J. Phys D: Appl. Phys.; Vol 43 095201

32. Teschke M, Kedzierski J, Finantu-Dinu E G, Korzec D and Engemann J 2005; IEEE Trans. Plasma Sci, Vol 33, pp 310

33. Jun-Seok Oh, Olumuyiwa T Olabanji, Craig Hale, Raffaello Mariani, Konstantinos Kontis and James W Bradley (2011); Imaging gas and plasma interactions in the surface-chemical modification of polymers using micro-plasma jets, Journal of Phys. D: Appl. Phys., Vol 44, 155206

34. Tachibana K 2006. IEEE Trans. Vol 1, pp 145-55

35. Karakas E, Koklu M and Laroussi M 2010 J. Phys. D. Appl. Phys. Vol 43 155202

36. J.P Holman *Heat transfer*, McGraw-Hill, 2002, p.207

37. Mericam-Bourdet N, Laroussi M, Begum A and Karakas E 2009. J Phys D: Appl. Phys 42 055207.

38. N. K. Bibinov, A. A. Fateev, K. Wiesemann, Plasma Sources, Sci. Technol. 2001, 10, 579.

39. F. Massines, P. Se´gur, N. Gherardi, C. Khamphan, A. Ricard, Surf. Coatings Technol. 2003, 174–175, 8.

40. V. Poenariu, M. R. Wertheimer, R. Bartnikas, Plasma Process. Polym. 2006, 3, 17

41. A. Bogaerts, A. Okhrimovskyy, R. Gijbels, J. Anal. At. Spectrom. 2002, 17, 1076.

42. Harling A M, Glover D J, Whitehead J C and Zhang K 2008. Environ. Sci. Technol. 42 4546

43. X Tu, H J Gallon, J C Whitehead, J. Phys. D: Appl. Phys. 44 (2011) 482003 (4pp)

44. T.A. Carlson, J.C. Carver, G.A. Vernon, J. Chem. Phys. 62 (1975) 932.

45. M. Dhayal, M.R. Alexander, J.W. Bradley, Appl. Surf. Sci. 252 (2006) 7957.

46. K. Wende, K. Schröder, U. Lindequist, A. Ohl, Plasma Process. Polym. 3 (2006)

47. R. Pollak, A.L. Ley, F.R. MvFeely, S.P. Kowalczyk, D.A. Shirley, J. Electron Spectrosc. Relat. Phenom. 3 (1974) 381.

48. D. Pines, Rev. Mod. Phys. 28 (1956) 184.

49. S.A. Abo-Namous, P. Andrews, Phys. Rev. B 20 (1979) 2335

50. M. Shen, A. T. Bell, ACS Symposium Series; American Chemical Society: Washington, DC, 1979

CHAPTER SEVEN

7.0 Side-on surface modification of polystyrene (PS) with a microplasma jet

Abstract

An atmospheric-pressure microplasma jet operating in helium gas has been used in a side-on configuration to modify locally the surface energy of polystyrene (PS). The plasma plume and gas outflow emanating from the capillary-type discharge (8 kV_{p-p} at 30 kHz excitation) were directed parallel to and just above the sample surface, rather than head-on as in conventional treatment.

Schlieren photography has been used to identify regions of laminar and turbulent flow in the exiting gas stream and the nature of their interaction with the substrate surface. Correlation of these observations with spatially-resolved water contact angle (WCA) measurements of the treated polystyrene (PS), show clearly that substantial reductions in WCA (~ 50° to 60°) occur in downstream regions where the turbulent gas mixed with air impinges the surface. In contrast, only small changes in WCA occur (~10° to 20°) in regions closer to the exit orifice where the helium (He) flow is still laminar across the surface. Little or no treatment is observed for distances greater than 5 cm from the source. In addition, low levels of treatment were observed in the regions where the visible plasma glow of the jet is adjacent and parallel to the surface. The results indicate that excited air species (either mixed or entrained in the He gas flow) which exist only in regions of turbulence are the main agent causing surface covalent bond breaking leading to surface modification.

7.1. Introduction

In conjunction with technological development, fundamental studies have been conducted to measure the plasma parameters and understand better the physical and chemical processes occurring in the emerging discharge plasma plume, including passive optical emission spectroscopy [1-3], 2-D optical imaging [4, 5], active laser absorption spectroscopy (LAS) [6], laser induced fluorescence (LIF) and two-photon absorption laser induced fluorescence techniques spectroscopy (TALIF) [7], and molecular beam mass spectrometry [8].

Here we are interested in using the microplasma jet for the surface modification of polystyrene and in particular investigating how the nature of the neutral gas as it emerges from the capillary (and mixes with the ambient air) affects the level and distribution of treatment. To do this we use Schlieren photograph to identify laminar and turbulent regions and their interaction with the substrate and correlate this to spatially resolved water contact angles measurements of surface modification.

A number of recent studies using plasma micro-jets for the surface modification of polymerics have used systems in which the emerging plume impinges directly the substrate head-on [5, 9]. The areas of treatment (identified by changes in surface energy or chemistry) vary in size from a few mm across [10, 11], up to 10's of μm [12] depending on substrate – orifice distance, excitation voltages, source design and gas flow rates [13].

Since the gas which comprises a mixture of excited neutrals and possibly charged particles flows directly on to the substrate, the gas stream is always turbulent at the point of interaction. In addition to these excited species UV and VUV photons from the original source and visible column can act directly along the helium channel [14] and act on upon the surface. Hence it is difficult to separate the role of different species (i.e plasma charged and metastable and secondary excited air species) in causing surface modification. It is also reported that head-on treatment can be accompanied by some surface damage (formation of holes) [15]. Direct plasma treatment with a similar cold plasma device has shown roughening in the surface of polymeric material over remote treatment [16]. Here by placing the micro-jet side-on to the substrate we can observe how different flow regions of the jet affect the sample, allowing individual effects to be seen. In addition, this configuration may prove an efficient way of treating samples with less surface damage.

7.2. Experimental Section

7.2.1 The microplasma jet

The plasma source (shown in figure 7.1), similar to that described in [5, 8], operated as a dielectric barrier discharge, and comprised of a quartz capillary tube of 1mm internal diameter attached to two copper ring electrodes each of length 1 cm and separated at a distance of 1.5 cm. One of the rings was 1 cm from the exit orifice of the capillary. The discharge was operated in helium gas and the flow rate of gas through the capillary was controlled through adjustment of a valve connected to a rotameter gauge (Omega Engineering Ltd). In this study, three different gas flow rates were used, 0.67, 3.6 and 5.4 slm corresponding to exit gas flow

velocities of 14, 77 and 115 ms^{-1} respectively. These speeds were calculated assuming a uniform flow across the capillary.

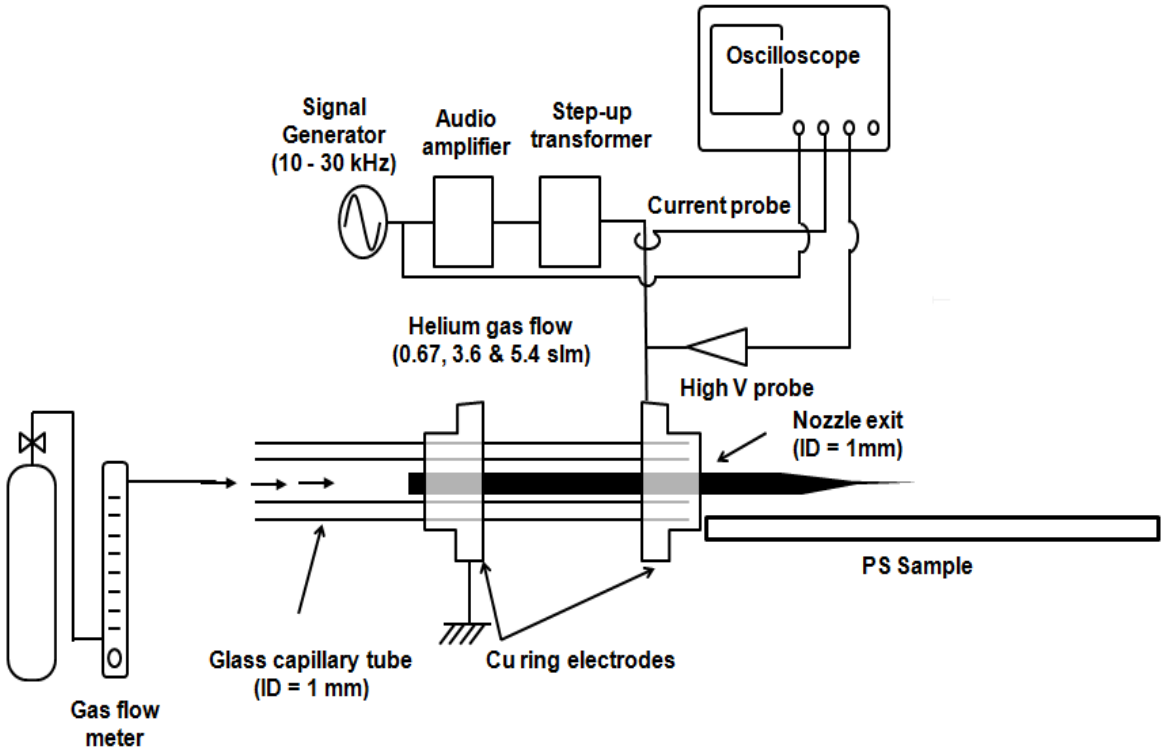

Figure 7.1: Schematic of the present apparatus (side-on)

A sinusoidal voltage of 8 kV_{p-p} (from a home-made power supply) was applied to the copper ring electrode closest to the exit orifice at a fixed frequency of 30 kHz. The other electrode was electrically grounded. The capillary source was orientated horizontally and aligned with the substrate plate holding rectangular PS samples with the centre of the capillary lying 3 mm above the surface, see figures 7.1 and 7.2.

After cleaning the PS samples as previously described, they were then introduced side-on to the plasma plume for 2 minutes. After treatment, the water contact angle (WCA) was measured on each sample at positions along the line-of-sight of the jet at 2.5 mm spacing.

For courser 2-D scans of the post-treated samples, WCA measurements were made at 0.5 cm intervals along the direction of plasma jet and at 2 mm intervals radially on either side of the centreline. This gave in total 112 measurement points. In this way, the spatial distribution and degree of treatment could be mapped out through observation of the change in WCA of the usually hydrophobic PS. The untreated PS had a WCA of 89°.

7.3 Results and Discussions

Figures 7.2 a, b and c show schlieren images of the flow field for the three different flow rates, 0.67, 3.6 and 5.4 slm with the plasma discharge struck. For the three cases, on exit from the orifice, the He flow is initially laminar but transforms to turbulent flow further downstream. The lengths of the laminar region (point where turbulence sets in) varied markedly with gas flow. From 0.67 to 3.6 slm the laminar region increases in length, from 0.5 cm to 2.9 cm, but reduces to 2 cm at 5.4 slm.

This behaviour of variation in length has been reported previously in [5]. For laminar flows, the viscous forces are dominant, and this regime is characterised by smooth and constant fluid motion, while for turbulent flows, inertial forces are dominant, characterised by chaotic vortices, eddies and other flow instabilities [17]. Using the exit gas velocities, the Reynolds number (Re) can be estimated using the expression $R_e = V L/\nu$, where V is to the mean fluid

velocity, L the minimum system scale length (1mm of the orifice diameter) and ν the kinematic viscosity of the fluid (1.22×10^{-4} for helium and 1.57×10^{-5} m^2s^{-1} for air, both at 300 K). Considering only He flow the R_e values at the orifice are ~ 115, 630 and 940, indicating laminar flow [4, 17]. As the jet expands the system length L increases and R_e reaches values crossing the threshold for turbulence ($R_e > 4000$). The diameter of the gas stream in the laminar flow region is < 2 mm and from inspection of in figure 7.2 it is clear that the laminar region flows across the substrate with little interaction and no surface turbulence.

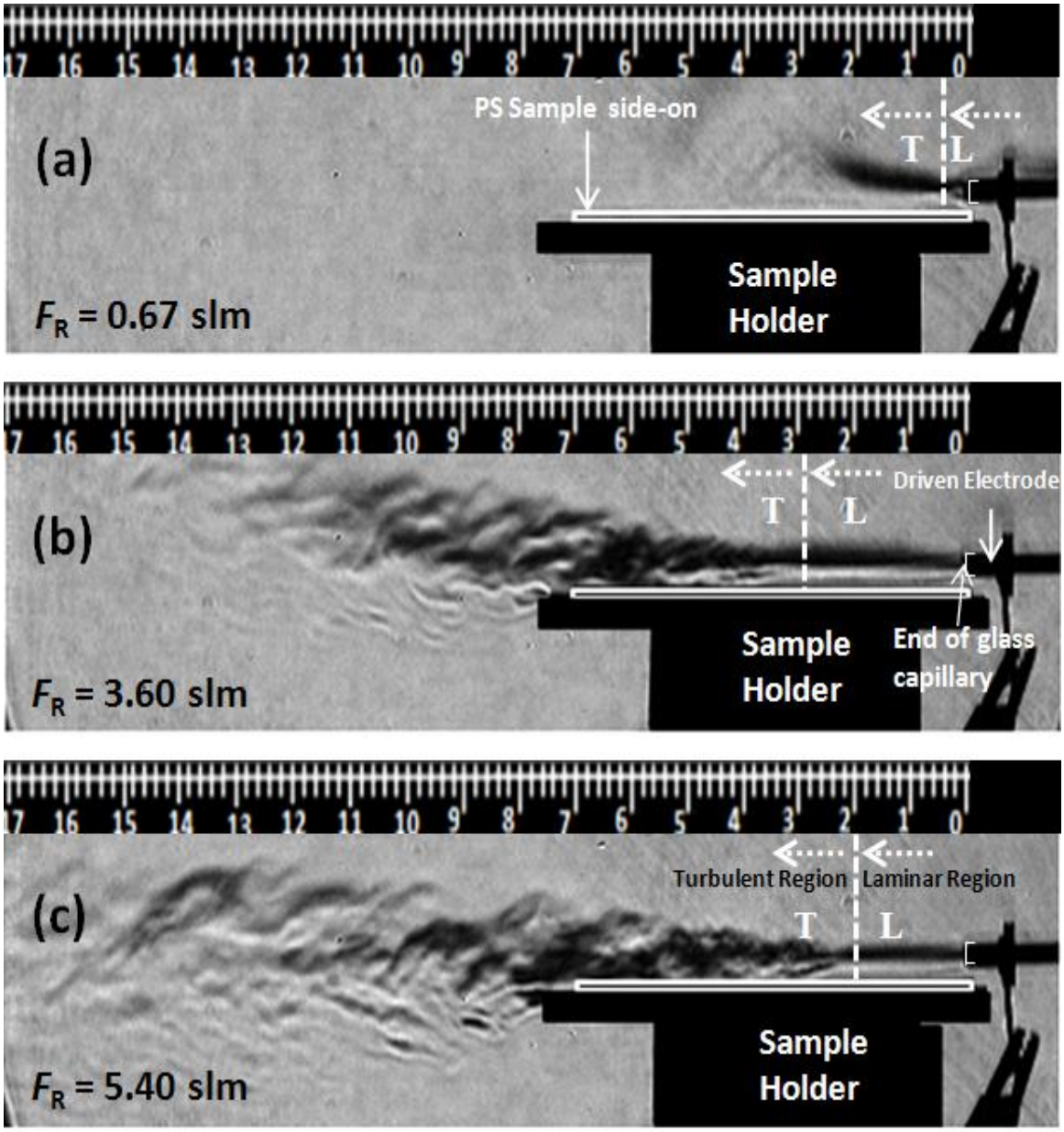

Figure 7.2: Schlieren photographic images showing variations in the lengths of the laminar and turbulent regions at three different flow rates of 0.67, 3.6 and 5.4 slm when at a fixed voltage V = 8 $kV_{p\text{-}p}$. The PS samples were positioned 3 mm below the visible plasma plume.

As well as fast streaming gas, the jet also has a thin luminous plasma region, emanating from the orifice comprising of positive and negative ions, electrons, excited neutrals and photons. The ionised regions exist as discrete high velocity packages of plasma known as bullets [18]. The lengths of these visible plumes are 0.3 cm, 2 cm and 1.7 cm for the gas flow rates 0.67, 3.6 and 5.4 slm respectively. Surrounding the plasma column and extending downstream is a non-luminous halo of excited atomic and molecular species. These are mainly air species such as OH, O*, N and in some micro-plasma systems the O* (O ^{1}S and O^{1}D)) species have been seen to extend distances up to 30 cm from the exit [19]. Metastable He (He* (2^1S and 2^3S)) is also present in downstream gas as well as in the main discharge. Spatially resolved mass spectrometry has shown that plasma ions such He^+ and N^+ from N_2 entrainment exist mainly in the visible plasma region, with no detection recorded 2 mm outside the visible plume [8]. In the black and white schlieren photographs in figure 7.2a, b and c, the plasma region can not been seen but their lengths are indicated in figure 7.3.

The plasma and associated electric fields, believed to be sustained by photo-ionisation [14], can only exist in regions of non-turbulent He flow and as discussed by Laroussi et al and Karakas et al [20, 21], when helium gas concentration falls below a critical mole fraction, due to mixing with air, the plasma bullets which make the observed glow can no longer be conducted forward. Therefore, the length of visible plasma plume is limited to that of the laminar He region as shown in [5]. Here for flow rates above 3.6 slm, the decrease in the extension of the visible plasma is a consequence of increased mixing of air species in the He column as the flow becomes turbulent sooner after exiting the orifice.

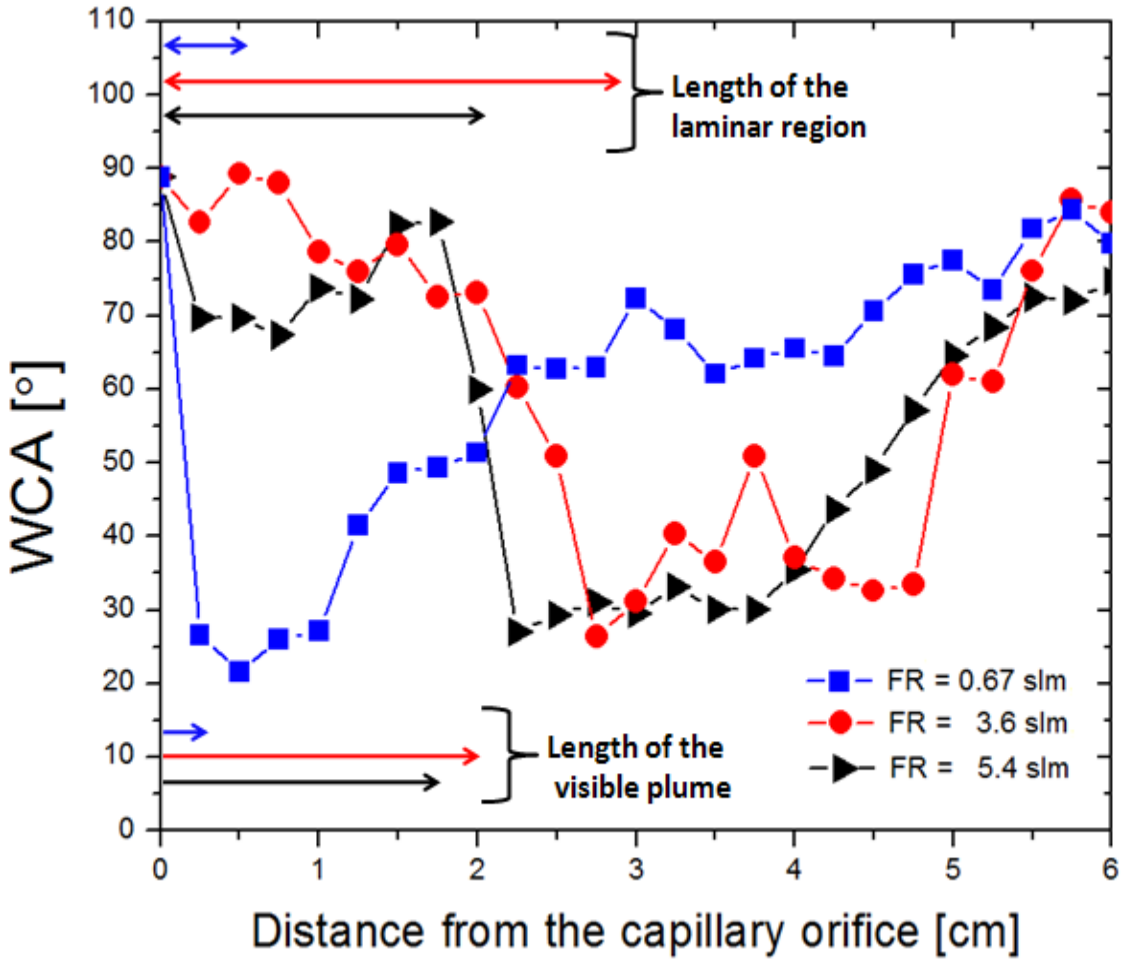

Figures 7.3: Water Contact Angle measurement results obtained for three different flow rates of 0.67, 3.6 and 5.4 slm from PS samples positioned side-on at a distance of 3 mm below the visible plasma plume. The applied voltage is 8 kV_{p-p} and the frequency is 30 kHz.

It is not known exactly which plasma and excited gas species are responsible for surface activation of the polymeric material in plasma micro-jet treatment applications, but we conjecture that reactions between ionised and metastable He atoms in the discharge (between the electrode and the exiting visible plume) with ambient air species including water vapour

gives rise to the existence of many radical species which are transported with flow. Since ionic species in the jet are not conducted far, it is these neutral species that probably play a dominate role in surface covalent bond breaking and the subsequent uptake of atmospheric oxygen, so reducing the degree of hydrophobicity. In addition energetic photons (UV or VUV) may also have a role in modifying the surface. These photons can only act in the pure He gas channel. Outside, atmospheric oxygen entrained in the flow rapidly absorbed these photons [22, 23]. Therefore, photon bombardment may be significant in head on-treatment where the visible plume is in contact with surface.

Figure 7.3 shows the detailed profiles of WCA measurements made along the line of symmetry from the exit orifice up to a distance of 7 cm from the capillary, for the three different flow rates. The PS samples were exposed to the jet effluent for 2 minutes in each case. The extension lengths of the visible plasma plumes and laminar flow regions are indicated in the figure. For untreated PS sample the WCA angle was measured to be 89° across a number of different samples. Along this line-of-sight we see in all the three cases a marked decrease in WCA down to about 25° or 30° in region whose position and width changes with flow rate. This change occurs very soon after the orifice for the low flow rate case of 0.67 slm, but between 2 and 2.5 cm for 5.4 and 3.6 slm respectively. Past these regions, with increasing distance downstream the WCA rises back to its untreated value. Figure 7.4 shows the 2-D distributions of WCA for flow rates of 0.67 and 5.4 slm respectively (note the reduced spatial resolution compared to data in figure 7.3.)

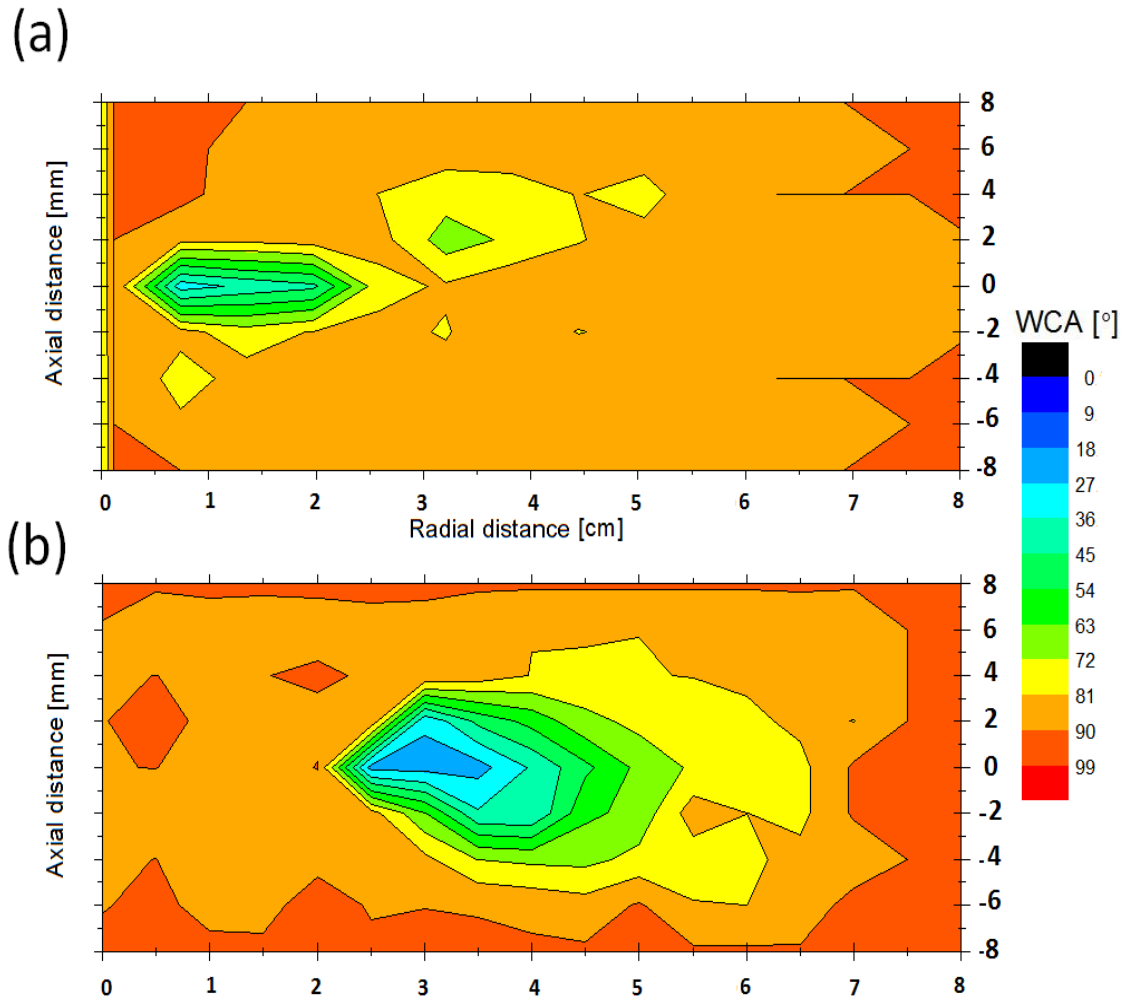

Figures 7.4: Spatially resolved Water Contact Angle measurement results obtained for two different flow rates (a) 0.67 and (b) 5.4 slm when PS samples were positioned side-on at a distance of 3 mm below the visible plasma plume. The applied voltage is 8 kV_{p-p} and the frequency is 30 kHz. Note: low WCA results represent regions of most treatment.

The results in figures 7.3 and 7.4 show that in regions where laminar of the gas (and the visible discharge) passes over the substrate only small changes in WCA occur, however once the gas becomes turbulent and impinges the surface, there is a significant lowering of the WCA. This modified region of the surface is about 3 cm long and 6 mm wide. The narrowness of the

treatment footprint shows that the species responsible for treatment are conveyed more effectively downstream than they are radially across the flow.

In the region of laminar flow the He gas has little or no entrained air species in it and therefore there are few oxygen or water based species that can diffuse across the flow and cause surface modification on the substrate directly below. In addition, energetic photons and ionic species such as He^+ , N^+ , OH^- (H_2O) known to be in the plasma plume [8] are not conveyed radially across the flow to the surface to cause bond-breaking.

The results of schlieren and WCA show that modification only happens to a large extent where the gas is turbulent, containing significant concentrations of excited air species which can get to the surface. The abrupt change in WCA at 0.3, 2.5 and 2 cm indicates that these excited species are created locally, (from reactions with plasma species) close to boundary between laminar and turbulent flow and then conveyed downstream. For 0.67 and 5.4 slm flow rates respectively, the longitudinal extension of the treatment are only about 2 and 5 cm indicating active species life times of about 1.4 ms and 0.43 ms respectively.

To investigate how the spatial distribution of treatment on the PS surface changes with time, WCA measurements were obtained and shown in figure 7.5. Here, the results for different treatment times (TT) of 20, 40, 60, 120 180 and 240 s respectively at a fixed flow rate of 3.6 slm are presented. At low treatment times of 20 s and 40 s, the change in WCA is ($\sim 10^\circ$ to 20°) across the PS surface due to little or no interaction of any of the He outflow along the whole length of the plume. For long treatment times of 60, 120, 180 and 240 s, significant

increases in WCA (~ 50° to 60°) are obtained with progressive broadening due to slow diffusion across the PS surface of active species arriving from the turbulent region.

Figure 7.6 shows comparative WCA results obtained when (a) the PS surface is allowed to interact directly with the plasma plume at distance d = 1mm, (b) when the PS surface was placed at d = 3mm as previously discussed and (c) when the PS surface is taken further away from the visible plume at distance d = 5 mm. The results show little or no treatment in WCA (~ 10° – 20°) in both laminar and turbulent regions when the PS samples were positioned too far from the visible plume at d = 5mm. This is due to no interaction of any of the outflow with the PS surface. However, when the PS samples were placed in direct contact with the outflow at d = 1mm, the WCA profile appears to be very similar to that obtained previously for d = 3mm i.e. ~ 10° – 20° in the laminar region and ~ 50° – 60° in the turbulent region. This is because we expect more interaction of the He outflow with the sample surface due to direct contact with the plume.

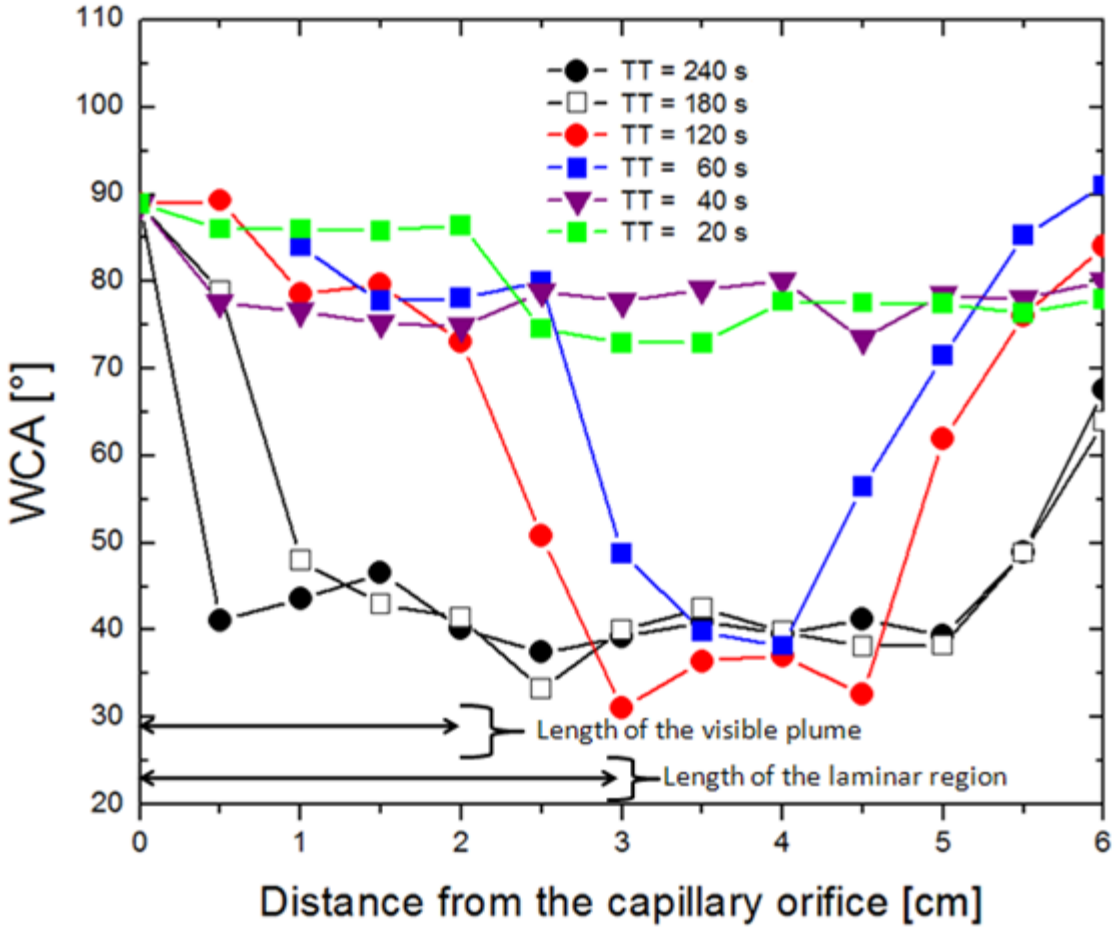

Figures 7.5: Water Contact Angle measurement results obtained for different treatment times 20, 40, 60, 120, 180 and 240 s for PS samples positioned side-on at a distance of 3 mm below the visible plasma plume. The applied voltage is 8 kV_{p-p} and the frequency is 30 kHz.

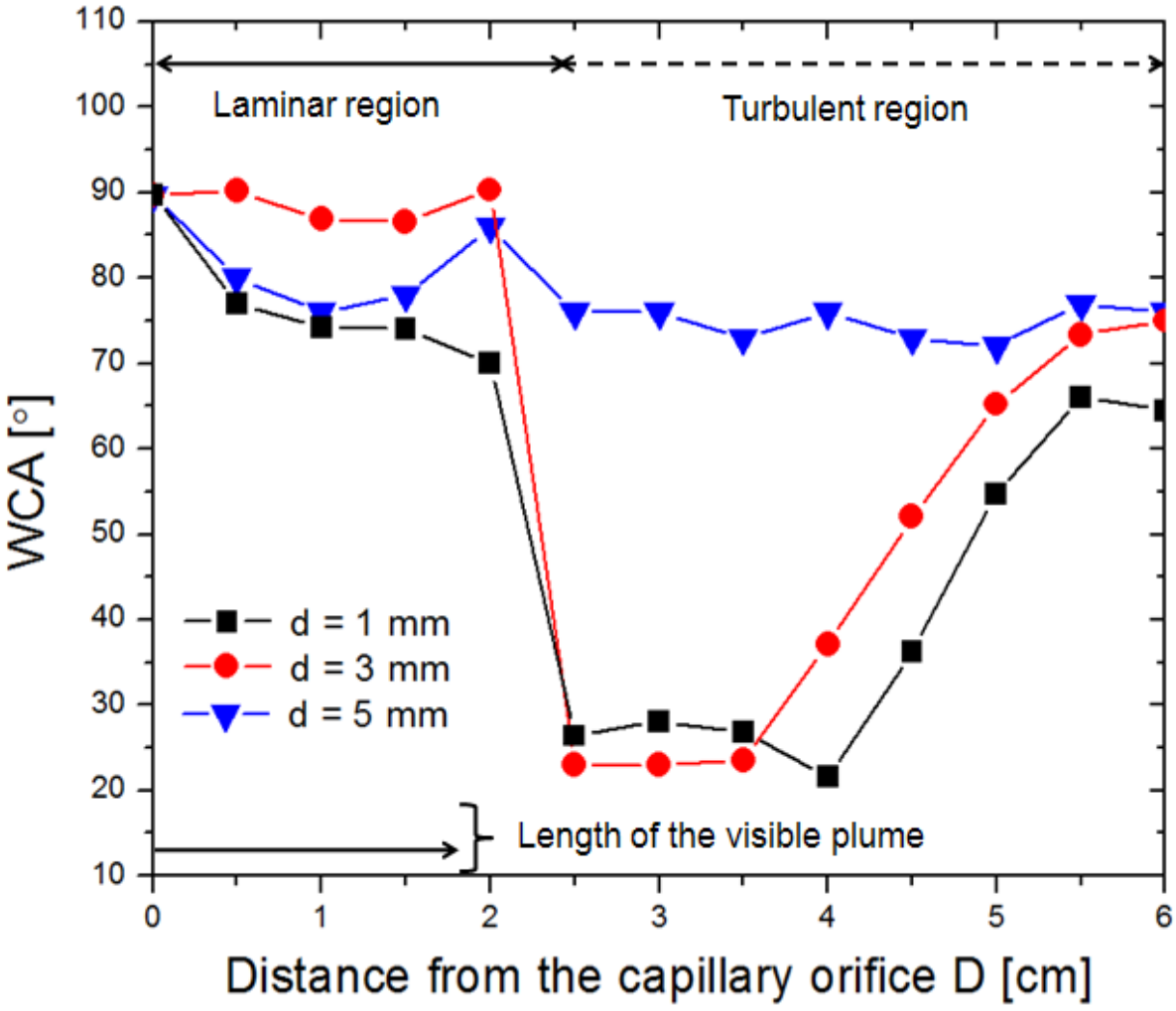

Figures 7.6: Water Contact Angle measurement results obtained at different distances d = 1 mm, 3 mm and 5 mm respectively for PS samples positioned side-on and below the visible plasma plume. The applied voltage is 8 kV_{p-p}, f = 30 kHz and F_R = 5.4 slm

In previous reports, it has been noticed that head-on treatment of polymeric materials using plasma micro-jets can lead to some surface damage, pitting or roughing with similar micro-

plasma devices [15, 16] and also with the jet configuration [24]. Figure 7.7 shows the results of head-on treatment on PS samples, where the AFM images show surface damages after different treatment times of 20 s and 40 s. Clearly, pitting with holes of ~ 1 – 2 μm are created in the head-on treatment. The direct, line of sight treatment appears to produce energetic species from the main discharge that can reach the substrate and damage it. These may be mainly due to the combination of high fluxes of excited species and photons impinging the surface in addition to low concentrations of other undetectable ions [8].

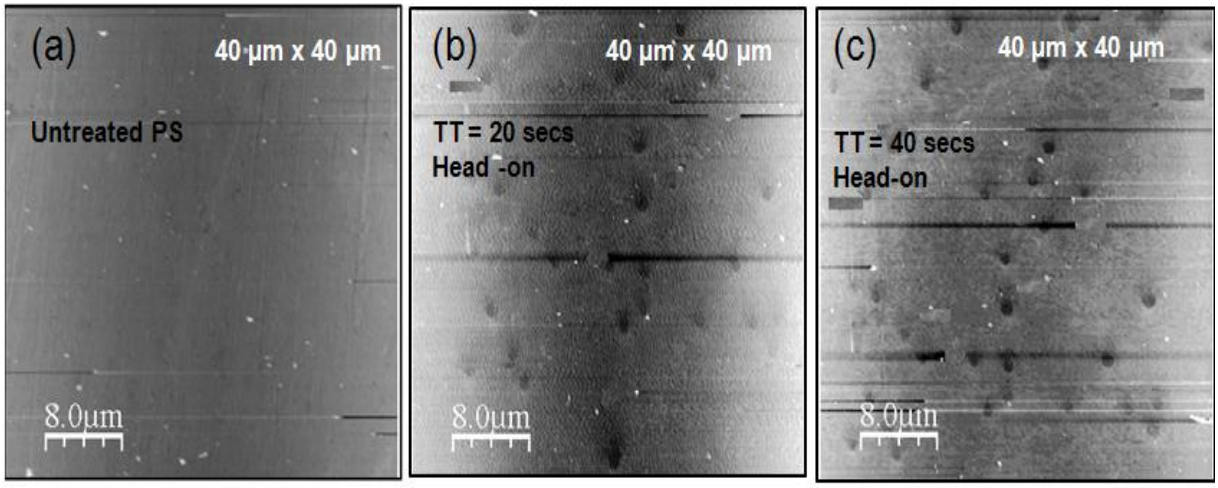

Figures 7.7: AFM images (40 μm x 40 μm) showing (a) untreated PS surface, (b) PS surface after TT = 20 s and (c) PS surface after TT = 40 s. V = 8 kV_{p-p}, f = 30 kHz and F_R = 3.6 slm.

To investigate whether side-on treatment shows these characteristics PS samples have been placed at 1 cm from the exit orifice in both side-on and head-on configurations for 40 s and 180 s respectively (shown in figure 7.8). Here, for short and long treatment times, the results show that the side-on treatment configuration is causing less damage to the PS surface and that the damages caused in the head-on configuration is not simply due to a high dose-effect

of the flux of reactive species impinging the surface due at long treatment times. For treatment time of 3 mins, we have obtained Ra values of 5.44 nm and 4.60 nm respectively for PS surfaces treated in the head-on configuration and side-on configuration respectively.

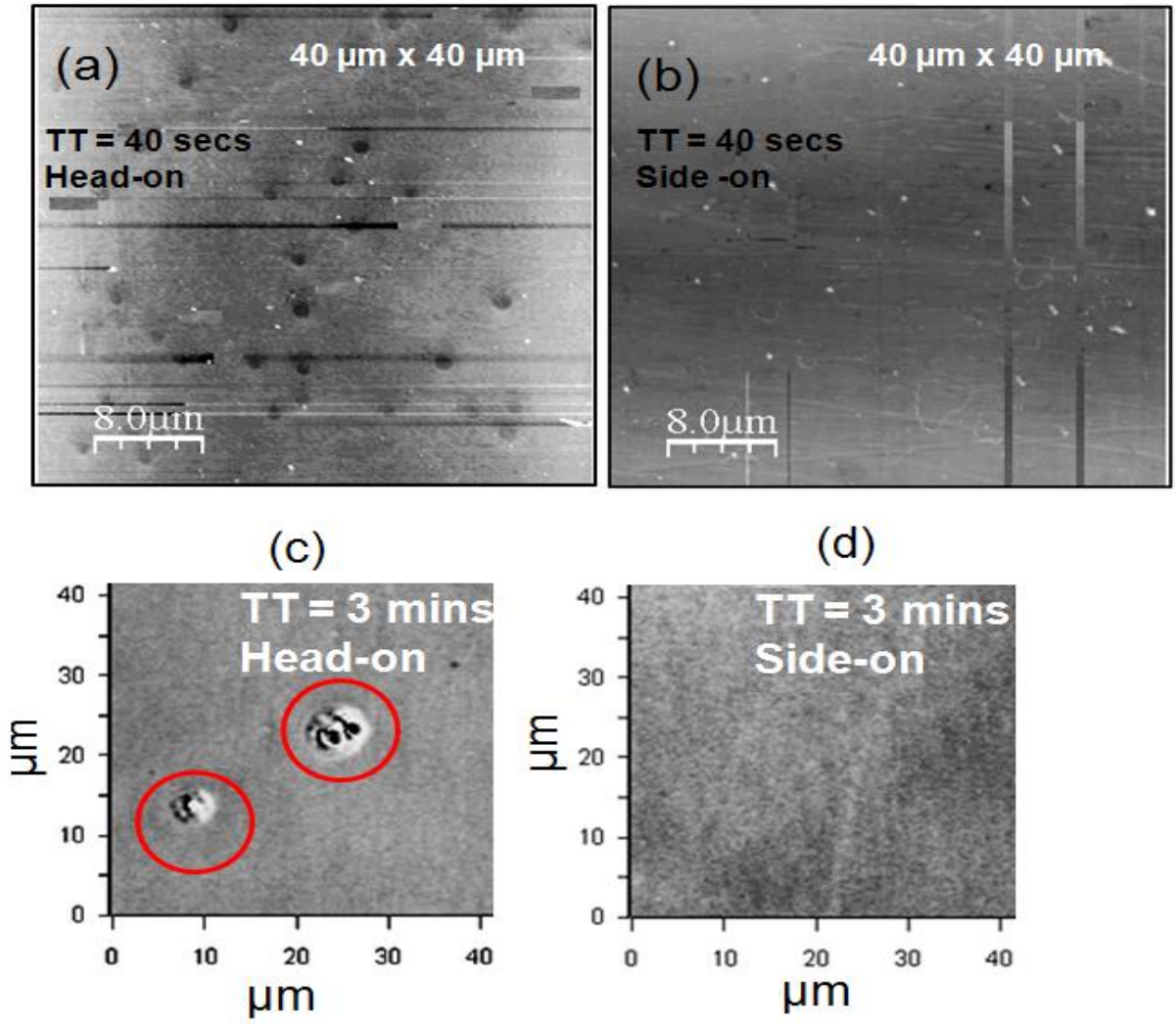

Figures 7.8: AFM images (40 µm x 40 µm) for **(a)** Head-on treatment for 40 s & **(b)** Side-on treatment for 40 s. Non-contact surface profile images for **(c)** Head-on treatment for 180 s (Ra = 5.44 nm) and **(d)** Side-on treatment for 180 s (Ra = 4.60 nm). V = 8 kV_{p-p}, f = 30 kHz and F_R = 5.4 slm.

PS Structure

Polystyrene is a long chain hydrocarbon wherein alternating carbon centers are attached to phenyl groups. It contains chemical elements carbon and hydrogen with the chemical formula given by $(C_8H_8)_n$ .The material forces are determined by van der Waals attractions between the polymer chains. Since the molecules are long hydrocarbon chains that consist of thousands of atoms, the total attractive force between the molecules is large. The structure is given below:

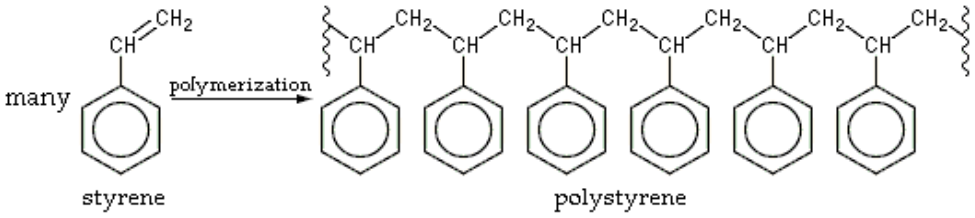

When heated (or deformed at a rapid rate, due to a combination of viscoelastic and thermal insulation properties), the chains are able to take on a higher degree of conformation and slide past each other. This intermolecular weakness (versus the high *intramolecular)* strength due to the hydrocarbon backbone) confers flexibility and elasticity. The ability of the system to be readily deformed above its glass transition temperature allows polystyrene (and thermoplastic polymers in general) to be readily softened and molded upon heating.

Here, we have investigated the effect of temperature on the water contact angle by pre-heating the PS samples for 10 minutes at 50 and 100 ºC and then comparing it with treatment at room temperature (shown in figure 7.9).From figure 7.9, we find that when the flow rate is fixed at 5.4 slm in all three cases, an increase in temperature from 20 to 50 ºC and then to 100 ºC

causes a larger area of surface modification possibly due to breakage of some of the van der Waals bonds on the polymer chains on the surface, and since we expect that the polymer chains to become more flexible and be able to move freely as the temperature is increased. Previous studies [25 - 27] suggest that temperature variations affect stereoregularity, tacticity, elastic young's modulus and the stress-optical coefficient of polystyrene. The stress-optical coefficient as well as the elastic young's modulus also appears to decrease linearly with increasing temperature according to results from these studies when a temperature range of -195 ºC to +24 ºC was applied. This coefficient in the glassy state is determined mainly by the polarizability of the phenyl groups which is largest in the plane of the benzene ring (see structure above). These phenyl groups become twisted on application of tensile stress so that they align in the direction of the applied stress [25].

According to the results by Rudd et al, a strain-optical coefficient which can be obtained by multiplying the stress-optical coefficient with the young's modulus appears to increase with decreasing temperature from – 195 ºC up to room temperature.

Spatially resolved Water Contact Angle measurement results at the three different temperatures (shown in figures 7.10, 7.11 and 7.12) have been compared for PS samples positioned side-on at a distance of 3 mm below and parallel to the visible plasma plume. Axial and radial scan profiles at the same position along the surface of the PS sample show a significant increase in the area of treatment as the temperature is increased from 20 to 100 ºC.

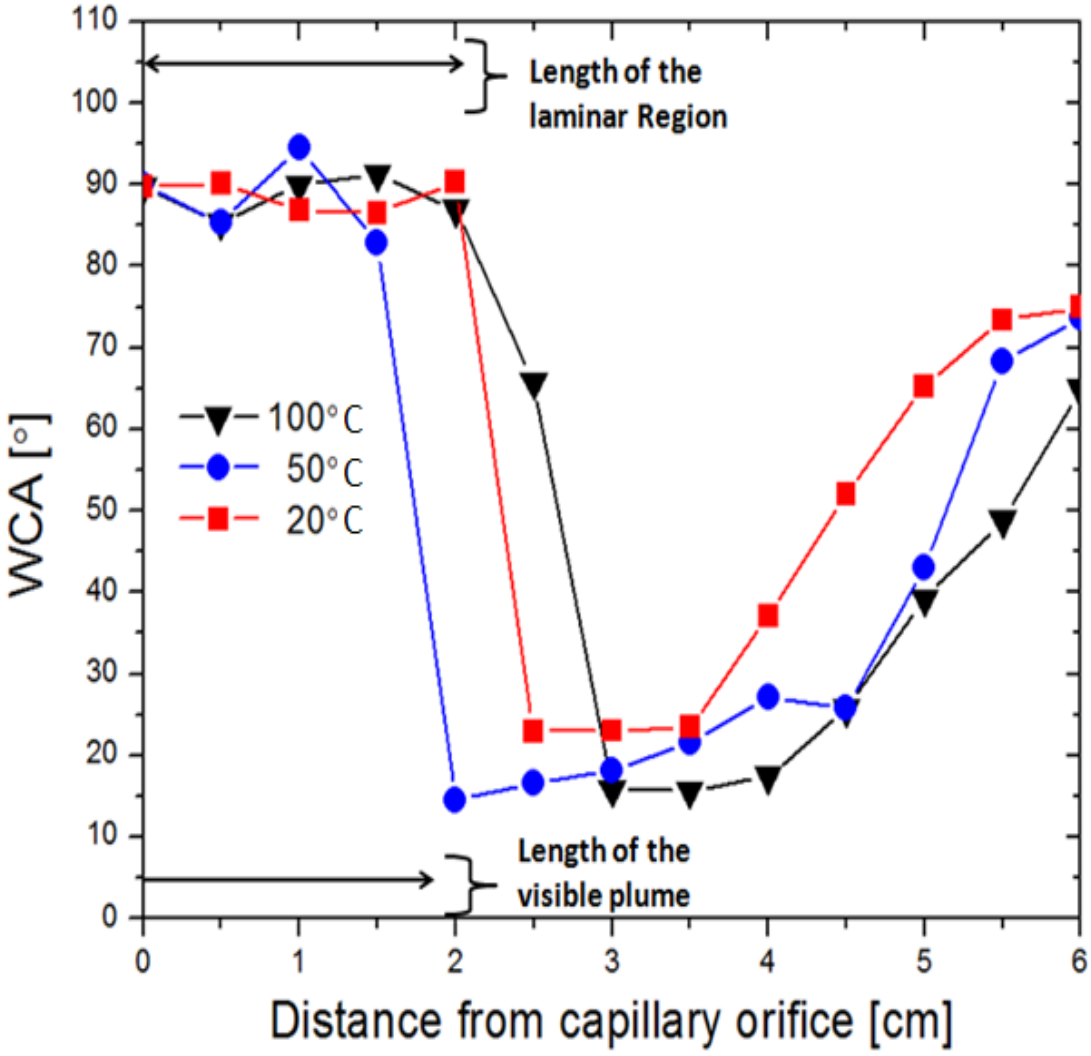

Figure 7.9: Water Contact Angle measurement results obtained for three different temperatures 20, 50 and 100 ° C at a constant flow rate of 5.4 slm. PS samples positioned side-on at a distance of 3 mm below the visible plasma plume. The applied voltage is 8 kV_{p-p} and the frequency is 30 kHz. Values taken from the radial centre of the orifice.

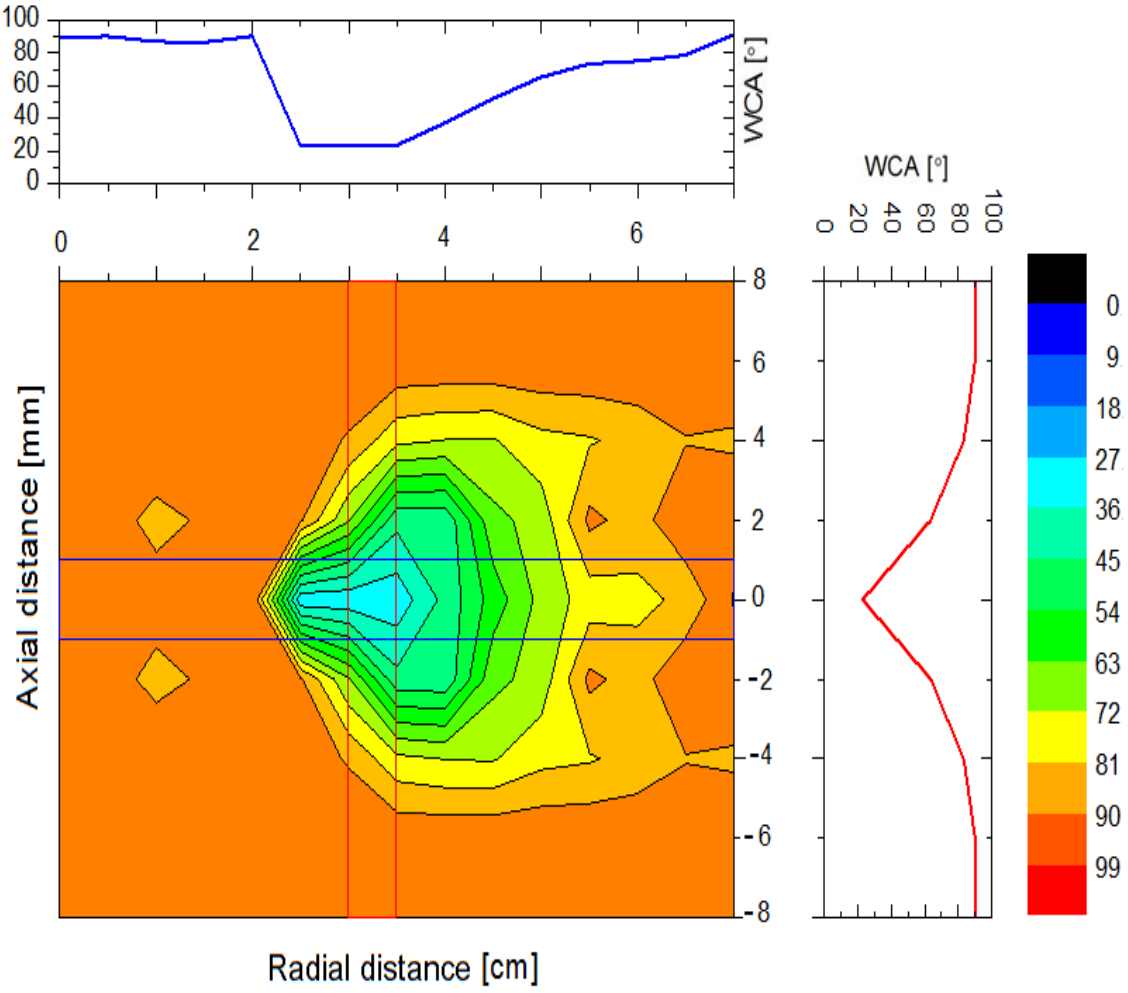

Figure 7.10: Spatially resolved Water Contact Angle measurement results obtained by keeping PS sample at room temperature (~ 20 ºC) prior to treatment. PS samples were positioned side-on at a distance of 3 mm below the visible plasma plume. The applied voltage is 8 kV_{p-p} and the frequency is 30 kHz. Note: low WCA results represent regions of most treatment. Axial and radial scan profiles shown for a fixed position.

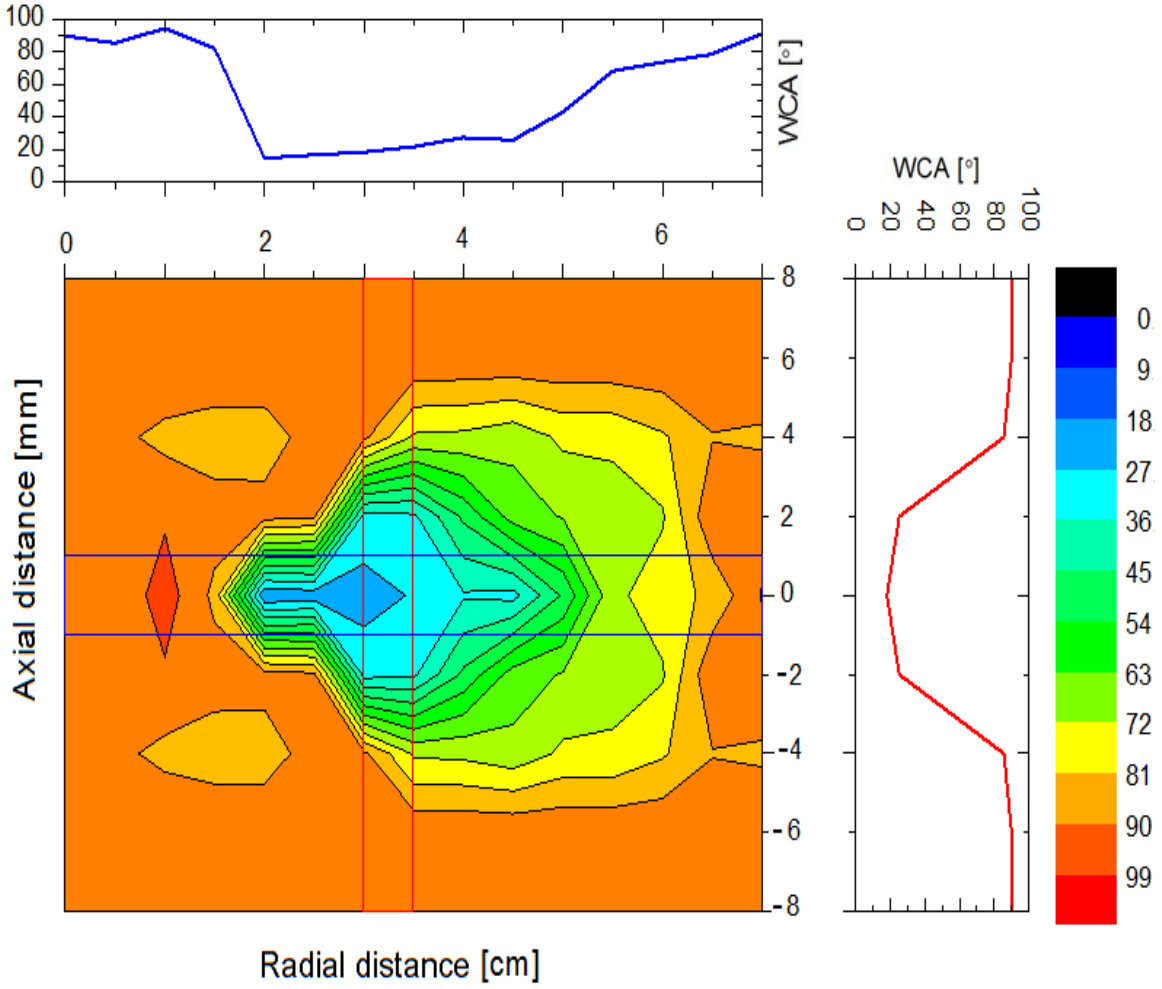

Figure 7.11: Spatially resolved Water Contact Angle measurement results obtained by preheating PS sample for 10 mins at 50 ºC prior to treatment. PS samples were positioned side-on at a distance of 3 mm below the visible plasma plume. The applied voltage is 8 kV_{p-p} and the frequency is 30 kHz. Note: low WCA results represent regions of most treatment. Axial and radial scan profiles shown for a fixed position.

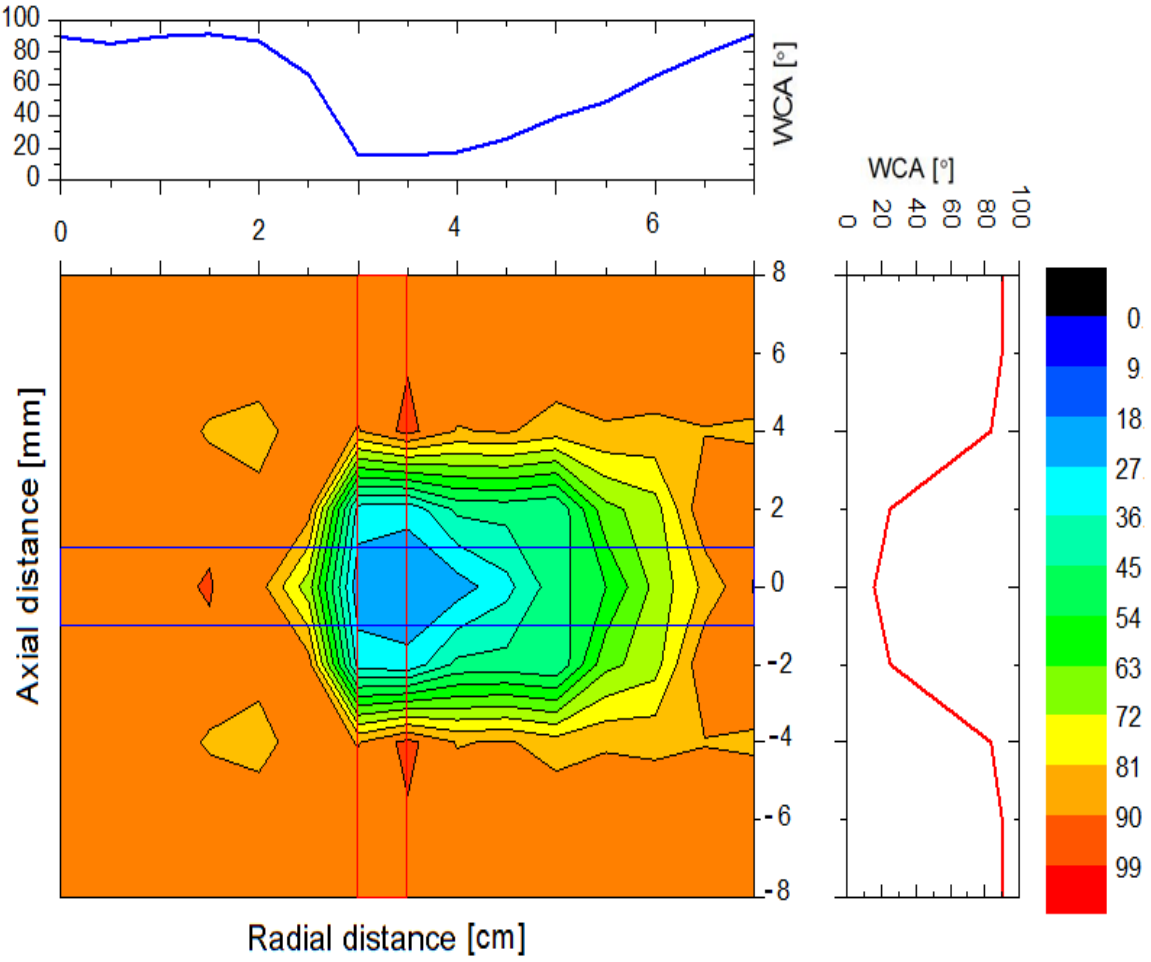

Figure 7.12: Spatially resolved Water Contact Angle measurement results obtained by preheating PS sample for 10 mins at 100 ºC prior to treatment. PS samples were positioned side-on at a distance of 3 mm below the visible plasma plume. The applied voltage is 8 kV_{p-p} and the frequency is 30 kHz. Note: low WCA results represent regions of most treatment. Axial and radial scan profiles shown for a fixed position.

7.4 Conclusions

Using a combination of schlieren imaging and spatially resolved WCA measurement the effect of laminar and turbulent flows on the surface modification of PS has been investigated in the exit stream of a micro-plasma jet operating in He. The jet was aligned in a side-on configuration with the exiting flow across, rather than directly on to, the substrate. For short treatment times in regions where turbulent flow, (consisting of He gas mixed with excited air species), interacts with the substrate, a significant lowering of the WCA (60°) is achieved. In addition, little or no surface modification occurs directly below the laminar flow region (containing He plasma species and photons) existing immediately outside the jet exit orifice for these short treatment times. However, as the treatment time is increased up to 180 s, the high flux of charged and reactive species entrained in the He outflow interact considerably with the entire PS surface resulting in a significant WCA reduction of ~ 60° across the entire surface.

The effect of changes in substrate temperature on the WCA on the PS surface has also been investigated. From the results obtained, an increase in temperature from 20 to 50 ºC and then to 100 ºC causes a larger area of surface modification possibly due to breakage of some of the van der Waals bonds on the polymer chains on the surface due to the fact that the polymer chains become more flexible and are able to move freely as the temperature is increased. However, the explanation for this trend is intended to be suggestive only and there is need for further investigation before a detailed analysis can emerge.

Future experimental work that correlates the densities of active species in the plasma plume with the changes observed on the heated PS surface will provide useful information about the influence and importance of temperature in surface modification applications.

The size and shape of the treatment profile provides a basis for further investigations into the complex mechanisms underpinning the behaviour of radicals and reactive species in the turbulent gas region in the jet plume. Not only this, the "side-on" treatment may offer some advantages over the more conventional "head-on" treatment configuration, allowing different more elongated treatment areas to be defined and with reduced or no surface damage.

References

1. J. L. Walsh, J. J. Shi, M. G. Kong, Appl. Phys. Lett. 2006, 88 ,171501

2. P. Bruggeman, F. Iza, P. Guns , D. Lauwers, M. G. Kong, Y. Aranda Gonzalvo, C. Leys, D. C. Schram, Plasma Sources Sci. Technol. 2010, 19 , 015016

3. R. Ye, W. Zheng, Appl. Phys. Lett. 2008, 93, 071502

4. J. Engemann, IEEE Trans.Plasma Sci. 2005, 33, 310

5. J.-S. Oh, O. T. Olabanji, C. Hale, R. Mariani, K. Kontis, J. W. Bradley, J. Phys. D, Appl. Phys. 2011,15, 155206

6. R. Kakei, A. Ogino, F. Iwata, M. Nagatsu, Thin Solid Films. 2010, 518, 3457

7. S. Mazouffre, I. Bakker, P. Vankan, R. Engeln, D. C. Schram, Plasma Sources Sci.Technol. 2002, 11, 439

8. J.-S. Oh, Y. Aranda-Gonzalvo, J. W Bradley, J. Phys. D: Appl. Phys. 2011, 44, 365202

9. E. J. Szili, S. A. Al-Bataineh, P. M. Bryant, R. D. Short, J. W. Bradley, D. A. Steele, Plasma Process. Polym. 2011, 8, 38

10. M. Laroussi, T. Akan, Plasma Process. Polym. 2007, 4, 777

11. A. Vogelsang, A. Ohl, H. Steffen, R. Foest, K. Schroder, K.-D. Weltmann, Plasma Process. Polym. 2010, 7, 16

12. H. Ayan, E. D. Yildirim, D. D. Pappas, W. Sun, Appl. Phys. Lett. 2011, 99, 111502

13. L. Chen, P. Zhao, X. Shu, J. Shen, and Y. Meng, Phys. of Plasmas. 2010, 17, 083502

14. C. Jiang, M. T. Chen, M. A. Gundersen, J. Phys. D: Appl. Phys. 2009, 42, 232002

15. S. A. Al-Bataineh, E. J. Szili, A. Mishra, S.-J. Park, J. G. Eden, H. J. Griesser, N. H. Voelcker, R. D. Short, D. A. Steele, Plasma Process. Polym. 2011, 8, 695

16. T.-H. Chen, C.-H. Liu, J.-T. Teng, C.-H. Su, C. Huang, H.-L. Sheu, S. Lin, Surf.

Interface Anal. 2009, 41, 886

17. J.P Holman, Heat transfer, McGraw-Hill, 2002, 207

18. M. Teschke, J. Kedzierski, E. G. Finantu-Dinu, D. Korzec, J. Engermann, IEEE Trans. Plasma Sci. 2005, **33,** 310

19. N. Knake, V. Schulz-von der Gathen, Eur. Phys. J. D. 2010, 60, 645

20. M. Laroussi, X. Lu, Applied Physics Letters. 2005, 87, 113902

21. E. Karakas, M. Koklu, M. Laroussi, J. Phys. D: Appl. Phys. 2010, 43,155202

22. K. Yoshino, W. H. Parkinson, K. Ito, T. Matsui, J. Mol. Spectrosc. 2005, 229, 238

23. M. Ackerman, F. Biaumé, G. Kockarts, Planet. Space Sci. 1970, 18 ,1639

24. E. J. Szili, S. A. Al-Bataineh, R. D. Short, D. A. Steele, Mawson Institute (UNISA) – private communication.

25. J. F. Rudd, E. F. Gurnee, J. Appl. Phys. 1957, **28**, 1096

26. F. Zaiee, H. F. Mobarakeh, Iranian Polymer Journal. 2011, 20, No. 3

27. J. L. Weaver, C. L. Beatty, Polymer Engineering and Science. 1978, 78, No. 14

CHAPTER EIGHT

8.0 Plasma Assisted Desorption Ionisation (PADI)

Abstract

A novel plasma assisted desorption ionisation (PADI) method that can be coupled with atmospheric pressure sampling mass spectrometry has been designed and set up at National Physical Laboratory (NPL). The PADI source which comprises non-thermal RF plasma has been successfully interfaced with a mass spectrometer to yield mass spectral information under ambient conditions of pressure and humidity. The non-thermal plasma directly interacts with the surface of the analyte causing desorption and ionization to occur. The ions produced are then analysed by the mass spectrometer. Here, we have used the PADI source for the analysis of pharmaceuticals, which identified the active ingredient and gave clean spectra in both positive and negative ion mode. This study aims to improve the spatial resolution of spectra obtained in comparison to other conventional sampling methods.

8.1. Introduction

PADI source is a non-thermal, radio-frequency driven cold atmospheric glow discharge with a temperature close to that of the ambient surroundings. It is often characterised by higher current characteristics and lower operating voltage typically at 300 V_{p-p} and applied power of less than 5 W in comparison to corona discharges. The glow discharge is cold to touch, self-

sustaining and results in relatively low ion energies, typically less than 5 eV and not exceeding 20 eV. This allows for direction interaction with the sample or analyte without heating it. The PADI source is distinct from other conventional sources such as the Desorption Electrospray Ionisation (DESI), Direct Analysis in Real time (DART) and related techniques [1]

Recently, Ratcliffe et al [1] developed a new PADI source that uses cold helium plasma to desorb and ionise molecules at surfaces under ambient conditions. This shows great promise in being able to desorb more strongly bound molecules which is a limitation of DESI. Applications range from pharmaceutical and biomedical analysis in areas as varied as tumour analysis and medical device analysis, biological analysis for research and development or drug delivery testing, forensic analysis, explosive detection and battlefield analysis, environmental monitoring, testing of counterfeits in drugs and food, production line testing for consistency or faults and point of care diagnostics [2].

Here, the PADI source consists of a non-thermal plasma needle operating at atmospheric pressure, based on the plasma needle design by Sladek et al [3]. The source was interfaced to a mass spectrometer and comprises a stainless steel wire, 190 mm long and 0.75 mm diameter, sharpened into a needle-like point at one end. The wire serves as a powered electrode and is placed coaxially within a ceramic tube (1.2 mm ID, 2.5 mm OD) which is itself placed coaxially within a quartz tube (5 mm ID., 7 mm OD). Even though this configuration is slightly different to our setup, the mechanisms for desorption and ionisation are fundamentally the same.

Helium is used as the sheath gas as it offers a lower breakdown voltage and more stability from the glow-to-arc transition compared to other gas mixtures. The mixing of air with helium at the interface of the needle and the atmosphere produces radicals in the gas phase. O and

OH radicals as well as ions such as OH+, O+, O-2(+), He-2(+), HeH+ and H-3(+) which have been identified [4] are most likely to be formed. Metastable He is formed by electron-impact excitation collisions. Electronic energy transfer due to metastable helium and ion impacts could cause desorption [5]. Thermal desorption could be partly responsible for desorption, though it is unlikely that it plays a large role as there is very little heating of the discharge gas.

8.2 Mass Spectrometer Coupling

Figure 9.1 shows a figure of the PADI source in action for the analysis of one of the samples. The PADI source was mounted on a fixed frame support to reduce the impact of vibrations caused by movements or other sources during experimentation. The tip of the plasma was placed at a reasonable angle (45° - 75°) and distance of ~ 1 to 2cm from the tungsten sniffer of the mass spectrometer in order to obtain clean and stable mass spectra with fairly negligible background signal. The samples were placed in such a way as to allow for maximum collection of ions and radicals without over saturation. We found that localised treatments with minimum penetration depth at short treatment times of 10 to 60 seconds gave optimum results. This is because long time treatments appear to decolourise and damage the sample.

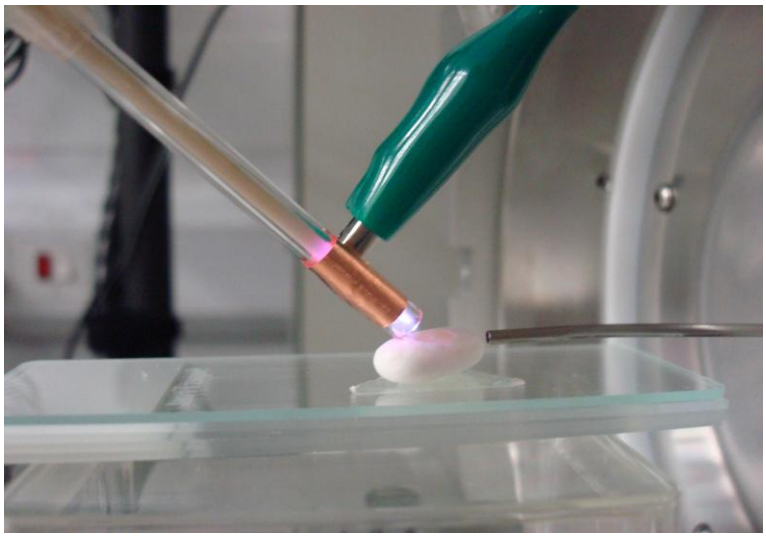

Figure 8.1: PADI in action on the mass spectrometer for the analysis of ibuprofen tablet [1]

8.3 Experimental set up

The non-thermal atmospheric RF plasma source was obtained using a coupling of both the RF generator and a matching network, tuned to a frequency of 13.56 MHz. The lossless RF coaxial cable was interfaced to a PTFE gas supply tube and a cylindrical glass tube using a plastic "Tee connector". The outer glass tube of 2.5mm inner diameter envelopes a hollow cylindrical ceramic insulator that encases tungsten pen/wire of 0.75 mm diameter (ID). Gas leakages were minimized using PTFE sealant tapes at the connector threads. The PADI pen was successfully optimised using a grounded electrode configuration at the open end of the glass tube, where the tip of the tungsten wire is exposed.

The grounded electrode was used to focus, stabilise and elongate the plasma needle /plume. The gas flow rate was observed and recorded using a calibrated rotameter, connected to a PTFE gas supply tube at one end and the "Tee connector" at the other. Helium gas was used

in this case to generate the plasma using RF power of 10 - 15 W. It was found that the automatic matching network (which sets the impedance to reduce reflections) did not work sufficiently well. We optimised the network manually by monitoring the RF signal quality from a pick up coil attached to an oscilloscope. Figure 8.2 shows results obtained from experimental measurements using a high speed digital camera and a measuring ruler. The vertical axis shows the distance of elongation of the plasma needle or plume while the horizontal axis shows the flow rates in mL/min for helium gas.

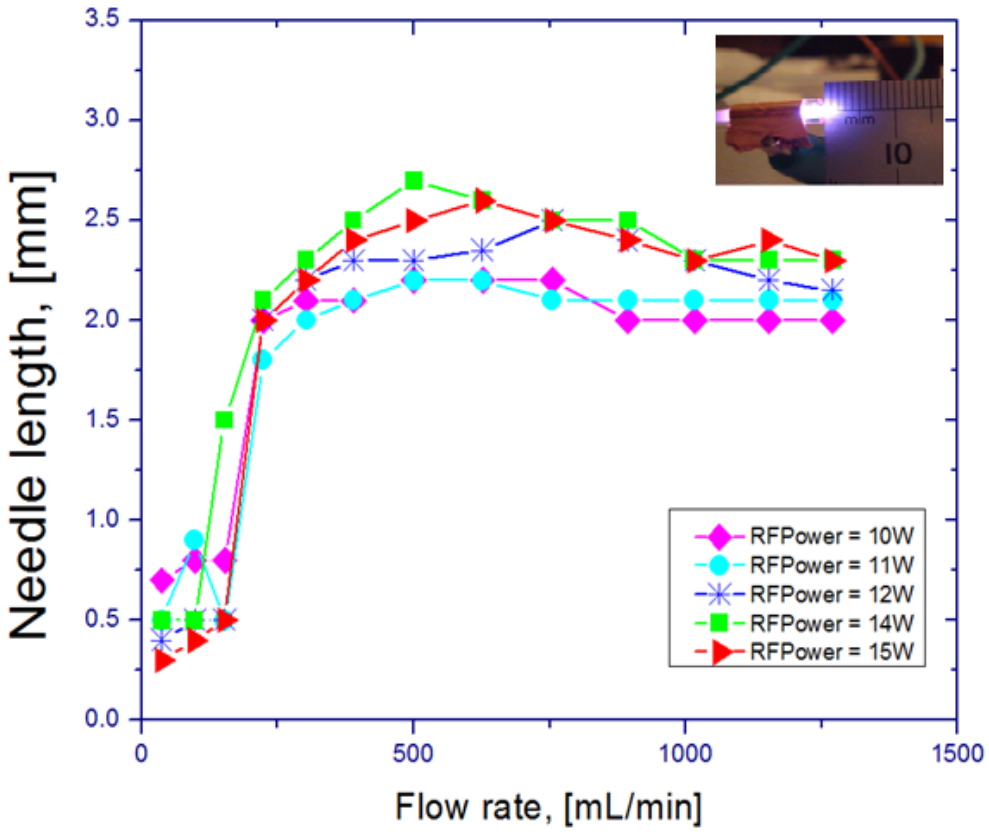

Figure 8.2: Effect of helium flow rate and RF power on plasma plume length, *L*. Photo inset shows plasma and measurement of *L*.

The RF power was obtained by subtracting the reflected power from the real power applied, assuming a lossless line. Here it is seen that the plasma needle length increases with increasing flow rate up to a certain point (~ 500 mL/min) after which it decreases or stabilises. Also, it was found that an increase in RF power yields a corresponding increase in needle/plume length up to a certain point at which a further increase only intensifies the plasma but does not elongate the plasma needle.

8.4 Results and Discussions

A mass spectrum of pharmaceutical tablets such as ibuprofen and paracetamol were analysed using the PADI source. The results are shown in figures 8.3, 8.4 and 8.5 for positive and negative ion modes. The mechanisms of desorption and ionization are still not fully understood but suggestions that positive ionization mechanisms include a combination of direct electron impact ionization, metastable penning ionization and ion-molecule reactions have been reported [6]. The H_e (2^3S) metastable state has an energy of 19.8 eV, and it is well-known that such species can induce desorption from surfaces of either neutral molecules or ions.

$$H_e\ (2^3S) + M \rightarrow M^+ + H_e\ (1^1S) + e \qquad (8.1)$$

The reaction of the helium (2^3S) state with water is very efficient [7], and the suggestion that analyte ionization mechanism in PADI proceeds via combination of ionized water cluster formation and proton-transfer reactions has been reported [1]

$$H_e\,(2^3S) + nH_20 \rightarrow H_30^+\,(H_20)_{n-2} + OH^- + H_e\,(1^1S),\ n > 1 \qquad (8.2)$$

$$H_30^+\,(H_20)_n + M \rightarrow MH^+ + (n+1)\,H_20 \qquad (8.3)$$

This mechanism is supported by observations of both M^+ and MH^+ fragments and also H^3O^+ $(H_20)_n$ clusters from the PADI source (data not shown) and predicts that each mechanism plays a part in the ionization of analytes in this technique.

Negative ion formation is thought to proceed via direct and dissociative electron attachment to oxygen species, producing e.g., O_2^-, which then react with analyte molecules to produce predominantly $[M - H]^-$ groups. These and other core negative ion species have been measured from the PADI source and previously in similar discharges [8].

Desorption processes are less well understood, but a suggestion that a combination of energy transfer from metastable helium, ion impact, and radical-surface interactions contribute to the mechanisms in the PADI technique has been reported [1]. Figures 8.3 show the positive ion mode spectrum of ibuprofen tablet with a distinct molecular peak at m/z 207.

Figure 8.3 a shows the results obtained using our current configuration while figure 8.3 b shows the result obtained by Ratcliffe et al in [1]. Figures 8.4 a and b show the negative ion mode spectrum of ibuprofen tablet, showing the molecular peak at m/z 205.

Figure 8.4 a shows the results obtained using our current configuration while figure 8.4 b shows the results obtained in similar studies reported in [1] .The PADI source was also used to analyse negative and positive ion mode spectra of paracetamol tablet (shown in figure 8.5) and other tablets (not shown).

Figure 8.5 shows the results for the positive ion mode spectrum obtained for paracetamol tablet with insert results from similar studies reported in [1].

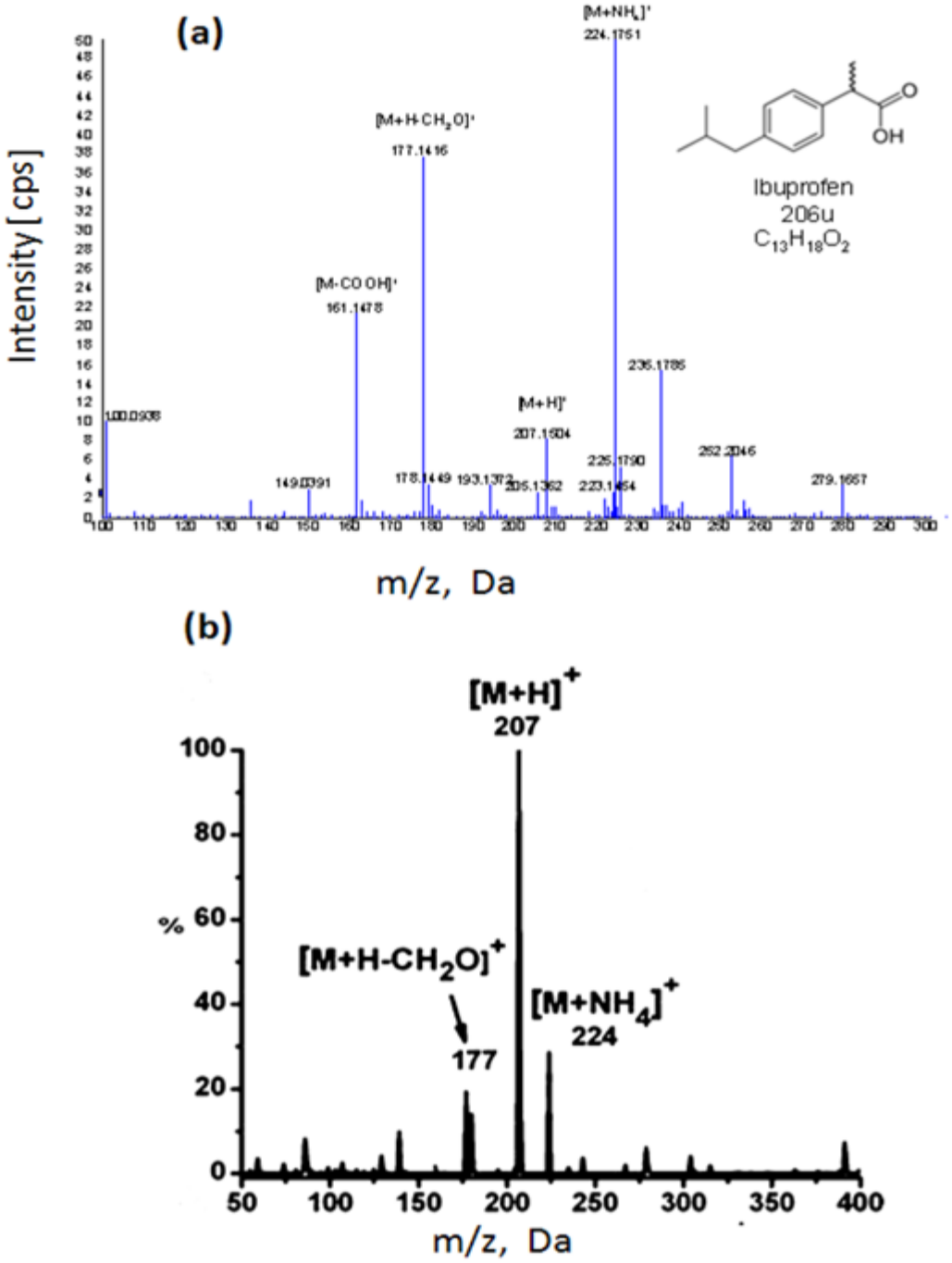

Figure 8.3: Positive ion mode spectrum of ibuprofen, showing the molecular peak at *m/z* 207, plus other fragment and adduct ions characteristic of the molecule. Inset shows positive ion spectrum of ibuprofen using MHCD [9] (note that mass scales are different).

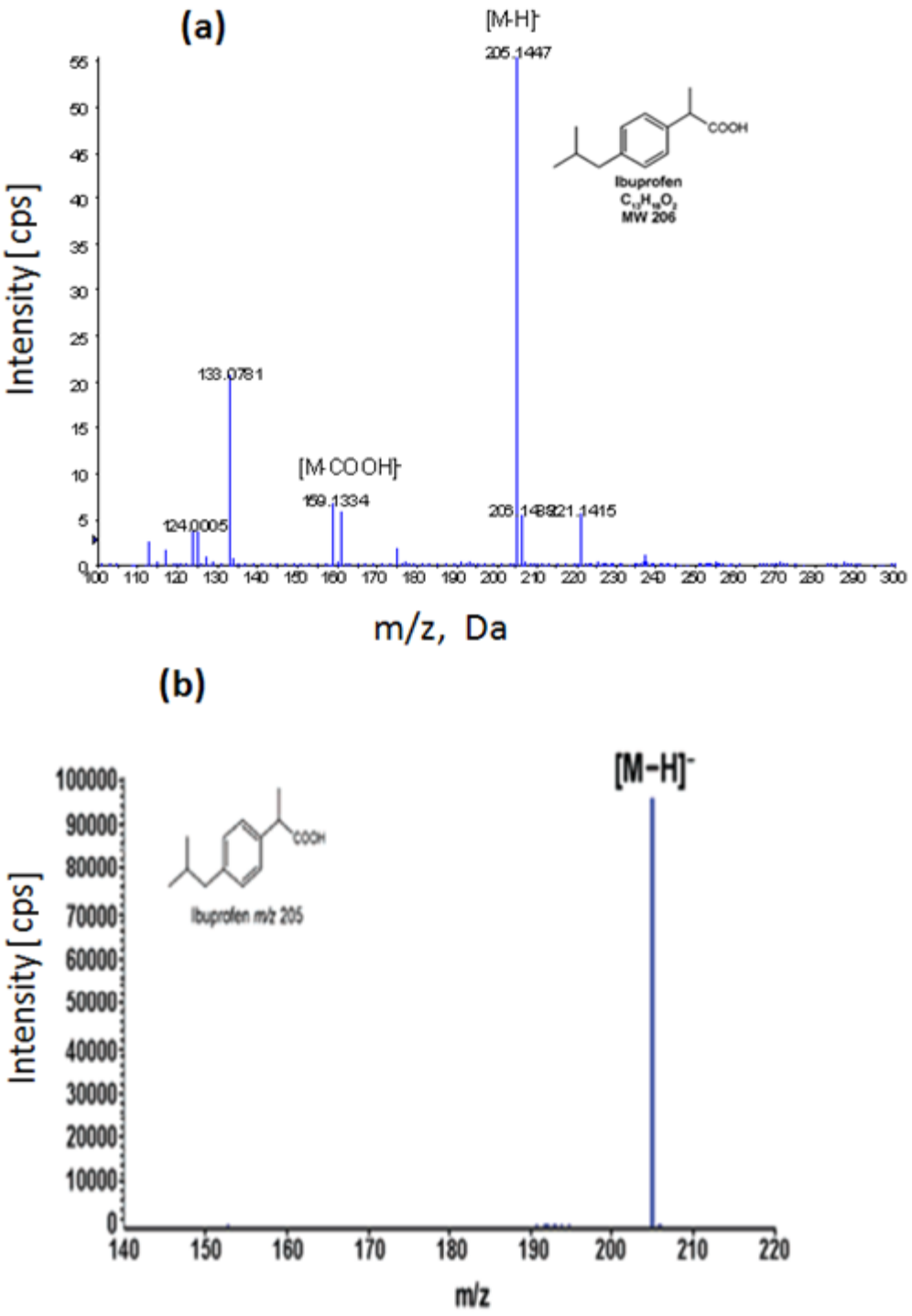

Figure 8.4: Negative ion mode spectrum of ibuprofen, showing the molecular peak at m/z 205, with insert showing PADI spectrum obtained in [2] (note that mass scales are different).

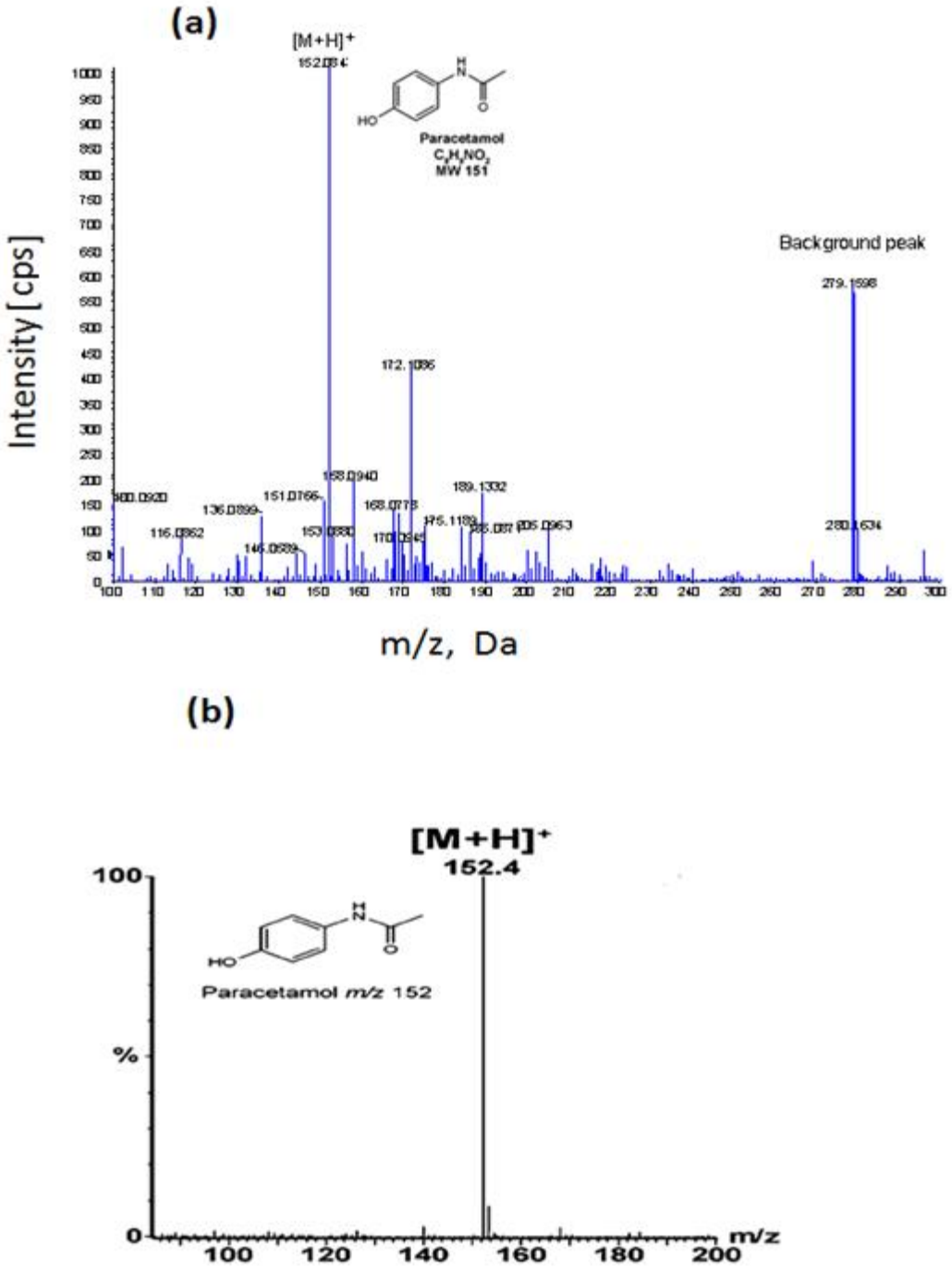

Figure 8.5: Positive ion spectrum of a paracetamol tablet, showing the molecular peak and a common background peak. Inset shows spectrum from the literature [2] for comparison (note that mass scales are different).

8.5 Conclusions

We have demonstrated the potential of the PADI technique as a potential candidate for surface analysis in pharmaceutical applications. This methodology has great potential for future applications as it can be easily interfaced to mass spectrometers that have an atmospheric pressure inlet.

This technique does not require solvent or sample preparation prior to analysis as it is simple, fast, capable of high-throughput analysis and less angle- dependent in respect of the sample to the mass spectrometer inlet in DESI technique. The mass spectra results obtained are in good agreement with those reported [1] and also cleaner than those obtained with DESI technique. The results show strong molecular peaks and low background signals.In the analysis of ibuprofen, the molecular peak was best observed in the negative ion mode at 205 m/z, and a fragment [M-COOH] at 159 m/z. The peak identification was confirmed from daughter fragment ions using MS/MS. In the positive ion mode, the strongest peaks came from the ammonium adduct, 224 m/z, and also the protonated molecular peak with loss of formaldehyde, 177 m/z. These peaks were also observed by the MHCD [9].

References

1. T. L. Salter, F. M. Green, O. T. Olabanji, J. W. Bradley, PADI report (private communication)

2. V. L. Ratcliffe, F. J. M. Rutten, D. A. Barrett, T. Whitmore, D. Seymour, C. Greenwood, S. Robinson, Y. Aranda-Gonzalvo, M. McCoustra, *Anal. Chem.* **2007,** *79,* 6094-6101

3. R. E. J. Sladek, E. Stoffels. *J. Phys. D: Appl. Phys.* **2005,** *38,* 1716–1721

4. P. Bruggeman, F. Iza, D. Lauwers, Y. A. Gonzalvo, *J. Phys. D: Appl. Phys.* **2010,** ***43.*** 012003

5. J. M. Symonds, A. S. Galhena, F M Fernandez, T. M. Orlando. *Anal. Chem.* **2010**, *82*, 621-627

6. Harada, Y.; Masuda, S.; Ozaki, H. Chem. Rev. 1997, 97, 1897-1952.

7. Searcy, J. Q.; Fenn, J. B. J. Chem. Phys. 1974, 61, 5282-5288.

8. Aranda Gonzalvo, Y.; Greenwood, C. L.; Whitmore, T. D.; Rees, J. A. Mass spectrometric investigation of an atmospheric dielectric barrier discharge in helium: positive and negative ions. 7th Workshop on Frontiers in Low Temperature Plasma Diagnostics, Beverley, U.K., April, 2007

9. J. D. Harper, N. A. Charipar, C. C. Mulligan, X. Zhang, R. G. Cooks, Z. Ouyang. *Anal. Chem.* **2008**, *80*, 9097–9104

CHAPTER NINE

9.0 Conclusions and Outlook

An atmospheric pressure DBD operating in a closed bonded microchannel with flowing helium and neon gases in electrode gaps of 250 μm, 300 μm and 450 μm has been studied. Electrical measurement results show that the discharges are filamentary and comprise numerous current filaments of short widths (10-100 ns) per half cycle that first appear at breakdown voltage and then increase in number as the applied voltage is increased beyond breakdown voltage. However, for a patterned DBD, the current filaments initially increase in number but subsequently decrease as the frequency is increased. 2D optical imaging results show similar microdischarge patterns for each half-cycle of the normal DBD but two distinct microdischarge patterns for the positive and negative half-cycles. High emission regions are seen corresponding to regions of high electric fields and lower intensities in the surrounding regions. Our results also show that the breakdown voltage depends on the ionization potential of the gas, flowate, operating frequency and the electrode gap of the microfludidic chip.

An atmospheric pressure microjet operating in an open glass capillary system has been used in both head-on and side-on configurations to modify locally the surface energy of polystyrene (PS). Schlieren photography has been used to indentify regions of laminar and turbulent flow in the exiting gas stream and their interaction with a PS substrate. The lengths of these two regions have been shown to vary depending on operating parameters i.e. frequency, voltage and flow rate. WCA measurement results show significant reductions in WCA (~50 to 60 °) in

the turbulent region where the turbulent gas mixed with air impinges the surface and only small changes in WCA (~50 to 60 °) in regions closer to the exit orifice where the helium (He) flow is still laminar across the surface. The results indicate that excited air species (either mixed or entrained in the He gas flow) which exist only in regions of turbulence are the main agents causing surface covalent bond breaking leading to surface modification. Increase in substrate temperature from room temperature up to 100 ° C is also seen to increase the area of surface modification on treated PS samples. This is possibly due to the breakage of the van der Waals bonds on the PS surface causing the polymer chains to move more freely. The OES results show increases in spectral peaks of plasma species as the flow rate and applied power increases. We have shown that the applied power causes higher increases in the current and hence higher spectral peaks due to more rapid collisions of the plasma species contained within the plasma. XPS results of treated PS surface showed an increase of ~10 to 20 % in oxygen concentration and a reduction of ~10 to 20 % in carbon concentration for peaks corresponding to O 1s and C 1s. In addition, the development of nitrogen peaks with binding energy ~403 eV is obtained due to the presence of NH2 functional group in the allylamine monomer .The potential application of a non-thermal atmospheric pressure plasma source as a candidate for surface analysis in pharmaceutical applications has been demonstrated. This PADI technique is shown to be fast, simple and capable of high-throughput analysis. It does not require solvent or sample preparation prior to analysis and the results obtained show strong molecular peaks and low background signals.

Microplasma and microdischarge devices have been widely used in the applications intersecting various fields such as science and engineering. The literature survey conducted has increased our ability to understand, model and develop basic mechanisms and technologies that generate these microplasmas, as well as develop technologies for detection and analytical purposes. It has only been in the past few years that results of modeling and computational investigations of microdischarges have emerged in the literature and helped shed light on the basic understanding of microplasmas. There are still many theoretical elements to be incorporated into the design process, including the design of an equivalent circuit model, for simulation to be carried out using Pspice and other appropriate software. It is also important to mention that the results obtained are highly dependent on the specific nature of the parameters and settings used, hence the need for a detailed experimentation and analysis over a wide range. In general, the following insights were gained.

- Plasma process chemistry can be controlled effectively by the application of multiple diagnostic tools.
- The continued development of diagnostics applicable to a wider range of plasma species is critical to enhancing our understanding of plasma processing.
- A dielectric barrier discharge can be produced in a capillary of a few microns or nanometers by applying positive pulses from an ac generator. The spectroscopic behavior can be monitored, and the discharge can be modified by the presence of strong electric fields in the vicinity of the cathode and by relatively high gas flow through the capillary.
- Over the last decade, an undeniable trend towards miniaturization has developed plasma spectrochemistry and this trend is currently gaining momentum, as fuelled by research, development and characterization of small-scale plasmas and microplasmas. Numerous

reviews have been done covering the period up to the end of 2011 and publications covering analytical and other applications.

- The force driving plasma miniaturization is the potential for development of small, light-weight microfluidic diagnostic devices which consume less power and gas, and can be embedded within instruments for sensing and detection.

9.1 Future Direction

Focus can be made on the following in order to further develop this research.

1. The experiments conducted can be repeated in a more controlled manner using new chip designs as well as new system designs.

2. The microfluidic chips used so far have been used to separately ignite Helium (He) and Neon (N_e), but not a mixture of gases, or monomers. This can be done to expand our knowledge about the microdischarge behaviour within the microchannels.

3. The determination of plasma parameters such as electron density (N_e) and electron temperature T_e can be performed to better aid our understanding of the different discharge modes.

4. The light emissions from the microdischarges within the microchannel are limited by the dielectric layers. It will be interesting to develop some other ways of capturing light from the centre of the discharge and focusing it onto the entrance aperture of an optical fibre and then onto the input slit of a monochromator with changeable gratings inorder to obtain time averaged and line resolved emission measurements.

5. For fast imaging of the discharge gap, projection optics can be used to image the whole microchannel onto another detector which is sensitive to light in the appropriate wavelength range.

6. Future work will possibly investigate and compare spectral details from light intensities in diffuse and filamentary modes. Comparisons will be made with some time averaged emission spectra which have been reported previously [1, 2].

7. The model used in this experiment was considered for a parallel electrode configuration. A better model which includes the gas properties and the surface charges distribution on the dielectric surfaces, and also represents the conduction current in the microchannel by a voltage controlled current source has been proposed. The model has been enriched with the inclusion of observed conditions occurring during the discharges and this is currently being investigated.

References

1. Gottscho R. A. and Miller T. A. 1984 *Pure Appl. Chem.* **56** 189

2. Excitationcrosssections,availablefrom:http://jilawww.colorado.edu/www/research/coll-data.html